Cosmic-ray acceleration in supernova remnants

E. A. Helder

Cover: Wavy shock structure of the southeastern region of the RCW 86 supernova remnant. This observation is obtained with the FORS2 instrument, which is mounted on the Very Large Telescope in Chile.

Omslag: Golfachtige structuur van de buitenste rand van de zuidoostelijke regio van de supernovarest genaamd RCW 86. Deze waarneming is verkregen met het FORS2 instrument welke zich bevindt aan de 'Very Large Telescope' in Chili.

ISBN: 978-90-393-5394-3

Cosmic-ray acceleration in supernova remnants

Kosmische stralingsversnelling in supernovaresten
(met een samenvatting in het Nederlands)

Proefschrift

ter verkrijging van de graad van doctor aan de Universiteit Utrecht op gezag van de rector magnificus, prof.dr. J.C. Stoof, ingevolge het besluit van het college voor promoties in het openbaar te verdedigen op 28 september 2010 des middags te 4.15 uur

door

Eveline Alette Helder
geboren op 7 oktober 1982 te Venhuizen

Promotor:	Prof.dr. F. W. M. Verbunt
Co-promotor:	Dr. J. Vink

Dit proefschrift werd mede mogelijk gemaakt door financiële steun van NWO en LKBF.

Contents

1

Introduction

EVERY second, millions of millions of particles[1] from outer space hit the Earth's atmosphere. Many of them have energies far larger than can be achieved in any laboratory on Earth. Fortunately, most of the particles lose their energy already high up in the atmosphere, by causing cascades of less energetic particles. Ever since the discovery of these particles in 1912, scientists have wondered about their origin.

1.1 Cosmic-ray energy spectrum

The energy spectrum of these particles (so-called cosmic rays) in the Galaxy is well determined: it is described by a power-law with a fairly constant index over a large range in energy (Fig. 1.1). There is, however, a slight steepening at 3×10^{15} eV, which is generally referred to as 'the knee' in the cosmic-ray spectrum.

Cosmic rays with energies up to the knee and possibly up to 10^{18} eV (where the spectrum flattens, a feature referred to as 'the ankle') are thought to originate from the Galaxy. With these energies, the paths of the cosmic rays are randomized by the Galactic magnetic field. This causes the direction of arrival on Earth to be uncorrelated with the source of acceleration. The average lifetime of a cosmic-ray particle in the Galaxy is 15.6 ± 1.6 Myr (Yanasak et al. 2001). This puts constraints on the sources of cosmic rays: in order to maintain the cosmic-ray

[1] 1 particle per m^2-second (Figure 1.1) is 5×10^{14} particles per second on the Earth's atmosphere

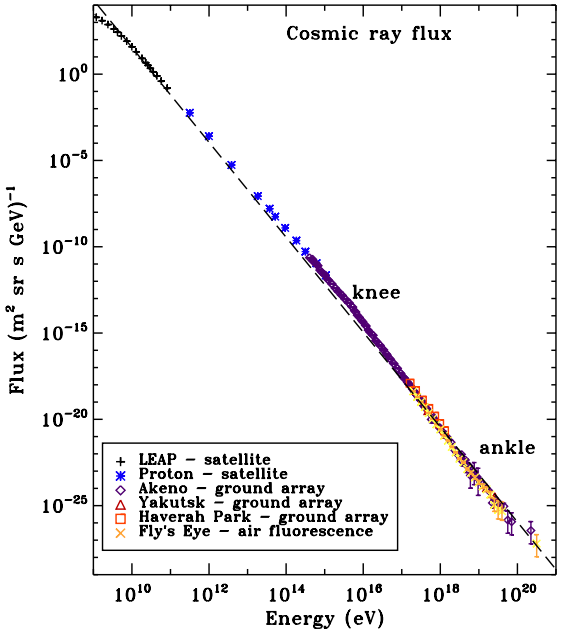

Figure 1.1: Cosmic-ray energy spectrum, as obtained by several experiments. Note the slight bends at 3×10^{15} and 10^{18} eV; also known as the 'knee' and the 'ankle' of the spectrum respectively (data compiled by J. Swordy, courtesy to Klara Schure).

energy density, the main cosmic-ray sources need to deliver about 10^{48} ergs/year. As supernovae are among the most energetic events in the Galaxy, this is one of the earliest and strongest arguments for supernovae (or their end-products) being the main sources of Galactic cosmic rays. To be the main sources of Galactic cosmic rays, supernovae need to transfer $\sim$10% of their initial kinetic energy into cosmic-ray energy (assuming an average of about 2-3 supernovae in the Galaxy per century, Tammann et al. 1994).

During a supernova explosion, kinetic energy is deposited into the outer layers of the star, creating fast shock fronts (with initial velocities of up to a few times 10^4 km s^{-1}), which sweep up the ambient medium.

A particle acceleration mechanism operating at shock fronts, is the so-called first-order-Fermi acceleration (also known as diffusive shock acceleration): charged particles scatter up and down the shock front on turbulent magnetic fields and each time they cross the shock front they effectively gain energy. This process

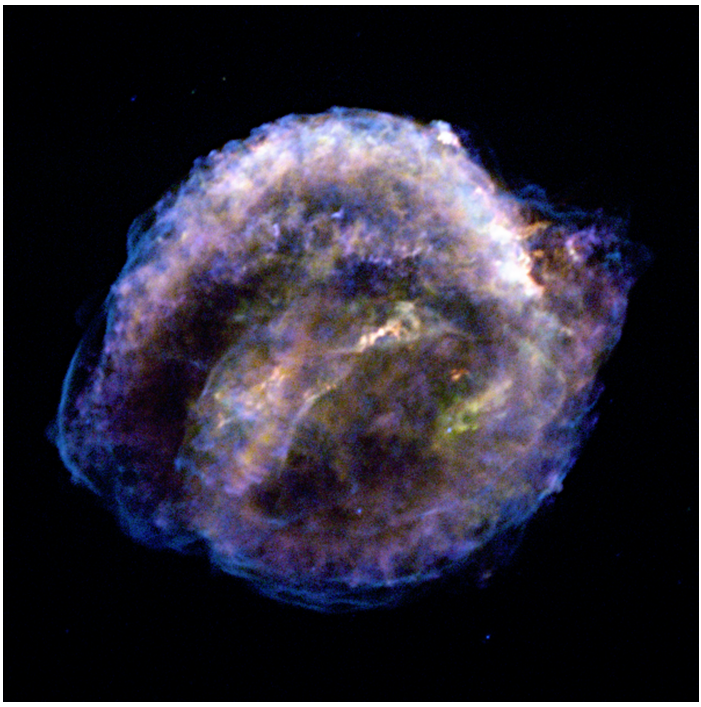

Figure 1.2: X-ray image taken by NASA's Chandra X-ray observatory of the remnant of the type Ia supernova witnessed by Johannes Kepler in 1604 C.E.. Red and yellow colors show the ejecta (0.3-0.72 and 0.72-1.7 keV respectively), shocked by the reverse shock. Blue shows synchrotron emission from relativistic electrons, accelerated at the forward shock. (Credits: NASA/CXC/NCSU/Reynolds et al. 2007).

stops when, at some point, the gyro radius[2] of the particle becomes too large for it to return to the shock, and the particles escape from the system. Alternatively, when the particle is scattered in the opposite direction and diffuses away from the shock.

Early evidence for accelerated particles in supernova remnants was found by the first generation of radio telescopes in the early fifties (Shklovskii 1953; Minkowski 1957). These telescopes detected emission from energetic electrons gyrating in the magnetic field of several remnants (synchrotron radiation). Electrons with even higher energies were found by the detection of X-ray synchrotron emission from the shocks of supernova remnants (Koyama et al. 1995, and Fig.

[2]radius ($r_{\rm g}$) of the curved path of a relativistic charged particle in a magnetic field. $r_{\rm g} = \frac{cE}{eB}$, where c is the speed of light, E the energy of a particle with charge e and B the magnetic field.

1.2). Recently, Cherenkov telescopes have detected TeV γ-ray photons from several supernova remnants, indicating the presence of particles with TeV energies (e.g., Aharonian et al. 2004). It remains unclear whether these photons are emitted by protons or electrons. The first explanation would imply the first direct evidence for accelerated protons by supernova remnants. This is an important issue, as 99% of the cosmic rays detected on Earth are protons (Meyer 1969). This issue might be resolved by data from the recently launched GeV γ-ray satellite Fermi, as these data will help distinguishing between both interpretations of the TeV γ-ray emission: the spectra for the different scenarios have substantial different shapes in the GeV energy range. Currently, the only supernova remnant detected in GeV and TeV γ-rays is Cassiopeia A. It appears that Cassiopeia A has converted $\sim 2\%$ of its explosion energy into cosmic-ray energy (Abdo et al. 2010), which is surprisingly little, as we expect a remnant to be the most efficient accelerator when the shock velocity is still high.

1.1.1 Research questions

Provided that supernova remnants are the main sources for Galactic cosmic rays, they convert 10% of their energy into cosmic rays. As this is a significant fraction, this must leave imprints on the dynamics of the remnant. We can use those imprints to investigate the physics of the acceleration process. This has the potential to identify supernova remnants as the main sources of cosmic-ray protons and therewith solving the question on the origin of Galactic cosmic rays. In this thesis, we try to answer the following questions, using both optical and X-ray observations:

- What imprints does cosmic-ray acceleration have on the dynamics of a shock?

- How can we use these imprints to understand the physics of the acceleration process?

1.1.2 Shock physics

Interstellar shocks are quite different from every-day shocks on Earth: the mean-free path of a particle in the Galaxy (density $\sim$ 1 particle cm^{-3}) is larger than the size of a typical young supernova remnant (few parsec). Therefore, it is quite surprising that shocks exist in the Galaxy as they require particles to communicate the existence of the shock. Apparently they do, because we observe the outer shocks of supernova remnants. The main characteristics of a shock are determined by its shock velocity, or, more precisely, by its Mach number; the shock velocity divided by the local sound speed. A fairly simple, but useful characterization of a shock is given by the laws of conservation of mass, momentum and energy. Taking

these conservation laws as starting point, and assuming that the thermal pressure of the ambient medium is negligible compared to the thermal pressure within the remnant, one can derive that the compression ratio of the shock (r) solely depends on the ratio of the specific heats of the plasma (γ, where γ is defined by $P \propto V^{-\gamma}$, in which P is the pressure and V the specific volume of an adiabatic gas):

$$r = \frac{\gamma + 1}{\gamma - 1}. \tag{1.1}$$

For example, for a non-relativistic plasma, $r = 4$ ($\gamma = 5/3$). Another useful observable is the temperature (T_i) behind the shock front for species with mass m_i:

$$kT_i = \frac{2(\gamma - 1)}{(\gamma + 1)^2} m_i v_{\rm s}^2. \tag{1.2}$$

This equation holds for shocks, behind which the different species are not in thermal equilibrium. For shocks with species in thermal equilibrium, the equation reads

$$kT = \frac{2(\gamma - 1)}{(\gamma + 1)^2} \mu m_p v_{\rm s}^2, \tag{1.3}$$

with μ the mean weight per particle (0.6 for fully ionized solar abundances). Note that, since these relations are based on the conservation of energy, these relations only hold for so-called non-radiative shocks: shocks for which the energy losses (e.g. in the form of radiation) are negligible.

1.1.3 Supernova remnant evolution

To understand the imprints of cosmic-ray acceleration on supernova remnants, we need to understand how a supernova remnant evolves. Supernovae come in two types: 1) a massive star ($M > 8M_\odot$) runs out of fuel and loses the battle against its own gravity. The core implodes, leaving behind a neutron star or a black hole. The envelope of the star will bounce off the hard core and expand into the ambient medium. 2) Mass transfer in a binary causes the mass of a Carbon-Oxygen white dwarf to exceed the Chandrasekhar limit ($1.4M_\odot$). This sets off an explosive thermonuclear burning of the white dwarf, where the burning products will expand into the ambient medium. Although the types of explosions are rather different, they show similar characteristics: in both cases, the explosion launches $\sim 10^{51}$ erg of kinetic energy into the ambient medium.

As the expanding ejecta sweep up ambient medium, they slow down. The boundary between the swept-up ambient medium and the still untouched ambient medium is called the forward shock. The slowing down of the expanding ejecta causes a second shock, moving inwards with respect to the forward shock: the reverse shock (Fig. 1.3, left). This reverse shock denotes the boundary between the shocked ejecta and the still freely expanding ejecta. The evolution of a supernova

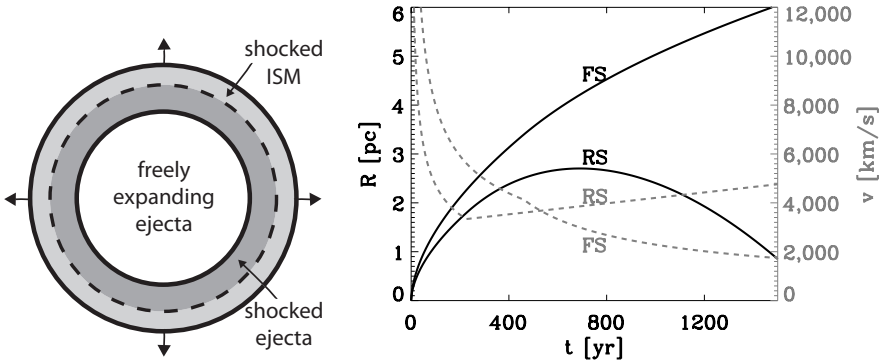

Figure 1.3: *Left* : Schematic representation of a supernova remnant. The outer circle indicates the forward shock. The dashed circle denotes the contact discontinity: the division between the shocked ambient medium on the outside and the shocked ejecta on the inside. The inner circle denotes the reverse shock. *Right*: Evolution of the forward (FS) and reverse shock (RS) radii (solid) and velocities (dotted) as function of time, for a typical Type Ia supernova remnant, assuming an explosion energy of 10^{51} erg, mass of the ejecta of $1.4 M_{\odot}$, and a density of the ambient medium of 1 particle per cm^{-3}. The reverse shock velocity is given in the frame of the freely expanding ejecta. The forward shock velocity is in our frame-of-reference.

remnant is generally characterized in three stages: 1) Right after the explosion, the dynamics are dominated by the ejecta pushing the shocked plasma outward. This is called the 'ejecta-dominated stage'. 2) After the reverse shock has shocked about half of the total ejecta mass, the main part of the kinetic energy contained in the ejecta is transferred to the expanding shell and the evolution is dominated by the energy originally released in the ejecta. This is the 'Sedov-Taylor stage' and typically starts after a few hundred years. 3) As the remnant grows older, the shock velocity decreases and hence the temperature behind the forward shock front will drop (equation 1.2). If the post-shock temperature drops below $\sim 5 \times 10^5$ degrees Kelvin (corresponding to a shock velocity of ~ 200 km s^{-1}), the radiation of H, He, C, N and O lines increases drastically (e.g. Schure et al. 2009) and the radiative losses become dynamically important (i.e. the remnant is no longer non-radiative). This causes the compression ratio of the shock to increase and the plasma will cool even faster, increasing the compression ratio even further. The thin, dense shell will eventually slow down until it dissolves into ambient medium (after 10^4-10^5 years).

The freely expanding ejecta within the reverse shock are not yet shocked and therefore do not emit in the X-ray energy bands. Note that at some point in the evo-

lution, the reverse shock will even come to a stand-still in our frame-of-reference and start moving inwards until it hits the center. At this point, all the ejecta of the progenitor has been shocked. The right panel in Fig. 1.3 shows the evolution of both radii and velocities of the forward and reverse shocks. Note that the velocity that describes the physical parameters behind (i.e. outside) the reverse shock is the one in the frame of the freely expanding ejecta ($v_{\rm s,\,ej}$), which is given by:

$$v_{\rm s,\,ej} = v_{\rm f,\,ej} - v_{\rm s,\,ob}. \tag{1.4}$$

Here, $v_{\rm s,\,ob}$ is the reverse shock velocity in our frame of reference and $v_{\rm f,\,ej}$ is the velocity of the freely expanding ejecta right before hitting the reverse shock. The latter is $r_{\rm RS}/t$, in which $r_{\rm RS}$ is the radius of the reverse shock and t is the age of the remnant. The plotted velocity in Fig. 1.3 is $v_{\rm s,\,ej}$.

1.1.4 Balmer-dominated shocks

As the plasma behind the shock front is hot (1.2 keV for a shock velocity of 1000 km s^{-1}, equation 1.2), most young remnants emit thermal X-ray emission. The continuum of this thermal X-ray emission is emitted by electrons as their paths get deflected by the ionized ions in the plasma. The shape of the continuum is hence characterized by the temperature of the electrons in the plasma. This process is called bremsstrahlung (also known as free-free emission).

Equation 1.2 and 1.3 show that the species right behind a shock front are not necessarily in thermal equilibrium. If the electron and proton temperature ($T_{\rm e}$ and $T_{\rm p}$) in a plasma are fully out of equilibrium, $T_{\rm p}/T_{\rm e} = m_{\rm p}/m_{\rm e}$ (equation 1.2). When the only equilibration of the temperatures occurs through Coulomb collisions, it takes $> 3 \times 10^5$ years to equilibrate $T_{\rm e}$ and $T_{\rm p}$ (e.g., Vink 2008a, for $n_{\rm e} = 1$ and $v_{\rm s}$=4000 km s^{-1}). However, recent empirical studies show that the protons and electrons in a plasma behind shock with $v_{\rm s} < 400$ km s^{-1} are in full thermal equilibrium, whereas, behind faster shocks, the electron temperature can be as low as 3% of the proton temperature (Ghavamian et al. 2007b; van Adelsberg et al. 2008). This has been determined using Balmer-dominated shocks. Balmer-dominated shocks are non-radiative shocks of which the hydrogen line emission consists of two superimposed Gaussian lines. The narrow line is emitted by hydrogen atoms right after entering the shock front; its line-width reflects the hydrogen temperature of the ambient medium (process 1 in Fig. 1.4). The broad line is emitted by hot protons after undergoing charge exchange with the incoming neutral hydrogen and its width reflects the proton temperature behind the shock front (process 2 in Fig. 1.4). As the temperature behind the shock front is of the order of 10^6 Kelvin, neutral hydrogen will be ionized within one month after entering the shock front. This leads to very thin filaments of hydrogen line (broad and narrow) emission, marking the location of the forward shock.

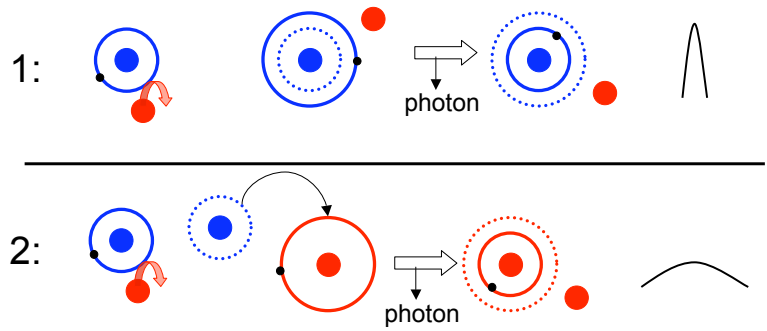

Figure 1.4: Schematic representation of the processes forming the hydrogen lines of a Balmer dominated shock. The blue (red) circles indicate cold (hot) protons. The small black circles indicate electrons. Process 1 shows the excitation of neutral cold hydrogen and producing a narrow line. Process 2 shows a hot proton, taking over an electron from a neutral hydrogen atom, and producing a broad emission line after excitation. (Note that the excitation of the atom can be done by electrons as well.)

1.2 Imprints of cosmic-ray acceleration on a supernova remnant

1.2.1 Structure of a cosmic-ray modified shock

As mentioned before, charged particles (cosmic rays) scatter on turbulent magnetic field back and forth over the shock front. This creates a so-called cosmic-ray precursor in front of the shock (Fig. 1.5). This in itself gives the shock already a modified structure with respect to a classical textbook shock, where the shock is solely a discontinuity. The precursor pushes the ambient medium outward (Lee et al. 2007). Additionally, the ambient medium gets pre-heated. This causes difference in shock velocity over the main shock to decrease, which leads to a temperature behind the main shock, lower than one would expect from equation 1.2 or 1.3.

In contrast, the *total* compression ratio of a cosmic-ray modified shock increases, as the equation-of-state of the shock becomes relativistic (γ lowers). Additionally, as the shock loses energy in the form of escaping cosmic rays, the compression ratio increases further (Decourchelle et al. 2000).

1.2.2 Increased compression ratio

This increased compression ratio is indicated in X-ray emission by a smaller width of the layer of the shocked ambient medium (Fig. 1.3) than one would expect from models without cosmic-ray acceleration. This has been first detected in the Tycho supernova remnant (Warren et al. 2005). A similar study for the SN 1006 remnant showed that the total compression ratio is higher in the regions coinciding with signs of cosmic-ray acceleration (Cassam-Chenaï et al. 2008).

1.2.3 Cosmic-ray spectrum

An increased compression ratio has its influence on the spectrum of the cosmic rays at the shock front. The power-law index of the cosmic-ray spectrum at the shock front is a function of the compression ratio that the particles experience as they scatter back and forth over the shock front. The higher the compression ratio, the higher the difference in shock velocity the particle feels and the higher the gain in energy in each iteration:

$$N(p) = p^{-3r/(r-1)+2} = p^{\Gamma}. \tag{1.5}$$

Where $N(p)$ is the number of particles with momentum p and Γ the power-law index. Hence, the cosmic-ray spectrum in a non-modified shock (inefficient acceleration) has $\Gamma = -2$, which will increase to a value of -1 for an infinite compression ratio. This provides a way for tracing a cosmic-ray modified shock from the synchrotron emission, as follows. The electrons with higher energies have larger gyro radii and will scatter through a larger range in radius over the shock front. As Fig. 1.5 shows, those particles will experience up to the full compression ratio of the shock, whereas the less energetic electrons will be confined to the main shock and will only experience the compression of the main shock. This implies that the spectrum will get harder for higher energies. Comparing the power-law index of the radio emission with the power-law index from X-ray synchrotron emission from the same shock will shock whether the shock is modified by cosmic rays. Such an effect has been found for both the RCW 86 and the SN1006 supernova remnants (Vink et al. 2006; Allen et al. 2008).

The shape of the cosmic-ray spectrum determines the importance of the energy losses for the dynamics for the system. A very hard spectrum ($N(p) \propto p^{-1}$) will have most of its energy contained at $p_{\rm max}$, making the shock a very productive accelerator and energy losses dynamically very important. The ratio of the energy flux, escaping the system at $p_{\rm max}$ ($F_{\rm CR}$) and the total cosmic-ray pressure within the system ($P_{\rm CR}$) is as follows:

$$\frac{F_{\rm CR}}{P_{\rm CR}} = (2-\Gamma)(1-\frac{1}{r})v_{\rm s}, \tag{1.6}$$

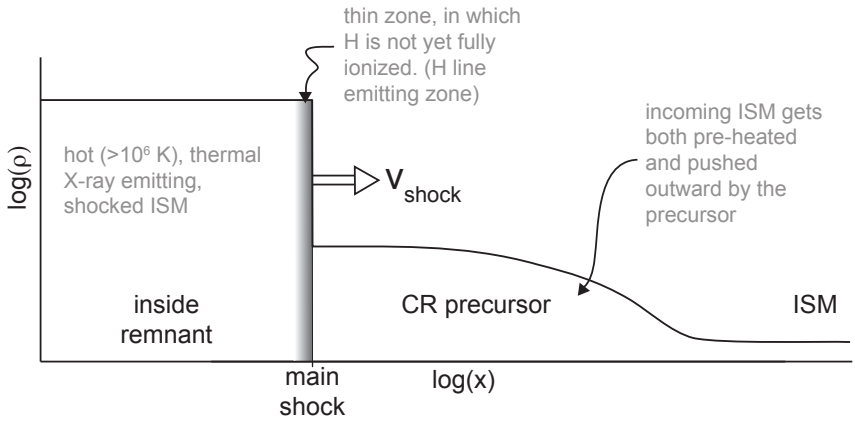

Figure 1.5: Schematic representation of a Balmer-dominated, cosmic-ray modified shock. On the x-axis is the radial coordinate increasing outwards and the y-axis denotes the density. Right from the main shock is the cosmic-ray precursor. (Based on models of Caprioli et al. 2009).

(Malkov & Drury 2001; Drury et al. 2009). For $\Gamma = 2$, the integral over the cosmic ray pressure diverges, and $(\Gamma - 2)$ is replaced with $1/\ln(cp_{\max})$. Note that this equation uses the total compression ratio and therefore assumes a constant Γ over the whole energy range of the spectrum.

1.2.4 Magnetic field amplification

The accelerated particles in front of the shock will contribute to the local pressure and hence form a so-called cosmic-ray precursor (Fig. 1.5). In addition, these particles locally create turbulent magnetic fields, amplifying the existing magnetic field well beyond the value of the ambient magnetic field. The compression of the shock itself increases the magnetic field even more (Bell & Lucek 2001; Bell 2004). These post-shock magnetic fields strengths can be measured from X-ray observations, as the highest energy electrons emit X-ray synchrotron emission. As the electrons diffuse away from the shock, they lose their energy fast (in a few years) due to this emission. At some point their energy is too low to emit synchrotron emission in X-rays (see Fig. 1.2). Hence, the width of the X-ray synchrotron rim provides a measure of how fast the electrons have lost their energy, indicating the post-shock magnetic field strength (Vink & Laming 2003). Increased magnetic field strengths have been found for many young supernova remnants (Bamba et al. 2005) and the magnetic field pressure appears to be typically around 3.5% of the ram pressure of the shock front, $\rho v_{\rm s}^2$ (Völk et al. 2005).

1.2.5 Temperature behind the shock front

For an efficiently accelerating shock, the post-shock temperature is lower than expected from equation 1.2. Hence, once we know the shock velocity and the post-shock temperature, we can characterize the cosmic-ray acceleration efficiency (Decourchelle et al. 2000; Drury et al. 2009). This has been found in the remnant 1E 0102 (Hughes et al. 2000b). Alternatively, shocks in the old ($\sim 10,000$ year) Cygnus Loop remnant does not show a discrepancy from equation 1.2 (Salvesen et al. 2009). Both studies use the post-shock electron temperature to characterize the temperature modification of the shock, assuming a certain measure for the electron-proton temperature equilibration. However, as indicated in chapter 3, this effect would ideally be measured by the post-shock proton temperature, as this temperature is closest to the mean plasma temperature.

1.3 Outline of this thesis

In this thesis, we studied several young supernova remnants, using X-ray and optical observations, in order to characterize the imprints of cosmic-ray acceleration on these remnants.

In *chapter 2*, we study the non-thermal X-ray emission of the Cassiopeia A supernova remnant, using a long (1Ms) Chandra observation. In particular, we focus on the filamentary structure at the inside of the remnant. We use a deprojection algorithm to show that this emission can not solely result from the blast wave, projected onto the inside. We identify that the emission originates from the reverse shock and is emitted by highly energetic electrons (i.e. synchrotron emission). This shows that particle acceleration can also occur at the reverse shock for some remnants.

Chapter 3 describes our study on the cosmic-ray acceleration efficiency of the RCW 86 supernova remnant. This northeast rim of this remnant shows indications for efficient cosmic-ray acceleration, as it emits X-ray synchrotron emission and is detected by the TeV γ-ray telescope H.E.S.S.. We use Chandra observations of two epochs to determine the proper motion of the northeastern rim of the remnant. The proper motion of the rim indicates a shock velocity of 6000 ± 2800 km s^{-1}. This velocity is inconsistent with the post-shock proton temperature, which we determined from the broad line of the Hα emission, as observed with the Very Large Telescope (VLT). We attribute this difference to the presence of a cosmic-ray pressure behind the shock front of over 50% of the total post-shock pressure.

Chapter 4 presents a detailed study on the X-ray emission of the young type Ia remnant in the Large Magellanic Cloud (LMC), SNR 0519-69.0. We used both high resolution spectra and images obtained with the RGS instrument onboard XMM-Newton and CCD instruments onboard Chandra respectively. We found a clear indication for stratification of the burning products in the ejecta. Additionally,

we used the Doppler-broadened spectral-line widths, combined with both analytical and hydrodynamical models, to determine a shock velocity of the remnant of 2700 ± 500 km s^{-1}.

In *chapter 5*, we use a similar method to determine the shock velocity of the youngest type Ia supernova remnant of the LMC, SNR 0509-67.5. We combine this with optical spectra from the VLT, from which we use the broad component of the Hα-line to determine the post-shock proton temperature in two locations in the remnant: the southwest and northeast rim. For the southwestern rim, we can only explain our measurements if we allow for $>$20% contribution of cosmic-ray pressure behind the shock front. For the northeast rim, we have two possibilities: either the electrons and protons behind the shock front are in thermal equilibrium, or, if we assume that the electron temperature is less than 10% of the proton temperature, the cosmic-ray pressure behind the shock front is $> 7\%$. This chapter shows that the effect found in *Chapter 4* is not an unique result, and shows that supernova remnants are very promising sources for Galactic cosmic rays.

Chapter 6 describes our study on the temperature equilibration behind several shocks of the RCW 86 supernova remnant. We us optical spectra obtained with the VLT to determine the post-shock proton temperature and we determine the electron temperature from X-ray spectra, obtained with XMM-Newton. Earlier studies reported that the electron to proton temperature ratio depends on the shock velocity in an elegant way: ($T_{\rm e}/T_{\rm p} \propto 1/v^2$). Our study shows that this relation is not this well-determined for the RCW 86 supernova remnant.

2

Characterizing the non-thermal emission of Cassiopeia A

E.A. Helder and J. Vink
Astrophysical Journal, 2008, 686, 1094

We report on our analysis of the 1 Ms Chandra observation of the supernova remnant Cas A in order to localize, characterize and quantify its non-thermal X-ray emission. More specifically, we investigated whether the X-ray synchrotron emission from the inside of the remnant is from the outward shock, but projected toward the inner ring, or from the inner shell. We tackle this problem by employing a Lucy-Richardson deconvolution technique and measuring spectral indices in the 4.2-6 keV band.

We show that most of the continuum emission is coming from an inner ring that coincides with the location of the reverse shock. This inner ring includes filaments, whose X-ray emission has been found to be dominated by X-ray synchrotron emission. The X-ray emission from these filaments, both at the forward shock and from the inner ring, have relatively hard spectra with spectral index > -3.1. The regions emitting hard X-ray continuum contribute about 54% of the total X-ray emission in the 4.2-6 keV. This is lower than suggested by extrapolating the hard X-ray spectrum as measured by BeppoSAX-PDS and INTEGRAL. This can be reconciled by assuming a gradual steepening of the spectrum toward higher energies. We argue that the X-ray synchrotron emission is mainly coming

from the Western part of the reverse shock. The reverse shock in the West is almost at rest in our observation frame, corresponding to a relatively high reverse shock velocity of ~ 6000 km s^{-1} in the frame of the freely expanding ejecta.

2.1 Introduction

Supernova remnants (SNRs) are the main candidates for producing Galactic cosmic rays, with energies at least up to the so-called knee of the cosmic ray spectrum at $\sim 3 \times 10^{15}$ eV. The first direct evidence for this is the detection of X-ray synchrotron emission caused by $\sim 10^{14}$ eV electrons (first established for SN1006, Koyama et al. 1995). Since the energy of electrons suffers from radiation losses, this might indicate even higher energies for ions. Moreover, hard X-ray tails up to 80 keV have been discovered for several Galactic SNRs (Allen 1999). This has been contributed to either non-thermal bremsstrahlung (Laming 2001) or to synchrotron radiation (Allen et al. 1997). In recent years, additional direct evidence for efficient cosmic ray acceleration has come from detection of TeV γ-rays for several SNRs by the High Energy Gamma-Ray Astronomy (HEGRA) experiment, the High Energy Spectroscopic System (H.E.S.S, e.g. Aharonian et al. 2004) and MAGIC (Albert et al. 2007). The γ-ray emission is either caused by inverse Compton scattering by the same electrons that cause X-ray synchrotron emission, or by pion production caused by collisions of accelerated ions with the background plasma.

Cassiopeia A (Cas A) is one of the supernova remnants with a hard X-ray tail (The et al. 1996) and has recently also been detected in γ-rays (Aharonian et al. 2001; Albert et al. 2007). This remnant was until recently[1] the youngest known supernova remnant in the Galaxy; its supernova was probably around 1671 (Thorstensen et al. 2001). In 2001 Chandra detected thin, X-ray synchrotron emitting, filaments at the forward shock of the remnant (Fig. 2.1, see also Gotthelf et al. 2001). This implies the presence of electrons with energies of $\sim 10^{13}$ eV for the magnetic fields in Cas A, estimated to be 0.1 mG to 0.6 mG (Vink & Laming 2003; Berezhko & Völk 2004). These synchrotron rims can be understood in the context of diffusive shock acceleration and synchrotron cooling downstream of the shock.

In addition, the Chandra image shows thin filaments at the inside of the remnant. Some of these inner filaments show a featureless spectrum (Fig. 2.2). Hughes et al. (2000a) identified one of the inner filaments at the West side of the remnant ('region D') as being the projected forward shock, based on its featureless spectrum. DeLaney et al. (2004) found that the kinematics of the inner filaments, which they interpreted as projected forward shock filaments, are different from the forward shock; they have a lower velocity.

[1] Recent expansion measurements of G1.9+0.3 show an age for this remnant of around 100 years

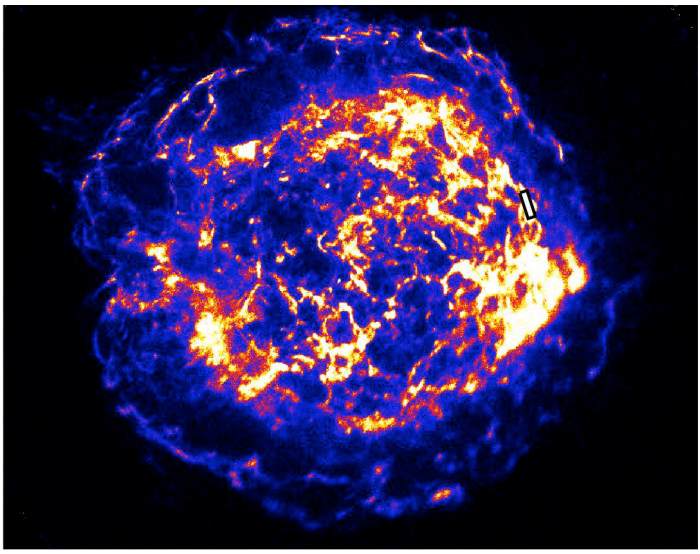

Figure 2.1: Million second 4-6 keV continuum image of Cas A, obtained with Chandra. The rectangle indicates region 'D' in Hughes et al. (2000a).

Diffusive shock acceleration is a process which accelerates cosmic rays at a shock front (for a review, see Malkov & Drury 2001). This mechanism accelerates charged particles of sufficient energy, which scatter on turbulent magnetic fields/plasma waves on both sides of the shock front. Each time the shock front is crossed, the particle gains energy, due to the difference in plasma velocity between both sides of the shock front. The higher the difference in the velocities is, the more energy is gained in one cycle and the higher the magnetic field and magnetic field turbulence, the more often particles cross the shock front. Since at the location where efficient particle acceleration takes place recently accelerated electrons are present, these locations show X-ray synchrotron radiation. However, further downstream from the shock front, synchrotron losses result in lower maximum energies of the synchrotron radiation.

The synchrotron spectrum can be approximated over a large range in frequencies with a power-law in flux density: $F_\nu \propto \nu^{-\alpha}$ with an index (α) related to the power-law index of the electron distribution (p) as: $\alpha = (p-1)/2$. In what follows, we use index Γ, which refers to the number density index $\Gamma = -(\alpha+1)$ and $n(E) \propto E^\Gamma$. Near the maximum electron energies, the electron spectrum has an exponential cut-off, but the resulting synchrotron spectrum cuts off less abruptly, roughly as $\exp(-\sqrt{\nu/\nu_{max}})$ (Zirakashvili & Aharonian 2007). In contrast, the

(Green et al. 2008; Reynolds et al. 2008).

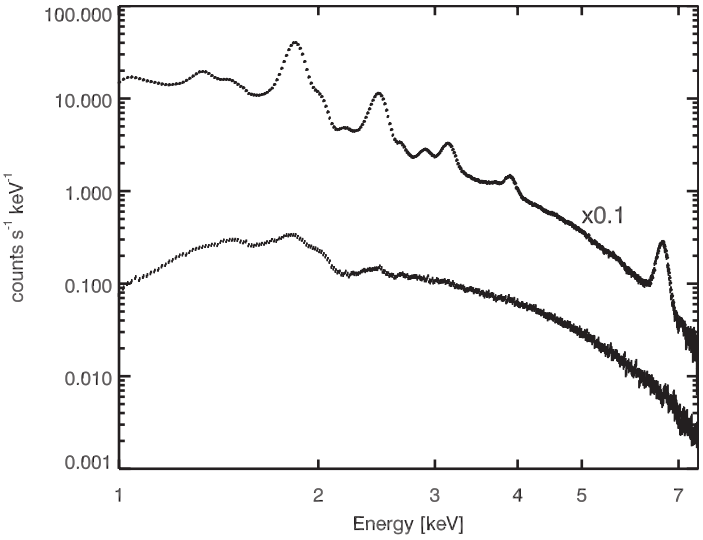

Figure 2.2: The spectrum of Cas A as observed by Chandra. Below is the spectrum of the featureless filament ('D') described by Hughes et al. (2000a) extracted from the megasecond observation, above is a spectrum of the whole remnant of one single observation (ObsID 4638), multiplied by 0.1.

other important continuum emission process, thermal bremsstrahlung, has an exponential cut-off ($\propto \exp(-h\nu/kT)$). In Cas A, the plasma temperature ranges between 0.6 and 3.6 keV (Yang et al. 2008). One should take into account that these temperatures originate from a thermal model. If a partly non-thermal spectrum is fitted with a thermal model, the fitted temperature tends to increase with respect to the real temperature of the plasma. For a thermal bremsstrahlung spectrum with a temperature of 3.5 keV, the power-law index between 4.2 and 6.0 keV is -2.8. For a synchrotron spectrum at the forward shock of Cas A, we typically measure a power-law index of -2.1. We therefore expect the bremssstrahlung continuum to be steeper than the synchrotron continuum in the 4 to 6 keV continuum band.

In this paper we investigate the shape of the continuum spectrum and its spatial distribution in order to address several questions pertaining to the shock acceleration in Cas A: What is the location of the X-ray synchrotron filaments? What fraction of the overall X-ray continuum is thermal and what fraction is non-thermal? And what are the implications for the hard X-ray emission, above 10 keV. We do this by analyzing the Chandra megasecond observation of Cas A.

2.2 The used data

Chandra observed Cas A for one million second in 2004 from Februari to May (Hwang et al. 2004) with the ACIS S3. For extracting the images, we use the CIAO package, version 3.4. To align the separate pointings, the central compact object is taken as a reference point. We mostly concentrate on the 4.2 to 6 keV energy band, but in addition, we also extracted an image in the line of Si XIII Heα from 1.80 to 1.90 keV. We corrected this for continuum emission by subtracting the average of two images next to the Si line: in the 1.63 - 1.64 and 2.13 - 2.14 keV bands.

We compared the results of our analysis of the Chandra data with a VLA radio map, made in the 6 cm band in 2000-2001. This map was kindly provided to us by Tracey DeLaney (Delaney et al. 2005). The VLA image has a resolution of $0.38'' \times 0.33''$, which is comparable to the Chandra telescope resolution of $0.42''$. However, the Chandra pixels size of $0.49''$ slightly undersamples the Chandra resolution.

In section 2.4, we make use of BeppoSAX observations made in June 2001, with an exposure time of 501 ks. The hard X-ray spectrum obtained with the PDS instrument is described in Vink et al. (2001). The data obtained with the MECS instruments were never published before, but the details of the analysis are similar to the analysis described in Vink et al. (1999) for a shorter exposure.

Finally, the INTEGRAL-ISGRI spectrum used in section 2.4 is described in Renaud et al. (2006).

2.3 Separating the forward and reverse shock

The surface brightness ($\Sigma(r)$) of an optically thin object consists of the emissivity function of this object ($\epsilon(r)$), integrated along the line-of-sight. For a spherically symmetric object, this integral is as follows:

$$\Sigma(r) = 2 \int_r^R \epsilon(r') \frac{r'}{\sqrt{r'^2 - r^2}} dr' \tag{2.1}$$

In which R denotes the outer radius of this object. We do the deconvolution in cylindrical coordinates, with θ perpendicular to r, and $\theta = 0$ is defined in the West, increasing counterclockwise. The number of counts in a sector at inner radius r, angular width $d\theta$ (in radians) and thickness dr is:

$$C_r = \Sigma(r) d\theta \left(r dr + \frac{(dr)^2}{2} \right) \tag{2.2}$$

By dividing Cas A in 18 sectors of 20° each, we first make surface brightness profiles of the X-ray continuum between 4.2 and 6 keV. For the surface

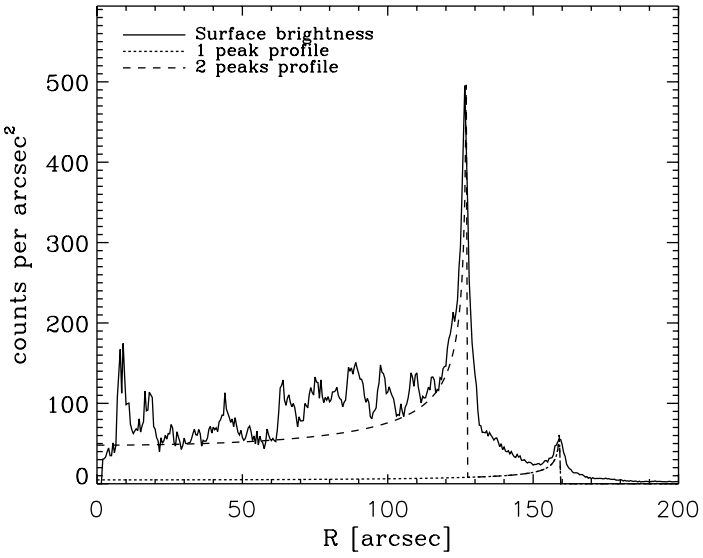

Figure 2.3: Radial surface brightness profile (black solid line) in the 4.2 to 6.0 keV energy band at an angle of 10° to 30° (including the featureless filament found by Hughes et al. (2000a)). The smoot=h, dotted solid line indicates what the profile will look like if the surface brightness is produced by an emissivity function with only a peak at the outer shock. For the dashed line, we use an emissivity function with two peaks. Note that this is not a fit, just an illustrative example.

brightness profiles, we adopt the center of expansion (Thorstensen et al. 2001): $\alpha = 23^{\rm h}23^{\rm m}27^{\rm s}.77$ and $\delta = 58^\circ48'49.4''$ (Equinox J2000) and take step-sizes of 0.5". Furthermore, we assume spherical symmetry for each sector individually. For an example of a surface brightness profile, see the radial surface brightness profile between an angle of 10° to 30° in Fig. 2.3. In this figure, we can clearly see the outer shock coming up at 160", as already found by Gotthelf et al. (2001). Using equations 2.1 and 2.2, we now make an emission profile in such a way that it fits the surface brightness of the outer shock (smooth solid line). As the line indicates, this thin, outer shell, can not account for all the surface brightness in the center of the remnant (the line which fits the outer peak is for a small R at least 15 times lower than the surface brightness profile). We also see a peak in the surface brightness at 126". We can identify this surface brightness peak with the featureless filament described by Hughes et al. (2000a). If we now include a second emission peak at 126"(dashed line), we see that a large part of the surface brightness in the center is covered.

To go from surface brightness to emissivity we use a general de-convolution

method described by Lucy (1974) and previously used on SN1006 by Willingale et al. (1996). To test this algorithm, we simulated emission functions, convolved them into a surface brightness profile and add Poisonian noise using the IDL routine 'poidev' from the NASA IDL Astronomy User's Library (Landsman 1993), we made them in such a way that the peak of the number of counts in one bin of $20^\circ \times 0.5''$ is 11000, which corresponds to the peak of Fig. 2.3 in terms of counts per $0.5'' \times 20^\circ$ bin. After constructing this surface brightness profile we used the Lucy algorithm to recover the emissivity function. We stopped the de-convolution after 30 iterations. The resulting emissivity function is similar to the original one, within 10% for $R > 40$"and even within 5% for $R > 75$".

2.3.1 Results of the deconvolution

The results of the de-convolution of the Chandra data of Cas A are given in Fig. 2.4. We see the forward shock coming up in the X-ray continuum at 160"and with a width of 10". What we also see, is another ring inside the forward shock with a radius of 115"with a width of 30", shifted to the right by 15". The forward shock and this inner ring are two almost complete circles, except for the NE region, where the jet is present. If we do the same for the radio and Si images of Cas A, we see a ring at the same location as the inner ring of the X-ray continuum. These inner rings in radio and Si have in previous researches been identified as the reverse shock (Gotthelf et al. 2001).
We note that the results of the deconvolution are far from perfect; the χ^2_{red} of the individual fits range from 20 to 253 for 4.2 to 6.0 keV and from 18 up to 1150 for the Si band. This is to be expected, since the filamentary structure is clearly inconsistent with the assumed spherical symmetry. Moreover, the X-ray Doppler maps of Cas A (Willingale et al. 2002) also show deviations from spherical symmetry. However, the fact that we can trace the inner and outer shells consistently from 18 independent deprojected sectors, argues for the veracity of the two rings.

In order to estimate the total contribution of each shell to the total emissivity of Cas A in each band, we multiply the deprojected shells with the volume of the shells ($4\pi R^2 \Delta R$), taking into account the relative contributions of each sector. For the continuum band in the East to South ($\theta \in [180^\circ, 260^\circ]$), for which the overall X-ray radiation is dominated by silicon line emission, 16 % comes from the outer ring and 84 % comes from the inner ring. For the Western part of the remnant ($\theta \in [-100^\circ, 20^\circ]$), in which most of the filaments dominated by continuum are situated, we find that 18 % of the continuum emission is due to the outer ring and 82% due to the inner ring.

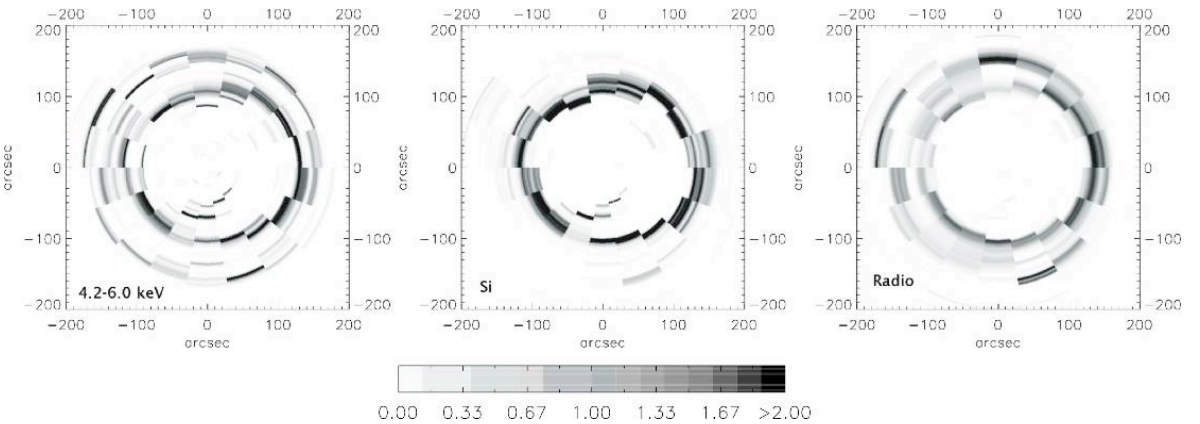

Figure 2.4: In the left figure we see the de-convolution of the 4.2 to 6.0 keV continuum radiation. For all the figures, the deconvolution is done in sectors, within each sector, spherical symmetry is assumed. The scale is in % per bin. Each sector is scaled in such a way that the total adds up to 100%. The middle figure shows the de-convoluted Si image and the right figure the deconvolution of the radio emission. The emissivity is multiplied with the volume of the shell to get the total emission over the whole sphere for each dr.

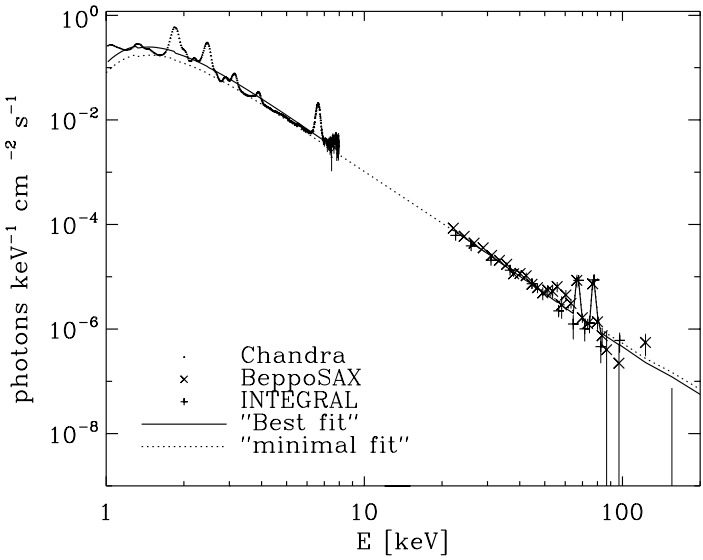

Figure 2.5: Unfolded broadband X-ray spectrum of Cas A. The solid line represents the best fit for the combined BeppoSAX/PDS and INTEGRAL/ISGRI data. Extrapolation of this line back to the Chandra regime fits the continuum surprisingly well. The dotted line indicates the minimal number of counts in the 4.2 to 6.0 keV band, allowed within the errors of the extrapolation of the hard X-ray fit. The Chandra broadband spectrum of Cas A was made from one of the observations (ObsID 4638) of the megasecond observation (Hwang et al. 2004).

2.4 Thermal Bremsstrahlung versus Synchrotron radiation

The hard X-ray emission from Cas A is clearly non-thermal in nature (The et al. 1996; Allen et al. 1997; Favata et al. 1997). In order to see how this relates to the Chandra spectrum of Cas A, we show in Fig. 2.5 both the broadband (1-8 keV) Chandra spectrum and the hard X-ray spectrum (above 20 keV) as obtained with BeppoSAX/PDS (Vink et al. 2001) and INTEGRAL/ISGRI (Renaud et al. 2006). The model shown is fitted to the hard X-ray data only and is similar to the one used by Renaud et al., which includes the contributions of ^{44}Ti decay at 67.8 and 78.4 keV. We included absorption with $N_{\rm H} = 1.3 \times 10^{22} {\rm cm}^{-2}$. Of interest here are the best fit parameters of the non-thermal component, fitted with a power-law. Our best fit parameters are $\Gamma = -3.4 \pm 0.2$ and the normalisation is 3.22 $\pm$1.9 counts keV^{-1} cm^{-2} s^{-1} at 1 keV. We checked these results with previous results on the hard X-ray tail of the spectrum of Cas A. Rothschild & Lingenfelter (2003)

observed Cas A for 226 ks with RXTE and fitted a power-law to the HEXTE data from 20 to 200 keV. They find a power-law index of -3.125 $\pm$ 0.050 with a normalization of 2.0 ± 0.6 counts $\mathrm{cm}^{-2}\mathrm{s}^{-1}$ at 1 keV.

We see that the BeppoSAX power-law, extrapolated back to Chandra energies, fits the continuum between 2.0 - 7.0 keV well. Within a confidence level of 90%, the extrapolated powerlaw contains a minimum of 93% of the counts in the Chandra continuum bands. The results of Rothschild & Lingenfelter (2003) amounts to a continuum flux from 4 to 6 keV which is 28% of the continuum flux measured by Chandra. Note that if we trust the power-law continuum model, there is little room for an additional thermal component. This is surprising, since we know that the continuum in the 1-10 keV range is at least partially due to thermal bremsstrahlung, which must accompany the copious X-ray line emission. In fact, fitting the spectrum in the 0.5-10 keV band can be done with a pure thermal model (Vink et al. 1996; Willingale et al. 2002).

To pinpoint the different mechanisms which contribute to the continuum in the Chandra band, we fit a power-law to regions of $4.9'' \times 4.9''$ (10×10 pixels) for the band between 4.2 and 6.0 keV. We use the eventfiles of the megasecond observation, which we merge, using the central compact object as a reference point. We use one ARF[2] file, made for the spectrum of Fig. 2.5. We estimated the background contribution, using an annulus around Cas A, with $R_{min} = 205.8''$ and $R_{max} = 235.2''$ and a center as defined in section 2.3. We neglected the effects of differential absorption over this small band; in the most extreme cases, the absorption varies from 1×10^{22} to $1.7 \times 10^{22}\mathrm{cm}^{-2}$ which has an effect of at maximum 0.09 in the power-law index. Fitting the continuum of the total remnant between 4.2 to 6.0 keV, using $\mathrm{N_H} = 1.3 \times 10^{22}\mathrm{cm}^{-2}$, we found that the average index is -3.14.

Fig. 2.6 shows that the power-law index varies considerably inside Cas A. We see that some of the regions with hard spectra overlap with known regions of non-thermal X-ray emission. For example the forward shock region appears to have a harder power-law. And also the non-thermal filaments in the West show up in the spectral index map. However, there are also is also hard continuum emission in regions where there is also line emission. This is illustrated by Figures 2.6 and 2.7.

The spectral map of Fig 2.6 implies that if we observe Cas A at higher energies, the Western part of the remnant will become more prominent. We validated this by comparing an extrapolation of our best fit power-law spectra with the 501 ks BeppoSAX/MECS observation in the 9-11 keV band.[3] We deconvolved the BeppoSAX image using the Lucy deconvolution method, following the procedure described in Vink et al. (1999). The results are shown in Fig 2.8. for comparison, we also show the 4 to 6 keV BeppoSAX image next to the Chandra image

[2] Ancillary Response File, which contains a description of the effective area of the instrument.

[3] There is also an observation made by XMM-Newton of Cas A up to 15 keV (Bleeker et al. 2001), because of errors in the exposure map of this observation, we choose to use the BeppoSAX data.

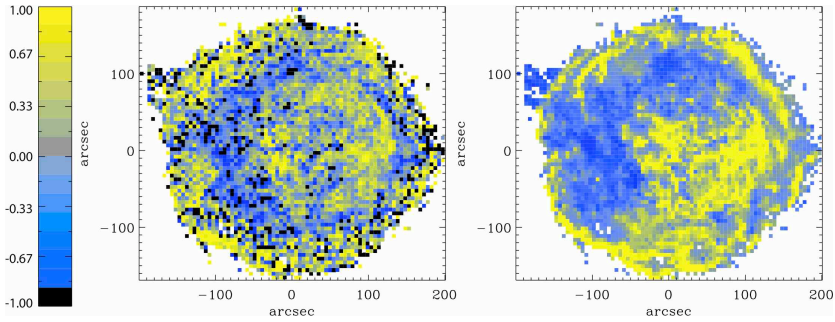

Figure 2.6: In the left Figure, we see the fitted power-law indices (Γ) + 3.1, to show the difference between the individual fits and the overall spectrum. Dark indicates a steeper spectrum. In the right Figure, we see a map of an image in the 4.2-6.0 keV continuum bands divided by a broadband image. The lighter color means relatively more continuum and thus a harder spectrum. Note the similarities between the images: as already noted by DeLaney et al. (2004), the continuum dominated areas tend to have a harder spectrum. Even so, not all hard spectra have a lack of line emission.

smoothed to roughly the same resolution (the extrapolation without smoothing is shown in Fig 2.9). Qualitatively the 9-11 keV image of BeppoSAX agrees with the extrapolated Chandra image: the South-Eastern part of the remnant is relatively less bright, whereas the Western part and the Southern part of the center are becoming more prominent.

Since for a bremsstrahlung continuum, we expect an exponential cut-off and thus a soft spectrum and for synchrotron radiation, we expect a hard spectrum, we tentatively identify the hard spectra with synchrotron emission. Although there is a likely overlap in spectral index between thermal and non-thermal emission we can nevertheless estimate the total contribution of non-thermal emission by noting that in Fig. 2.6 left, those regions that have abundant line emission (the Eastern part of the shell), have power-law spectra steeper than -3.1. The total flux associated with those power-law indices amounts to 46 % of the total flux in the 4.2 to 6 keV band (Fig. 2.10) , suggesting that the other 54% of the flux, is due to non-thermal radiation. This corresponds roughly to a total non-thermal flux above 4 keV of 2.7×10^{-10}erg s^{-1} cm^{-2}. If we take a power-law index of -2.8 as an upper limit, this corresponds to a thermal bremsstrahlung model with kT = 3.5 keV, the non-thermal contribution comes down to 33 %. This is indeed a large fraction of the total continuum emission, but not as large as the 93% suggested by extrapolation of the hard X-ray power-law. The reason for this is probably that the true spectral shapes are not exactly power-laws, but steepen at higher energies. So apparently, in

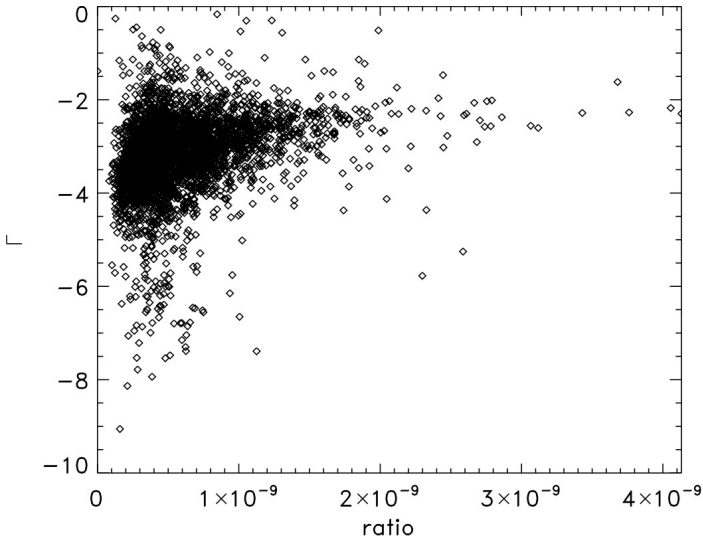

Figure 2.7: On the x-axis is the ratio of continuum over broadband in arbitrary units (the same units as in Fig. 2.6, right image), a higher value means relatively more continuum. On the y-axis the fitted powerlaw indices of the corresponding bins.

the Chandra band the addition of soft thermal emission and hard non-thermal gives by coincidence almost the same power law index, as the steepening non-thermal spectra at high energies. The lack of an obvious spectral break is probably due to the variation in power law indices for the non-thermal spectra, and the variation in cut-off energies across the remnant.

2.4.1 West side of Cas A

So far, we have shown that a large part of the non-thermal emission is associated with the reverse shock region and that most of this emission is coming the Western part of the remnant. This prompted us to investigate the spectrum of the Western part more closely. Specifically we were interested in whether the reverse shock in the Western part shocks the less dense material. The reason is that the Western region not only shows more non-thermal emission, but there also seems to be less thermal emission. A low density of a shocked material results, apart from less flux from shock-heated plasma, also in a short ionization time scale, $n_e t$. With this in mind, we extracted spectra from one of the featureless filaments, located at the reverse shock. This is the same filament as used by Hughes et al. (2000a) (filament 'D'). We extracted the spectrum of this region in the individual eventfiles of the megasecond image and added them with the `addspec` tool of ftools in heasoft.

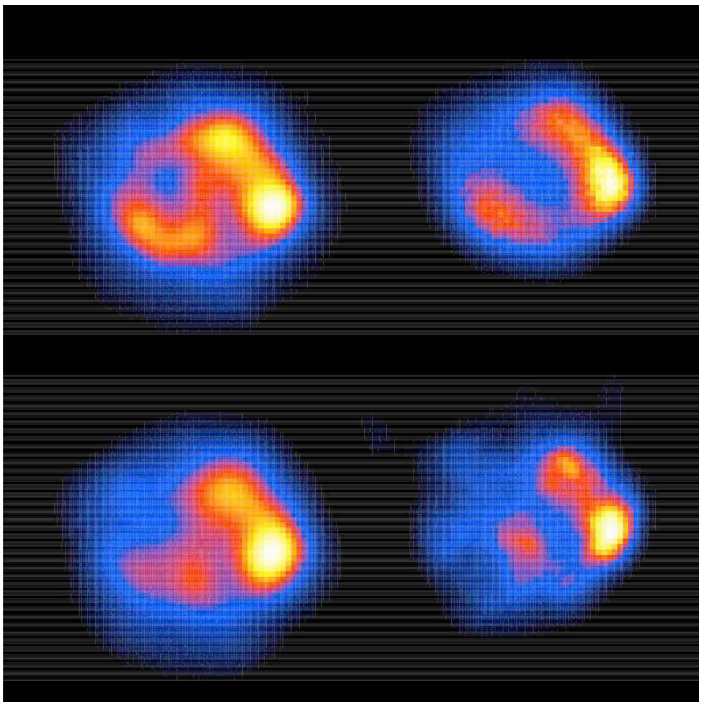

Figure 2.8: The upper row is a Chandra image of Cas A in the 4 to 6 keV band, convolved to the BeppoSAX resolution (left) and the BeppoSAX image of Cas A in the same energy band (right). The second row has on the left side the image of Fig. 2.6, extrapolated to 9 to 11 keV (Fig. 2.9) and convolved to the BeppoSAX resolution. The right image shows the actual BeppoSAX image in the 9 to 11 keV band. The extrapolation matches qualitatively the BeppoSAX image and therefore, the powerlaw fits, give a reasonable prediction of the hard X-ray image of Cas A.

We fit the resulting spectrum with a model consisting of a power-law and the non-equilibrium ionization (NEI) model of SPEX (Kaastra et al. 1996). The best fit parameters are listed in Table 2.1.

Previous studies (Keohane 1996; Willingale et al. 2002) show that the absorption in the West side is higher than in the East, with values up to 1.7 $\times 10^{22}$ cm^{-2}. So a value of 1.67 $\times 10^{22}$ cm^{-2} is still within the expectations.

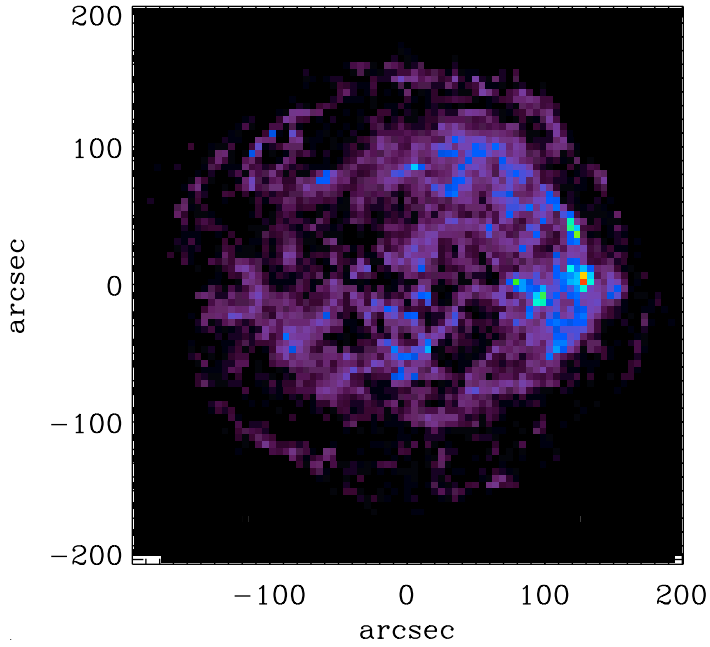

Figure 2.9: An extapolation of the best fit power-laws from Fig. 2.6 to the 9 to 11 keV band

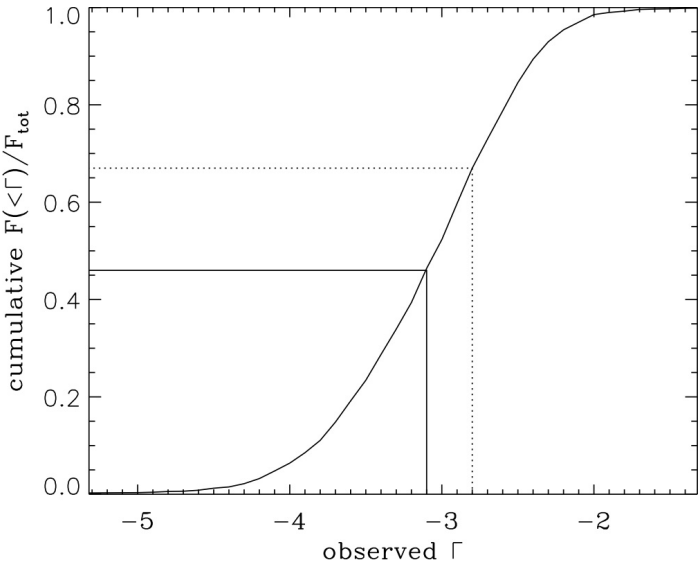

Figure 2.10: A plot of the cumulative flux between 4.2 and 6 keV versus the best-fit powerlaw index as found in Fig 2.6. The solid line shows that 46% of the flux has a power-law index steeper than -3.1. The dotted line shows that 33% of the flux has a power-law flatter than -2.8; the power-law index associated with a thermal bremsstrahlung model with kT = 3.5 keV.

Table 2.1: Results of the spectral fit to the featureless filament

Parameter	Value
n_H (cm^{-2})	$1.67^{+0.03}_{-0.03} \times 10^{22}$
$n_e t$ (cm^{-3} s)	$8.6^{+1.0}_{-1.0} \times 10^{10}$
Γ	$2.09^{+0.07}_{-0.07}$
F_{pow}/F_{nei} ($E \in [0.4\ keV, 8\ keV]$)	2.23
χ^2/d.o.f	283/145

2.5 Discussion

Using a combination of deprojection and characterization of the X-ray continuum power-law slope of the one megasecond Chandra observation, we have determined the location of the non-thermal X-ray emission of Cas A. We have found that a significant fraction of the X-ray continuum emission is coming from two separate rings; one can be identified with the forward shock, the other with the shell dominated by bright ejecta. About 54% of all continuum emission in the 4.2 to 6 keV band is likely to be non-thermal.

The non-thermal emission from the forward shock is likely due to synchrotron radiation from electrons accelerated at the forward shock, confined to the forward shock region by synchrotron cooling (Vink & Laming 2003; Berezhko & Völk 2004). However, the non-thermal emission of Cas A as a whole is dominated by the contribution of the inner ring. This inner region of emission is shifted to the West of the remnant by $\sim 15''$. A similar shift was found for the location of the reverse shock by Reed et al. (1995); Gotthelf et al. (2001), on the basis of optical data and a deprojection of radio data and a 50 ks Chandra observation, in the Si band. Gotthelf et al. (2001) also found marginal evidence for a higher emissivity at the reverse shock in the 4 to 6 keV band using the 50 ks Chandra observation.

2.5.1 Nature and location of the inner non-thermal emission

Since some of the spectra in the West hardly show any line emission, we think it is likely that this is synchrotron emission, since non-thermal bremsstrahlung without line emission is hard to establish, unless one has peculiar abundances. Such a bremsstrahlung model was once invoked for SN1006 (Hamilton et al. 1986), but has now been abandoned in favor of synchrotron emission. Furthermore, a recent paper by Vink (2008b) shows that electrons with energies close to the thermal electron energy distribution, lose their energy relatively fast due to Coulomb losses. This process is already important in the Chandra energy band for $n_e t < 8.6 \times 10^{10} \mathrm{cm}^{-3}\mathrm{s}$; the value reported here for a filament, dominated by

continuum emission in the West (section 2.4.1, Table 2.1). For $n_{\rm e}t \sim 10^{11}{\rm cm}^{-3}{\rm s}$, typical for Cas A (Willingale et al. 2002), one only expects to see non-thermal bremsstrahlung for photon energies $\gtrsim 100$ keV.

When it comes to the location of the synchrotron emission, there are two possibilities: the reverse shock and the contact discontinuity. The contact discontinuity marks the border between shocked ejecta and shocked circumstellar medium. Hydrodynamical solutions show that the density and the magnetic field peak at this radius (Chevalier 1982; Lyutikov & Pohl 2004). For a supernova remnant evolving in a stellar wind, the contact discontinuity is close to the reverse shock. So from our deprojections it difficult to judge whether the X-ray synchrotron emission is coming from the reverse shock or the contact discontinuity. It is unlikely that electrons are accelerated to TeV energies at the contact discontinuity, since no viable acceleration mechanism is known (however, see Lyutikov & Pohl 2004), but there are two ways of generating X-ray synchrotron emission at the contact discontinuity: 1) Due to an increase of the magnetic field, electrons with relatively low energies suddenly light up in X-rays. 2) High energy electrons and positrons are created through the decay of charged pions ($\pi^{\pm}$), caused by hadronic cosmic ray collisions (Gaisser 1990). Charged pions decay into muons and muon neutrinos. The muons decay into electrons/positrons and electron and muon neutrinos. The electrons and positrons thus created are often called secondary electrons and positrons.

For option 1: For synchrotron radiation the relation between electron energy and photon energy is

$$E_{\rm ph} = 19 E_{\rm TeV}^2 B_{\rm G} \text{ keV} \tag{2.3}$$

(Ginzburg & Syrovatskii 1965). For electrons to be invisible in X-ray synchrotron radiation, the peak energy should be an order of magnitude lower than the X-ray continuum at 4-6 keV. Therefore, the magnetic field should increase an order of magnitude at the contact discontinuity. As an example, an electron, accelerated at the forward shock, with an energy of 3 TeV in the typical magnetic field of Cas A of 0.5 mG, typically emits photons of 0.09 keV. When this electron suddenly enters a region of 5 mG, it will emit photons of typically 1 keV; detectable in X-rays. However, the synchrotron loss time for such an electron in a 0.5 mG magnetic field, 18 years, is rather short compared to the age of Cas A. In this time the particle has to diffuse from the forward shock region to the contact discontinuity, which is about 0.5 pc, for a distance to Cas A of 3.4 kpc (Reed et al. 1995). For 3 TeV and B=0.5 mG the diffusion constant is $D = \eta \cdot 2 \times 10^{23}$ cm^{2}s^{-1}, with $\eta = 1$ corresponding to Bohm diffusion (Malkov & Drury 2001). In 18 yr a particle can diffuse by $R \approx \sqrt{2Dt} = 5 \times 10^{-3}\sqrt{\eta}$ pc. In other words, this model only works if the magnetic field turbulence is very low, corresponding to $\eta > 10000$. This unlikely, since the ample presence of cosmic rays results in magnetic field turbulence. Moreover, at the shock front $\eta \sim 1$ (Vink 2006; Stage et al. 2006). For low values of η, the diffusion length ($l_{\rm diff}$ the length for which advection dominates

over diffusion), is short: $l_{\rm diff} = \eta 4.5 \times 10^{-4}$ parsec. So, for low η, the advection velocity, ($u = v_{\rm fs}/4$, with $v_{\rm fs}$ the forward shock velocity) is the relevant velocity. For a $v_{\rm fs}$ of 5800 km s^{-1}, $u = 1450$ km s^{-1}. Using this velocity, it takes 674 years to go from the forward shock to the contact discontinuity, longer than the synchrotron loss time of 18 years.

It has been argued that the magnetic field at the shock front is high, but rapidly decays towards the inside (Pohl et al. 2005), increasing the synchrotron loss times, and increasing the diffusion constant. However, the decay in magnetic field should be reflected in the radio emissivity from the forward shock to the inside, which is contrary to observations, that show gradual increase in emissivity toward the center starting at the shock front (Gotthelf et al. 2001).

For option 2 (secondary electrons): if the X-ray synchrotron emission from the inside is due to secondary electrons, this would be an important discovery. It would be evidence for the presence of TeV ion cosmic rays. Neutral pions (π^0) are made in comparable quantities to charged pions. The power in secondary electrons should therefore be comparable to the luminosity in pion decay. In order to compare the fluxes from X-ray synchrotron and γ-ray radiation one should take into account the conversion from pion energy (π^0 & $\pi^{\pm}$) to photon energies, both in the TeV band (through π^0 decay) and in the X-ray band, due to synchrotron radiation from secondary electrons. Taking into account these various decay channels, one finds that $E_{\rm ph} \sim 20 E^2_{\gamma{\rm TeV}} B_{\rm G}$ keV [4], so the X-ray synchrotron flux above 4 keV should correspond to roughly the γ-ray flux above 20 TeV. We found for the X-ray synchrotron flux above 4 keV $2.7{\times}10^{-10}$ erg s^{-1}cm^{-2}. This is a factor 130 higher than the γ-ray flux above 1 TeV, which we calculated to be 2.1×10^{-12} erg cm^{-2} s^{-1} using the photon-flux and photon index above 1 TeV reported by the MAGIC collaboration (Albert et al. 2007). Since we should actually have evaluated the flux above 20 TeV, we can rule out that the X-ray synchrotron emission is caused by secondary electrons.

In our view it is therefore most likely that the X-ray synchrotron emission is caused by electrons accelerated at the reverse shock. Similarly to the forward shock region the electrons are likely to be confined to a region near the shock itself. For a long time the reverse shock as location for acceleration has been neglected, because of its putative low magnetic field. Moreover, the abundance pattern of cosmic rays is consistent with acceleration from plasmas with solar abundances (Hörandel 2008). As far as the magnetic field is concerned, however, Ellison et al. (2005) have argued that if magnetic field amplification (Bell & Lucek 2001) works at the forward shock it is likely to operate at the reverse shock as well. Also for

[4] The decay product of π^0 decay is two photons, with each, on average, an energy $E_{\gamma{\rm TeV}} = 0.5 E_{\pi^0}$. For the charged pions, $\pi^{\pm}$, the final decay product consists of electrons (positrons) and neutrinos ($\pi^{\pm} \rightarrow \mu^{\pm} + \nu_{\mu}(\bar{\nu}_{\mu})$, $\mu^{\pm} \rightarrow e^{\pm} + \nu_e(\bar{\nu}_e) + \nu_{\mu}(\bar{\nu}_{\mu})$). In this case the final electron or positron also take up, on average, half the initial pion energy $E_{e^{\pm}} \approx 0.5 E_{\pi^{\pm}}$; hence, for a given pion energy, $E_{e^{\pm}} \approx E_{\gamma{\rm TeV}}$. This electron or positron emits synchrotron radiation at a peak frequency given by Eq. 2.3. Hence the close resemblance of this equation with Eq. 2.3.

the SNR RCW 86 it has been suggested that the X-ray synchrotron emission in the Southwest of the remnant is coming from electrons accelerated at the reverse shock (Rho et al. 2002).

2.5.2 Reverse shock velocity in the West and the presence of synchrotron emission

The presence of X-ray synchrotron radiation from shock accelerated electrons is only expected if the shock velocity is high enough: shock acceleration theory predicts for the maximum photon energies (Aharonian & Atoyan 1999):

$$E_{\rm ph} = 0.5\eta^{-1}\left(\frac{v_{\rm s}}{2000\ {\rm kms}^{-1}}\right)^2\ {\rm keV}, \tag{2.4}$$

with v_s the shock velocity. Note that the photon energy is independent of the magnetic field. For the reverse shock the velocity in Eq. 2.4 refers to the shock speed in the frame of the ejecta. The ejecta velocity is equal to the free expansion velocity $v_{\rm f,ej} = r_{\rm ej}/t$. For the reverse shock the shock velocity as seen by the ejecta is therefore $v_{\rm s,ej} = v_{\rm f,ej} - v_{\rm s,obs}$, with $v_{\rm s,obs}$ the shock velocity in the frame of the observer. The presence of X-ray synchrotron radiation from the reverse shock in the Western half of Cas A suggests a higher reverse shock velocity than in the rest of the remnant. Proper motions of knots at the inside of Cas A in X-rays were most recently measured by DeLaney et al. (2004), but some details of the measurements, including measurements of the proper motions as a function of azimuth, only appeared in appendix 4.4 of Delaney (2004, Fig. 4.6). In this Figure, we see that in the West the expansion rate is between -0.1%yr^{-1} and 0.1%$^{-1}$ this corresponds to $v_{\rm r,ob}$ at the reverse shock of approximately -2000 km s^{-1} to 2000 km s^{-1}, implying a shock velocity [5] $v_{\rm s,ej} \approx 3900 - 7900$ km s^{-1}. In the Northern and Eastern part of Cas A, Delaney (2004) finds expansion rates of 0.2%yr^{-1}, corresponding to $v_{\rm r,ob} \approx 4000$ km s^{-1} and a shock velocity of $v_{\rm s,ej} \approx 1900$ km s^{-1} at the reverse shock.

In the optical Morse et al. (2004) reports a shock velocity of $v_{\rm s,ej} \approx 3000$ km s^{-1} for a filament in the Northwest. In our maps (Fig. 2.6 left) we find that this region has a hard power law slope, suggesting the presence of synchrotron radiation, but the overall X-ray emission is dominated by thermal X-ray line emission (Fig. 2.6 right).

It indeed looks like the presence of X-ray synchrotron emission from the inner ring corresponds with reverse shock velocities in excess of 2000 km s^{-1}. To some extend this is surprising, since the X-ray synchrotron emissivity function is rather

[5] We have checked this result using the Chandra 1 Ms observation and an observation of Chandra made in 2000 using the procedure described in Vink et al. (1998). We concentrated on filament 'D'. The result confirms the lower expansion or even backward velocities: we found -970 ± 140 km s^{-1}, i.e. the filament seems to move towards the center. This implies a $v_{\rm s,ej} \approx 6900$ km s^{-1}. Vink et al. (1998) already reported a lower expansion for the whole Western part of Cas A.

broad and can result in some synchrotron emission beyond the maximum photon energy as defined in Eq. 2.4. On the other hand, $\eta = 1$ corresponds to Bohm diffusion, and represents the case for maximum acceleration efficiency. The fact that 2000 km s^{-1} seems close to the velocity dividing the presence or absence of X-ray synchrotron radiation again suggests that acceleration takes place close to the Bohm limit. Equation 2.4 suggests that the spectra in the West of the remnant will be harder than in the rest, where $v_{\rm s,ej}$ is lower.

Note that the high reverse shock velocities in the West (and low observed velocities) are not in agreement with analytic hydrodynamic solutions for an SNR evolving in a stellar wind (Laming & Hwang 2003). Adapting the parameters of this model such that the forward shock radius and velocity and the reverse shock radius, match those of Cas A, we find $v_{\rm s,ej}$ ranging between 1600-2300 km s^{-1}, significantly lower than in the West, but in agreement with those in the Eastern part of Cas A. This suggests that the circumstellar density structure is more complex in the West.

2.6 Conclusions

We have presented an anaysis of the spatial and spectral variation of the X-ray continuum emission of Cas A, based on the 1 Ms Chandra observation. We find that harder continuum spectra are associated with the filaments, dominated by continuum emission, suggesting that the harder spectra are caused by non-thermal radiation. A dominant fraction of the non-thermal emission appears to come from the reverse shock region. We have discussed various options for the nature of the non-thermal emission and its origins. Some of our conclusions were independently also obtained by Uchiyama & Aharonian (2008), but based on X-ray variability. Based on our analysis and discussion we come to the following conclusions:

- The power-law index of the spectrum between 4.2-6.0 keV is an indicator for X-ray synchrotron emission: there is a correlation between filaments, dominated by continuum emission and hard spectra.
- Hard X-ray spectra are not exclusively associated with filaments, dominated by continuum emission, suggesting that non-thermal emission comes also from other regions,
- The non-thermal X-ray emission is likely to be synchrotron radiation.
- The non-thermal accounts for about 54% of the overall continuum emission in the 4-6 keV band.
- In the Western part of Cas A, most X-ray synchrotron comes from the reverse shock.

– The dominance of X-ray synchrotron emission from the West is probably the result of a locally higher reverse shock velocity of $v_s \sim 6000$ km s^{-1} (corresponding to a lower proper motion) than in the Eastern region ($v_s \sim 1900$ km s^{-1}).

2.7 Acknowledgments

We want to thank Tracey DeLaney for providing us with a recent radio map of Cas A. We would like to thank Frank Verbunt for carefully reading the manuscript and Michele Cappellari for the software we used to display some of our results. This work is supported by the NWO-VIDI grant of J.V.

3

Measuring the cosmic-ray acceleration efficiency of a supernova remnant

E.A. Helder, J. Vink, C.G. Bassa, A. Bamba, J.A.M. Bleeker,
S. Funk, P. Ghavamian, K. J. van der Heyden, F. Verbunt
and R. Yamazaki
Science, 2009, 325, 719

COSMIC rays are the most energetic particles arriving at earth. Although most of them are thought to be accelerated by supernova remnants, the details of the acceleration process and its efficiency are not well determined. Here we show that the pressure induced by cosmic rays exceeds the thermal pressure behind the northeast shock of the supernova remnant RCW 86, where the X-ray emission is dominated by synchrotron radiation from ultra-relativistic electrons. We determined the cosmic-ray content from the thermal Doppler broadening measured with optical spectroscopy, combined with a proper-motion study in X-rays. The measured post-shock proton temperature in combination with the shock velocity does not agree with standard shock heating, implying that $>$50% of the post-shock pressure is produced by cosmic rays.

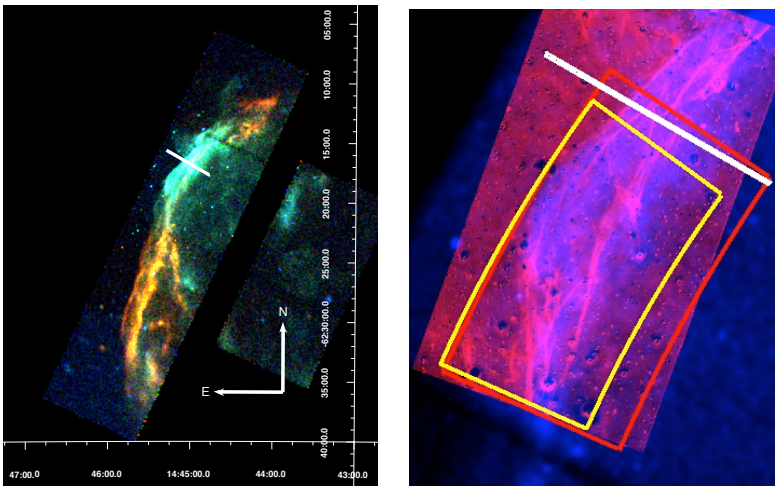

Fig. 3.1: (**Left**) The eastern rim of RCW 86, as observed in 2007 with Chandra. Red indicates the 0.5-1.0 keV band, green the 1.0-1.95 keV band and blue shows the 1.95-6.0 keV band. The northern part has relatively more flux in the higher energy bands, which is characteristic for synchrotron emission. (**Right**) Blue is the broadband keV Chandra image, red is the image as observed with the VLT through a narrow Hα filter. The regions (yellow and red) indicate where we measured the proper motion. In both panels the location where we took the optical spectrum is indicated with a white line.

3.1 Introduction

The main candidates for accelerating cosmic rays up to at least 10^{15} eV are shell-type supernova remnants (SNRs), which are the hot, expanding plasma shells, caused by exploded stars (supernovas). In order to maintain the cosmic-ray energy density in the Galaxy, about 3 supernovae per century should transform 10 percent of their kinetic energy in cosmic-ray energy. Indeed, $\sim 10^{14}$ eV electrons have been detected at forward shocks (Koyama et al. 1995; Bamba et al. 2005) and possibly at reverse shocks (Rho et al. 2002; Helder & Vink 2008) of several shell-type remnants by their X-ray synchrotron emission, and particles with TeV energies have been detected in several SNRs by Cherenkov telescopes (Aharonian et al. 2004; Albert et al. 2007).

If SNRs transform a substantial amount of their kinetic energy into cosmic rays, this should affect the kinematics of the remnant. One imprint of energy losses by cosmic rays is a higher compression factor of the post-shock plasma (Berezhko & Ellison 1999), for which indications have been found in both the Tycho SNR

and SN 1006 (Warren et al. 2005; Cassam-Chenaï et al. 2008). Another signature of a substantial cosmic-ray energy density is a lower post-shock temperature (Decourchelle et al. 2000; Vink 2008a; Drury et al. 2009; Patnaude et al. 2009). For shocks with conservation of mass, momentum and energy, in absence of cosmic rays, the post-shock temperature (T_i) for species with mass m_i relates to the shock velocity (v_s) as

$$kT_i = \frac{3}{16} m_i v_s^2 \tag{3.1}$$

in case of no thermal equilibrium (i.e. the several atomic species do not have the same temperature), in which case protons carry most of the thermal energy. In case of fast thermal equilibration, this relation reads $kT = \frac{3}{16}\mu m_{\rm p} v_s^2$ ($\mu \simeq 0.6$ for cosmic abundances). Indications for a lower post-shock electron temperature have been found in the Magellanic Cloud remnant 1E 0102-72 (Hughes et al. 2000b). Thermal electrons may constitute only a minor part of the thermal pressure. Here we derive the post-shock proton temperature and the shock velocity of the northeast rim of the shell-type SNR RCW 86 based on optical and X-ray observations.

RCW 86 [1] was detected in TeV energies by the H.E.S.S. telescope (Aharonian et al. 2009) and is probably the remnant of the supernova witnessed by Chinese astronomers in 185 A.D. (Stephenson & Green 2002; Vink et al. 2006). It has been suggested that it evolves inside a stellar-wind blown cavity, where the southwest corner has already hit the cavity wall (Vink et al. 1997). The northeast side still expands in a less dense medium and its X-ray spectrum is dominated by synchrotron radiation, which is an indication for efficient cosmic-ray acceleration.

The optical spectrum of the northeast rim of RCW 86 is dominated by hydrogen lines, with no [NII] line emission (Chevalier et al. 1980). The lack of [NII] indicates that the hydrogen line emission is not a result of strong cooling, but results from excitation processes immediately behind the shock front. The hydrogen lines from these shocks consist of two superimposed Gaussian line profiles: one, caused by direct excitation, has the thermal width of the interstellar medium (ISM), the other is emitted after charge exchange between hot post-shock protons and cold incoming neutral hydrogen and hence has the thermal width of the post-shock protons. Hα emission and efficient cosmic-ray acceleration are likely to anti-correlate because incoming neutral species are likely to damp plasma waves, which are essential for shock acceleration (Drury et al. 1996) and because cosmic rays escaping ahead of the shock ionize the surrounding ISM and decrease the amount of Hα emission. In RCW 86 the Hα emission occurs all along the rim, including, although with weak emission, the parts coinciding with X-ray synchrotron emission, where efficient cosmic-ray acceleration is likely to occur (Fig. 1). The only other remnant in which Hα emission is seen all along the shell, including regions with X-ray synchrotron emission, is the SN 1006 SNR (Winkler

[1] G315.4-2.3, MSH 14-63

et al. 2003).

The right panel in Figure 1 shows both the Hα and the X-ray emission of the northeast rim of RCW 86. The Hα emission marks the onset of the X-ray synchrotron radiation, which indicates that they are from the same physical system.

3.2 Post-shock proton temperature based on the optical spectrum

In order to measure the proton temperature, we used long-slit spectra obtained with the visual and near ultraviolet FOcal Reducer and low dispersion Spectrograph (FORS2) instrument on the Very Large Telescope (VLT, Appenzeller et al. 1998). We first imaged the northeast side of RCW 86, where the X-ray spectrum is dominated by synchrotron emission. Using this image as a guide, we pointed the slit at a location where the Hα emission is bright (Fig. 1, Table S1).

The spectrum's (Fig.2) measured full width at a half of the maximum (FWHM) is 1100 ± 63 km/s (see the appendix for further details) corresponding to a $\sigma_v = 467 \pm 27$ km/s and implying a post-shock temperature of 2.3 ± 0.3 keV.

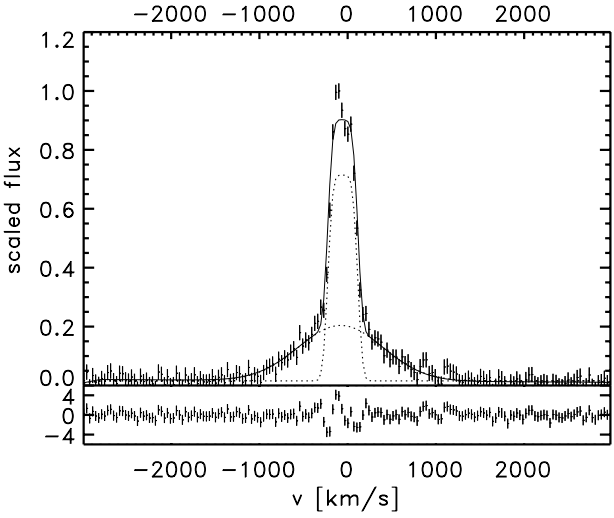

Fig. 3.2: The Hα spectrum, with broad and narrow components (dotted). The best fitting spectrum is overplotted. The lower panel shows the residuals divided by the errors.

3.3 Proper motion based on X-ray data

To measure the shock velocity of the northeast rim of RCW 86, we observed it with the Chandra X-ray observatory in June 2007, and matched it with an observation taken in June 2004 (Vink et al. 2006). To make both observations as similar as possible, we used the same observation parameters as in 2004 (Table S2).

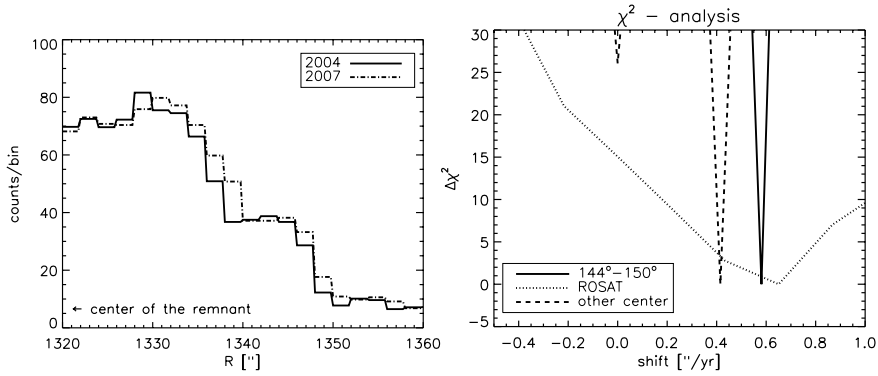

Fig. 3.3: (**Left**) Steep gradient in the radial profiles for the 2004 and 2007 observations, adaptively binned with the Haar method(Starck et al. 1998), so that each bin has a signal to noise ratio of at least 4, with a maximum bin width of $2''$. (**Right**) χ^2 statistics of the proper motion measurement. (Details of the used radial profiles in SOM).

We measured the proper motion of the shock at the location of the slit of the Hα spectrum by comparing the positions of the shock in the two images (see the appendix for further details). A solid estimate of the proper motion is $1.5 \pm 0.5''$ in 3 years time (Fig. 3 and S1), implying a shock velocity of $(6.0 \pm 2.0) \times 10^3$ km/s at a distance of 2.5 kpc (Rosado et al. 1996; Sollerman et al. 2003). The statistical error on the measured expansion is of the order of $0.2''$. However, in the process of calculating the proper motions, we found that small details, such as slightly changing the angle in which we made the profile, tended to give a different proper motion, with a difference larger than the $0.2''$ statistical error we measured. However, in none of the measurements, did we find a proper motion below $1.0''$. Because the proper motion is higher than expected (Vink et al. 2006), we verified that it is consistent with data taken in 1993 with the Position Sensitive Proportional Counter (PSPC) on board the ROentgen SATellite (ROSAT) compared with the 2007 observation (Fig. 3 and S1). Although the proper motion, using the nominal pointing of the ROSAT PSPC, is statistically highly significant, the large pointing error of ROSAT ($\sim 4''$) results in a detection of the proper motion at the 2σ level.

3.4 Discussion

Compared to other remnants of a similar age, the shock velocity is surprisingly high. Recent models (Dwarkadas 2005) predict $v_{\rm s} \sim 5000$ km s^{-1} after 2000 years for SNRs evolving in a wind blown bubble [2]. This fits with the scenario where RCW 86 is evolving in a cavity and the southwest corner, which has a slower shock velocity (Long & Blair 1990; Ghavamian et al. 2001) and a mostly thermal (Rho et al. 2002) X-ray spectrum, has already hit the cavity shell. Shock acceleration theory suggests that only shocks with velocities exceeding 2000 km s^{-1} emit X-ray synchrotron emission (Aharonian & Atoyan 1999; Vink et al. 2006), which is also consistent with observations (Katsuda et al. 2008).

An additional uncertainty in the shock velocity is in the distance to RCW 86, which is based on converging but indirect lines of evidence. RCW 86 was found to be in the same direction as an OB association, at a distance of 2.5 kpc (Westerlund 1969). Because high mass stars are often found in such associations, the progenitor of RCW 86 may well have formed in this one, provided that RCW 86 is the remnant of an exploded massive star. Other studies (Rosado et al. 1996; Sollerman et al. 2003) found a distance of 2.3 and 2.8 kpc respectively, based on the line-of-sight velocity of ISM swept up by the remnant, combined with an observationally determined rotation curve of the Galaxy (Brand & Blitz 1993). The third argument supporting a distance of 2.5 kpc is the molecular supershell seen in CO emission in the direction of RCW 86, whose line-of-sight velocity agrees with that of RCW 86 (Matsunaga et al. 2001). In further calculations, we take the distance towards RCW 86 to be 2.5 $\pm$ 0.5 kpc, leading to a shock velocity of 6000 ± 2800 km/s.

The relation between shock velocity and measured post-shock proton temperature has been extensively studied (Chevalier et al. 1980; Ghavamian et al. 2001; Heng & McCray 2007; van Adelsberg et al. 2008; Ghavamian et al. 2007b), including the cross sections for excitation and charge exchange as function of $v_{\rm s}$. Although recent studies show that there can be a substantial effect of cosmic rays on the post-shock proton spectrum (Raymond et al. 2008), up to now, there was no need to include cosmic-ray acceleration in the interpretation of the post-shock temperature. This is possibly because most of the Hα spectra are taken from the brightest rims of SNRs. Because Hα emission and efficient cosmic-ray acceleration are likely to anti-correlate (Drury et al. 1996), these rims probably have low cosmic-ray acceleration efficiency. A possible exception is 'knot g' in the Tycho SNR, where indications for cosmic-ray acceleration in the form of a precursor have been found (Ghavamian et al. 2000; Lee et al. 2007; Wagner et al. 2009). Additionally, for some SNRs (Winkler et al. 2003; Smith et al. 1991) the distance has been determined using the post-shock proton temperature in combination with

[2] The effects of cosmic ray acceleration on the evolution of the forward shock are small, see Patnaude et al. (2009)

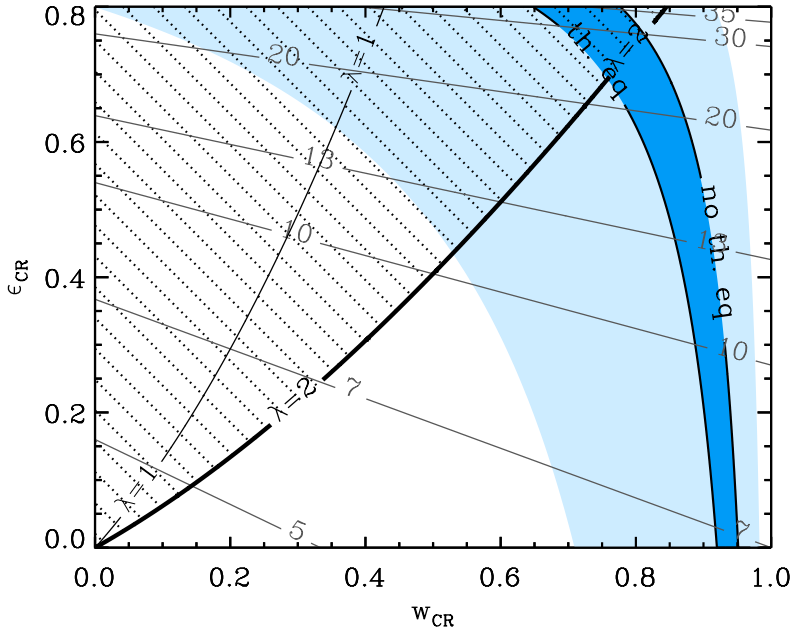

Fig. 3.4: The dark blue area is the area allowed according to the modified equations, limited by full thermal equilibrium and no thermal equilibrium for the nominal values of kT =2.3 keV, $v_{\rm s}$ = 6000 km/s. The light blue area shows the area of the kT and $v_{\rm s}$ with all uncertainties taken into account. The thin lines indicate the compression ratio (χ) of the post-shock plasma. Within the allowed region, $\lambda = 2$ line provides an upper limit on $\epsilon_{\rm CR}$ and a lower limit on $w_{\rm CR}$.

the proper motion, using theoretical models which do not take into account energy losses and cosmic-ray pressure. This procedure leads to an underestimate of the distance if cosmic-ray acceleration is present. Thus, unless the distance is accurately determined in an independent way, there will be no discrepancy between the predicted $v_{\rm s}$, based on kT and Eq. 3.1 and the actual shock velocity.

The shock velocity of the X-ray synchrotron rim implies a post-shock temperature of 70 keV (assuming no thermal equilibrium), 42 keV (assuming equilibrium), whereas the measured post-shock temperature is 2.3 keV. This measurement is at least a factor 18 less than the post-shock temperature estimated from the shock velocity, which can now be used to constrain current theoretical shock heating models (Drury et al. 2009; Patnaude et al. 2009). Additionally, this proton temperature is close to the electron temperature at the same location (Vink et al. 2006), implying fast thermal equilibration between both species, breaking the trend be-

tween the shock velocity and the measure of thermal equilibrium seen in previous observations (Ghavamian et al. 2007b; van Adelsberg et al. 2008).

To translate this discrepancy into the energy and pressure in cosmic rays, we followed the approach of Vink (2008a), which is based on standard shock equations for plane-parallel, steady-state shocks, modified by additional pressure and loss terms (see also Chevalier 1983; Berezhko & Ellison 1999; Bykov et al. 2008). The loss term is defined in terms of the incoming energy flux: $\epsilon_{\rm CR} \equiv F_{\rm CR}/\frac{1}{2}\rho_0 v_{\rm s}^3$, $F_{\rm CR}$ is the amount of energy flux in cosmic rays which escapes from the system and ρ_0 is the pre-shock density. The parameter which indicates the fraction of the pressure residing in cosmic rays in the total post-shock pressure is $w_{\rm CR}$ ($w_{\rm CR} \equiv P_{\rm NT}/(P_{\rm T} + P_{\rm NT})$, with $P_{\rm T}$ the pressure in particles with a thermal and $P_{\rm NT}$ with a non-thermal energy distribution (i.e. CRs). We plot the modified equations (listed in the supporting online material) in Figure 4 and indicate the region where the combination of kT and v_s of the northern rim of RCW 86 resides for thermal equilibrium as well as for no thermal equilibrium. As Figure 4 shows, a post-shock temperature and a shock velocity do not give a unique solution for $w_{\rm CR}$ and $\epsilon_{\rm CR}$. However, the cosmic rays significantly change the shock dynamics, because the combination solution is far away from $w_{\rm CR} = 0$ and $\epsilon_{\rm CR} = 0$ (Fig. 4).

There are two ways to further constrain $w_{\rm CR}$ and $\epsilon_{\rm CR}$. First, an additional estimate of the compression ratio (χ) of the post-shock plasma would exactly determine $w_{\rm CR}$ and $\epsilon_{\rm CR}$. For certain SNRs this is done by determining the distance between the supernova ejecta and the outer shock; a higher compression ratio implies that the swept-up ISM forms a thinner shell and hence the ejecta will be closer to the shock front (Warren et al. 2005; Cassam-Chenaï et al. 2008). However, ejecta and swept-up ISM are only distinguished by their thermal spectra, which is (almost) absent in the X-ray synchrotron dominated rim ($\sim 15\%$ of the total X-ray emission (Vink et al. 2006)).

An other way is to invoke a dependency of $w_{\rm CR}$ on $\epsilon_{\rm CR}$. According to non-linear shock acceleration theory (Malkov & Drury 2001; Drury et al. 2009), $\epsilon_{\rm CR}/w_{\rm CR} = \frac{2}{\lambda}(1 - 1/\chi)^2$, in which χ is the compression ratio of the post-shock plasma and $\lambda = 1, 2$ indicates the $(w_{\rm CR}, \epsilon_{\rm CR})$ relation for a cosmic-ray spectrum with $f(p) \propto p^{-3.}, p^{-3.5}$ respectively, with p the momentum of the cosmic rays. The $\lambda = 2$ line gives an upper limit to the energy losses, since it is valid for the most efficient cosmic-ray acceleration by cosmic-ray modified shocks (Malkov 1999). For $f(p) \propto p^{-4}$, $\lambda = ln(p_{\rm max}/mc)$ (Drury et al. 2009) which can be large and does not provide a lower limit to $\epsilon_{\rm CR}$. Taking the $\lambda = 2$ line as an upper limit for $\epsilon_{\rm CR}$, we find a value for $w_{\rm CR}$ of $\geq 50\%$. One remaining question is whether we should include the effects of the turbulent magnetic field. The average magnetic field pressure in RCW 86 has been estimated to be $P_B = B^2/8\pi = 2.3 \times 10^{-11}$dyn cm^{-2}, for a magnetic field of 24 μG (Vink et al. 2006). This is an order of magnitude below the thermal pressure, which we esti-

mate to be $P_T = nkT = 3.7 \times 10^{-10}$dyn cm^{-2}, for n = 0.1 (Vink et al. 2006) and kT = 2.3 keV. In reality, the magnetic field pressure may be higher if one takes full account of its unknown, turbulent spectrum.

3.5 Conclusions

In summary, our observations show that the post-shock temperature of the north-east rim of RCW 86 is lower than expected from standard shock relations using the measured shock velocity. The high velocity (6000 ± 2800 km/s) of the shock implies a local low ISM density, which can be expected in a cavity blown by a stellar wind. Cosmic-ray acceleration decreases the post-shock proton temperature in RCW 86 by a factor of 18, implying that $\geq 50\%$ of the post-shock pressure is due to cosmic rays.

3.6 Acknowledgements

We wish to thank A. Achterberg for a useful discussion on the current literature on the theory of shock heating. EH and JV are supported by the Vidi grant of JV from the Netherlands Organization for Scientific Research (NWO). This work was supported in part by Grant-in-Aid for Scientific Research of the Japanese Ministry of Education, Culture, Sports, Science and Technology, no. 194014 (AB) and no. 19047004 and no. 21740184 (RY). SF is supported by SAO grant G07-8073X. PG is supported by the STScI grant GO-11184.07. This paper is based in part on observations made with ESO Telescopes at the Paranal Observatories under programme ID 079.D-0735.

3.A Appendix

3.A.1 VLT spectra

Table 3.1 lists observational characteristics of the VLT observation. To reduce the data, we first calculated for each pixel the median signal in a square of 5×5 pixels around it. Then, the pixels which had a higher value than 2× the median were flagged as cosmic-ray pixels, and are not used in the following calculations. We removed the skylines by fitting a 3$^{\rm rd}$ order polynomial[3] to the spectrum in the spatial direction for each wavelength coordinate. Furthermore, we calibrated the wavelength using the HeHgCdArNe calibration spectrum. Then, we added the spectra of the 4 observations, resulting in the spectrum shown in Figure 3.2. We fitted this spectrum by minimizing the χ^2, the line profile using two Gaussians, convolved with a hat profile with the width of the slit (2.5″). The errors on the data points are based on the variance of the residuals between the data and the best fit model. This method results by definition in a $\chi^2/\mathrm{d.o.f.} \sim 1$. The brightness of the filaments is $1.0 \pm 0.2 \times 10^{-16}\mathrm{erg\ s^{-1}\ cm^{-2}\ arcsec^{-2}}$.

3.A.2 Expansion measurement & statistics

Table 3.2 lists the observational parameters of both Chandra observations. The data were reduced using the CIAO data reduction package, version 4.0 and the calibration database CALDB 3.4. We turned off the randomization, which is applied during the standard process of generating the event list; combined with the dithering of the telescope this gives a slightly better angular resolution. We checked the registering of the two observations using 9 point sources in the field. The error in the alignment of both pointings is well below 0.1″, which is the value we are using as a systematic error in the proper-motion measurement. From the event list, we made radial surface brightness profiles with bins in the radial direction of 0.25″, using photons with energies between 0.5 and 6.0 keV. We choose the center of the proper motion to be $\alpha = 14^{\rm h}42^{\rm m}31.00^{\rm s}$ and $\delta = -62°29'34.99''$ (J 2000). This is not necessarily the center of the remnant, it is our estimated center of the curvature of the part of the remnant we are interested in. Note that a wrongly chosen center can only result in a lower proper motion of the shock. We calculated the expansion in 2 overlapping regions (Figure 3.1). We implemented the Poisson statistics as follows: for each bin, we calculated the probability that the number of counts in both bins were drawn from the same Poisson distribution. We measure the proper motion by shifting the normalized profiles with respect to each other, with steps of 1 bin and for each shift, we calculate the probability that both profiles were drawn from the same distribution, using the χ^2 and the Poisson maximum likelihood method. Additionally, we used the Kolmogorov Smirnov statistic. For

[3] Or a lower order, depending on whether the fit improved by taking the higher order.

applying the latter, we first made cumulative distributions for the profiles and then calculated the Kolmogorov Smirnov statistic for each shift.

The Kolmogorov-Smirnov statistic does not provide an error on the parameters. To estimate the errors, we simulated 20 radial profiles using the bootstrap method Press et al. (1992), added an artificial proper motion ($1.0''$) and measured this proper motion using the Kolmogorov-Smirnov statistic. The best fit proper motion agrees well with the input value. We use the standard deviation on these best fit proper motions as the 1σ error. In addition, we checked the Poison maximum likelihood estimation and χ^2 statistics in a similar way, resulting in consistent estimates of the artificial proper motion ($1.0'' \pm 0.2''$). Furthermore, we use these simuations to determine the optimum choice for the range in radius. The most reliable results for the proper motion were obtained if we include the whole rim in the radial profile. We validated our result using two independently written computer codes.

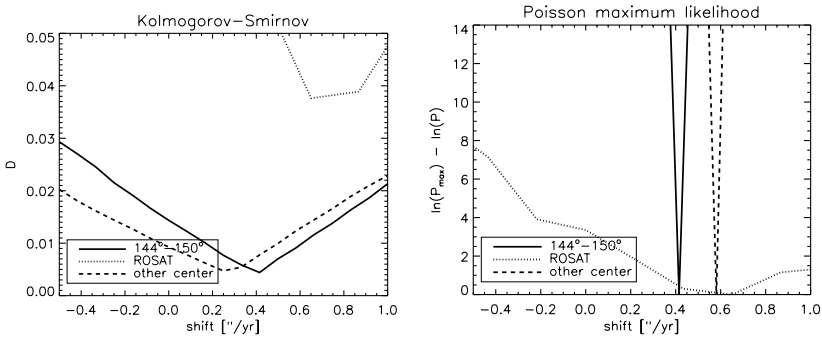

Fig. 3.5: Plotted are the statistics on the proper motion of RCW 86, for both the Kolmogorov Smirnov statistic and the Poisson maximum likelihood estimation. The linestyles denote the same regions as in Figure 3.3. Since the Poisson statistics is a multiplication of the probabilities for each bin, the total probability depends on the number of bins in the profile. We corrected for that by subtracting $ln(P_{\max})$, we multiplied the y-axis with -1, so the best fit solution is a minimum in this plot.

3.A.3 kT and V_s relation

Analytical equations of the post-shock temperature and shock velocity in the presence of cosmic-ray acceleration have been described by several authors (Chevalier 1983; Berezhko & Ellison 1999; Blasi et al. 2005). In this section, we give a summary of the equations used to obtain Figure 3.4. We start out with a relation which

states the conservation of momentum over the shock front:

$$P_2 + \rho_2 u_2^2 = P_0 + \rho_0 u_0^2. \tag{3.2}$$

A '0' subscript means pre-shock and a '2' subscript means post-shock, ρ denotes the density, P the pressure and u the velocity of the gas/plasma in the frame of the shock. Now, we use conservation of mass over the shock: $\rho_0 u_0 = \rho_2 u_2$ and we define the compression ratio $\chi \equiv \rho_2/\rho_0$:

$$P_2 = P_0 + \rho_0 u_0^2 (1 - 1/\chi). \tag{3.3}$$

We introduce $w_{\rm CR} \equiv P_{\rm NT}/(P_{\rm T} + P_{\rm NT}) \rightarrow P_2 = P_{\rm T}/(1 - w_{\rm CR})$. Additionally, we use $P_T = nkT_i$, $\rho = nm_i$ and we assume that the pre-shock pressure is small compared to $\rho_0 u_0^2(1 - 1/\chi)$:

$$kT_i = (1 - w_{\rm CR})\frac{1}{\chi}(1 - 1/\chi) m_i u_0^2. \tag{3.4}$$

Note that for a shock without cosmic-ray pressure ($w_{\rm CR} = 0$) and no energy losses and a non-relativistic gas ($\chi = 4$), we get equation 3.1. To derive the compression ratio χ, we use γ_s; the effective adiabatic index at the shock front. This is defined as (Chevalier 1983):

$$\gamma_s = \frac{5 + 3w_{\rm CR}}{3(1 + w_{\rm CR})}, \tag{3.5}$$

We now use γ_s in the equation for compression ratio including energy losses by cosmic rays, as described in Bykov et al. (2008) and define $G = \frac{3}{2} w_{\rm CR} + \frac{5}{2}$. This gives:

$$\chi = \frac{G + \sqrt{G^2 - (1 - \epsilon_{\rm CR})(2G - 1)}}{1 - \epsilon_{\rm CR}}. \tag{3.6}$$

Table 3.1: Journal of the VLT long slit spectroscopic observations

Pointing	α^1 (J2000)	δ^1 (J2000)	observation date	exposure time	position angle (East of North)
NE	14:45:15.7	-62:16:33.2	05/16/2007	2734 s	240°
	14:45:15.7	-62:16:33.8	07/16/2007	2734 s	240°
	14:45:15.7	-62:16:34.6	07/18/2007	2734 s	240°
	14:45:15.7	-62:16:34.0	07/20/2007	2734 s	240°

[1]Coordinates given are the center of the CCD with which we took the spectrum. The slit, which was not in the middle of the CCD, was laid over the filament with coordinates α = 14:45:02.813, δ =-62:16:33.05 (J 2000).

Table 3.2: Journal of the Chandra observations

ObsID	α (J2000)	δ (J2000)	observation start date	exposure time	Roll angle
4611	14:45:03.60	-62:21:05.56	06/15/2004	69.1 ks	295.16
7642	14:45:04.48	-62:20:40.53	06/20/2007	71.7 ks	299.02

4

The kinematics and chemical stratification of the Type Ia supernova remnant 0519-69.0

D. Kosenko, E.A. Helder and J. Vink
Astronomy & Astrophysics accepted, 2010
ArXiv: 1001.0983

We present a detailed analysis of the XMM-Newton and Chandra X-ray data of the young Type Ia supernova remnant SNR 0519-69.0, which is situated in the Large Magellanic Cloud. We used data from both the Chandra ACIS and XMM-Newton EPIC MOS instruments, and high resolution X-ray spectra obtained with the XMM-Newton reflection grating spectrometer (RGS).

Our analysis of the spatial distribution of X-ray line emission using the Chandra data shows that there is a radial stratification of oxygen, intermediate mass elements (IME) and iron, with the emission from more massive elements peaking more toward the center. Using a deprojection technique we measure a forward shock radius of 4.0 ± 0.3 pc and a reverse shock radius of 2.7 ± 0.4 pc.

We took the observed stratification of the shocked ejecta into account in the modeling of the X-ray spectra, for which we used multi-component non-equilibrium ionization models, with the components corresponding to layers dominated by one or two elements. An additional component was added in order to represent the shocked interstellar medium, which mostly contributed to the continuum emission. This multicomponent model fits the data adequately, and

was also employed to characterize the spectra of distinct regions extracted from the Chandra data. From our spectral analysis we find that the approximate fractional masses of shocked ejecta for the most abundant elements are: $M_{\rm O} \approx 32\%$, $M_{\rm Si/S} \approx 7\%/5\%$, $M_{\rm Ar+Ca} \approx 1\%$ and $M_{\rm Fe} \approx 55\%$. From the continuum component we derive a circumstellar density of $n_{\rm H} = 2.4 \pm 0.2$ cm^{-3}. This density, together with the measurements of the forward and reverse shock radii suggest an age of 0519-69.0 of 450 ± 200 yr, somewhat lower than, but consistent with the age estimate based on the extent of the light echo (600 ± 200 yr).

Finally, from the high resolution RGS spectra we measured a Doppler broadening of $\sigma = 1873 \pm 50$ km s^{-1}, from which we derive a forward shock velocity of $v_{FS} = 2770 \pm 500$ km s^{-1}. We discuss our results in the context of single degenerate explosion models, using semi-analytical and numerical modeling, and compare the characteristics of 0519-69.0 with those of other Type Ia supernova remnants.

4.1 Introduction

Thermonuclear (type Ia) supernova explosions have drawn a lot of attention over the last decade, as they provide a powerful tool to measure cosmological distances (Perlmutter et al. 1999; Riess et al. 1998). The reason is that they are bright enough to be observed over very large distances, and that, compared to core collapse supernovae, their peak luminosity shows relatively little variation, which can be further reduced by applying the empirical peak luminosity — decline rate correlation (Phillips et al. 1999). Nevertheless, some evolutionary systematic effects (Panagia 2005) may take place, which may affect the measured values of cosmological parameters. Thus, it is important to understand the mechanism and physics that governs thermonuclear explosions.

In addition to the extensive studies of the supernovae themselves, through their light curves (e.g Woosley et al. 2007; Blinnikov et al. 2006) and spectra (e.g. Branch et al. 2009), one can also turn the attention to the SN type Ia remnants. A typical young supernova remnant (SNR) is a bright X-ray source, due to the high temperatures of the plasma, heated by the forward and reverse shocks. The reverse shock, propagating inwards into the supernova ejecta, efficiently heats the metal-rich matter. The hot plasma produces X-ray spectra, abound with prominent emission lines. These spectra carry the imprints of the chemical composition of the plasma, and, therefore, the distribution of the elements in the supernova ejecta, which are determined by the explosion properties. Thus, a detailed analysis of the X-ray data of supernova type Ia remnants provides a powerful complementary tool in the studies of the nature of a thermonuclear supernova progenitor (e.g. Sorokina et al. 2004; Badenes et al. 2003).

The current generation of X-ray observatories, such as XMM-Newton and Chandra, provide the capability to obtain simultaneously spectral and imaging data

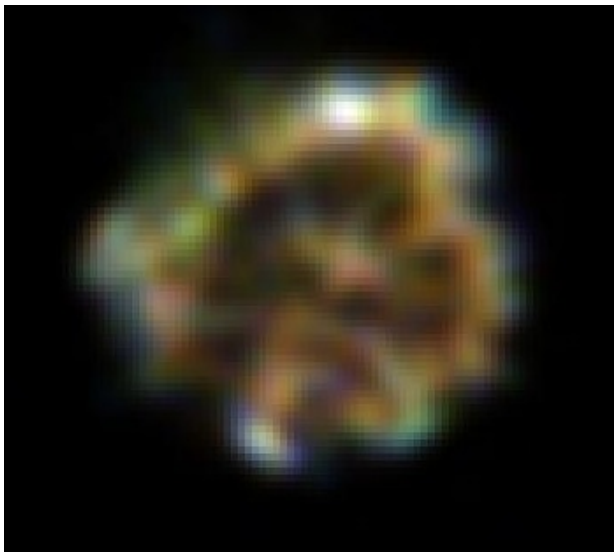

Fig. 4.1: Chandra smoothed RGB image of SNR 0519-69.0. Red — 0.5 - 1.0 keV, green — 1.0 - 2.0 keV, blue — 2.0 - 4.0 keV. North is up, east is left.

of extended objects such as SNRs. Young SNRs in the Large Magellanic Cloud (LMC) are especially suitable targets for these telescopes, as the relative proximity (48 kpc, e.g. Pietrzyński et al. 2009; Koerwer 2009) of the LMC yields a sufficiently high signal-to-noise level of the X-ray data as observed by the CCDs and grating spectrometers on board Chandra and XMM-Newton. The SNRs are still large enough (typically $\sim 1'$) to perform morphological studies with Chandra and small enough to be excellent targets for the Reflection Grating Spectrometer of XMM-Newton. An additional advantage is the relatively low interstellar absorption column towards LMC SNRs ($N_{\rm H} \approx 10^{21}$ cm^{-2}), as compared to most Galactic SNRs.

In this paper we present an X-ray study of the LMC SNR 0519-69.0. The SNR has an irregular patchy morphology and an angular extent in X-rays of 33", corresponding to a shell radius of 4 pc. A three color X-ray image of SNR 0519-69.0, based on the Chandra data, is presented in Fig. 4.1.

In the optical SNR 0519-69.0 has been investigated by Tuohy et al. (1982); Smith et al. (1991) and Ghavamian et al. (2007a). It is also one of several LMC SNRs for which a light-echo has been identified, from which an age of 600 ± 200 years can be deduced (Rest et al. 2005).

In X-rays the remnant was studied by Hughes et al. (1995), who analyzed the

ASCA spectra and found that the SNR is oxygen-poor and iron-rich and must be a remnant of a thermonuclear supernova (SN Ia) explosion. The analysis of Chandra data by Williams et al. (2001) revealed the separation between the shocked ejecta and the shocked circumstellar medium (CSM).

In the present study we analyzed archival X-ray data of SNR 0519-69.0 from the both XMM-Newton and Chandra observatories. We used the ACIS data of Chandra and the imaging spectroscopy (EPIC) and the high spectral resolution grating (RGS) data of XMM-Newton.

Various techniques to analyze the available data are employed. The high spatial resolution Chandra data provide us with an opportunity to study the composition of the SNR as a function of radius. The RGS data on the other hand, offer high resolution spectroscopy, but without much spatial information.

For the analysis of the SNR 0519-69.0 X-ray spectra, we employed the SPEX (Kaastra et al. 1996) spectral fitting software (version 2.01.05, November 16, 2009). The package contains the most up-to-date atomic data and has a wide range of plasma emission models, which is especially helpful and important in fitting complex spectra from objects such as SNRs.

We fit the XMM-Newton EPIC and RGS spectra with single and multicomponent NEI models. The high spectral resolution RGS data allow us to resolve details of the Fe-L line emission, and to measure line velocity broadening, due to the thermal and bulk motion of the shocked supernova ejecta.

This paper is organized as follows. First in Sect. 4.2, we describe briefly the Chandra and XMM-Newton data. The methods and techniques we used to deal with the spectral and imaging data are presented in Sect. 4.3. Sect. 4.4 contains the principal results of the study, which are discussed in Sect. 4.5. We conclude the paper in Sect. 4.6.

4.2 The data overview

4.2.1 Chandra

SNR 0519-69.0 was observed only with the ACIS instrument of Chandra X-ray Observatory (obs ID 118) for 41.1 ks on June 21, 2000. We analyzed the data with CIAO 4.1.1 software product and CalDB 4.1.2 calibration data. Apart from an X-ray spectrum of the whole SNR, we also used our own software to extract spectra from certain regions based on emission characteristics. The software reads the standard pipeline event lists and selects events from it based on a "mask" image, i.e. an image containing only zeroes and ones. An event is selected for spectral extraction, if its sky coordinates corresponds with a pixel of value one in the mask image. The event grade selection and spectral data binning scheme are identical to the standard CIAO software. The advantage of this method is that spectra can be extracted from regions with more complex shapes than with the region files, and

can be easily constructed based on hardness ratios or narrow band images. These spectra were used together with the ancillary and main response files generated for the SNR as a whole. Given that the remnant occupies only a small part of the ACIS-S3 CCD, using these files for the response is justified. For the background spectrum, we extracted a spectrum from an annulus with radii spanning from 19"to 37", centered on the SNR.

4.2.2 XMM-Newton

We used XMM-Newton observations of SNR 0519-69.0 (obs ID 0113000501) that were made on September 17, 2001, and have a total exposure of 47.8 ks.

For our study we concentrated on the EPIC MOS and RGS data. Although the EPIC MOS instruments (Turner et al. 2001) have a lower sensitivity than the EPIC pn instrument, they have a higher spectral resolution, which is important for line-rich sources, such as SNRs. The MOS1 observations were performed with thick (25.4 ks) and medium (15.6 ks) filters, whereas the MOS2 data were acquired with the medium filter only. For the spectral analysis the spectra, response and ancillary response files were combined, using weights proportional to the exposure times. For the background, spectra were extracted from an annulus with an inner radius of 2.1', and an outer radius of 4.3'. This is larger than for the Chandra background spectrum, because the XMM-Newton point spread functions have much broader scattering wings.

The RGS is a slitless spectrometer (den Herder 2001). For an extended source, this implies that the spectrum is smeared by the image of the source itself. For Small/Large Magellanic Cloud remnants, the smearing is modest, but present, and it gives rise to a change in the line spread function. For our analysis, we incorporated this effect into the response matrix by convolving the standard (point source) response matrix with the brightness profile of the SNR, as obtained from the Chandra observations. All the results presented here made use of these modified matrices. This procedure was also applied to the RGS data of the SN 1006 remnant (Vink et al. 2003) and SNR 0509-67.5 (Kosenko et al. 2008).

Apart from adapting the RGS response matrix, all reduction for both MOS and RGS data were made with the standard XMM-Newton software package SAS version 7.1.0.

4.3 Data analysis

4.3.1 Chandra radial emissivity profiles

The high spatial resolution Chandra data allow us to plot radial emissivity profiles of the remnant's shell, with a deprojection technique that was also employed by Helder & Vink (2008). For the measurements, we first made a radial surface

brightness profile of the remnant, using the centroid of the broadband emission (0.5-8.0 keV) as center. Then, assuming that the SNR is spherically symmetric, we used the Lucy-Richardson technique (Lucy 1974; Richardson 1972) to deproject the surface brightness profile into an emissivity profile (following the method of Willingale et al. 1996; Helder & Vink 2008). We applied this technique to images in different energy bands, where the emission lines from different species dominate. For the oxygen band, we choose 0.5-0.7 keV, for the added silicon and sulfur band, we took 1.75-3.00 keV. Because the spectra indicated that in the Fe-L band ($\sim 0.7 - 1.1$ keV) the relative contribitions from different Fe-L shell ions varies as a function of position (Sect. 4.3.5), we divided the iron energy band in a low (0.7-0.9 keV) and high (0.9-1.1 keV) energy band, which correspond roughly to line emission dominated by Fe XVII and Fe XX ions respectively.

For the broad band (0.5-8.0 keV) energy range, we calculated an inner and outer radius. The inner radius was determined where the emissivity (i.e. deprojected, ϵ) drops below one half of the maximum value. We ignored emissivities at radii less than 7", since the deprojection technique is not well constrained at these lower radii, due to the low contribution to the surface brightness Σ of shells at small radii ($\Sigma \propto \epsilon(R)R^2$). In general, there is no sharp rise in emissivity at the outer radius, so taking a value of one half of the maximum would underestimate the outer radius. Hence, we took a value of 1/20 of the peak value, which, in the deprojections, is just above the noise level of the background at large radii. In the remainder of this paper we assume that this measured inner radius of 2.7 ± 0.4 pc, corresponds to the location of the reverse shock and the outer radius to the forward shock at 4.0 ± 0.3 pc. We estimated the error from the standard deviation of this measurement repeated for 18 individual slices of 20° each.

We use the deprojected profiles to determine the shells in the remnant in which different species dominate (Fig. 4.2), which we will use in section 4.4 for estimating total masses of the shocked species. Table 4.1 lists the ranges in which the different components dominate. Silicon and sulfur dominate the emissivity in region 2/3, however, our numerical models (see Sect.(4.5) show that the Si/S and Ar/Ca layers coincide. For this reason, we split region 2/3 evenly in two parts. Furthermore, we chose 3.6 pc as the division between oxygen and the shocked CSM, since for this value, the volume of the shocked CSM is one fourth of the volume of the total remnant. The latter seems reasonable, if we assume a compression ratio of 4 over the shock front during the whole lifetime of the remnant. Note that all values mentioned above contain uncertainties. For the corresponding volumes, we estimate errors of 50%. In Fig. 4.2 we also show the observed radial profile and its deprojection for the 5-7 keV hard X-ray band. This band includes both continuum emission and Fe-K shell line emission around 6.5 keV. Unfortunately, the signal to noise ratio in this band is poor, but the profile suggests tentatively that the 5-7 keV emission is associated mostly with the Fe XX line emission in the 0.9-1.1 keV band. With some caution, it also suggests that there is no strong non-thermal X-ray

Table 4.1: The inner and outer radii for the SNR 0519-69.0 shell in different energy ranges.

Radii [pc]	0.5-8.0 keV	CSM 0	O 1	Si/S 2	Ar/Ca 3	Fe-high 4	Fe-low 5
$R_{\rm in}$	2.7 ± 0.4	3.6	3.48	3.405	3.33	3.15	2.7
$R_{\rm out}$	4.0 ± 0.3	4.0	3.6	3.48	3.405	3.33	3.15

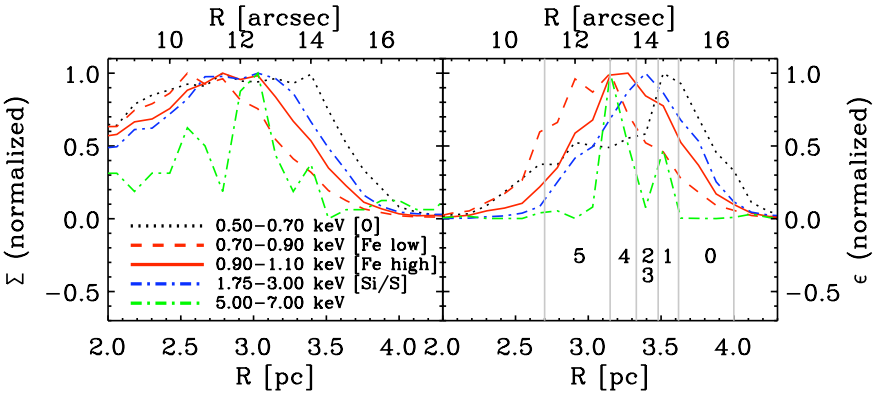

Fig. 4.2: Azimuthally averaged radial profiles in different energy bands. Left panel: surface brightness radial profiles. Right panel: deprojected emissivity profiles. The vertical light grey lines correspond to the spectral components, used in Sect. 4.3.4.

continuum associated with the forward shock.

4.3.2 EPIC and ACIS spectra

Fitting the XMM-Newton EPIC MOS and Chandra ACIS spectra with single-ionization timescale non-equillibrium ionization (NEI) SPEX model provides us with the typical values for the emission measure, electron temperature, ionization timescale and abundances in the remnant. The corresponding spectra and the best-fit model are shown in Fig. 4.3. The best-fit parameters of the spectral model are listed in Table 4.2. The best-fit abundances are plotted in Fig. 4.4. For comparison, also the abundances, derived from the analysis of the younger supernova Type Ia remnant 0509-67.5 (Kosenko et al. 2008) are plotted.

A single ionization timescale NEI model is not the best approach to explain

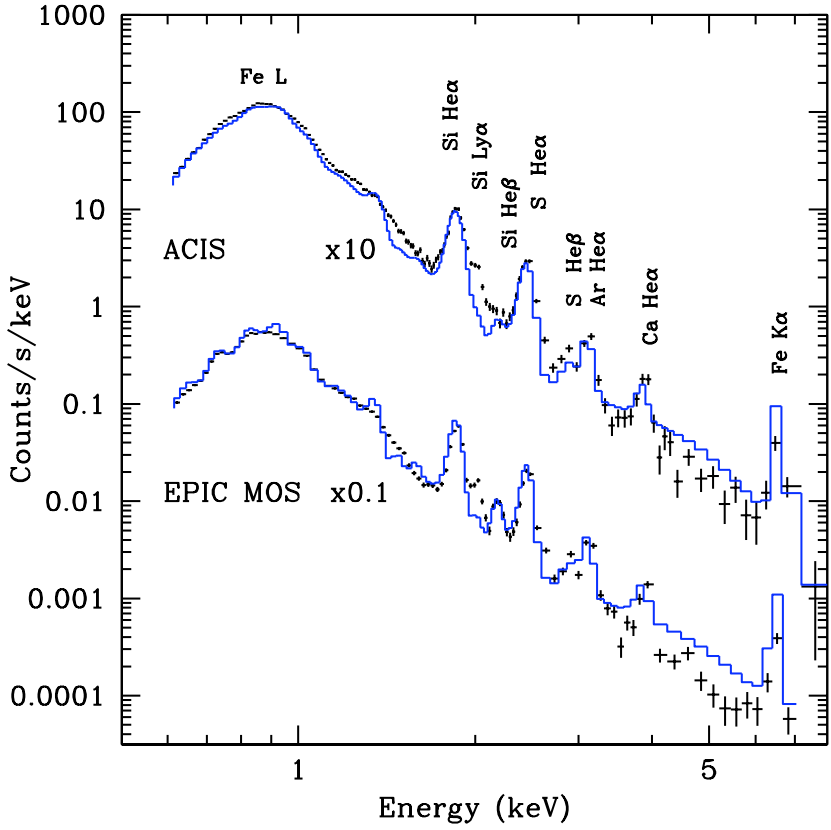

Fig. 4.3: Combined fitting of the EPIC MOS (scaled down by a factor of 10) and ACIS (scaled up by a factor of 10) data with single ionization timescale NEI model of SPEX.

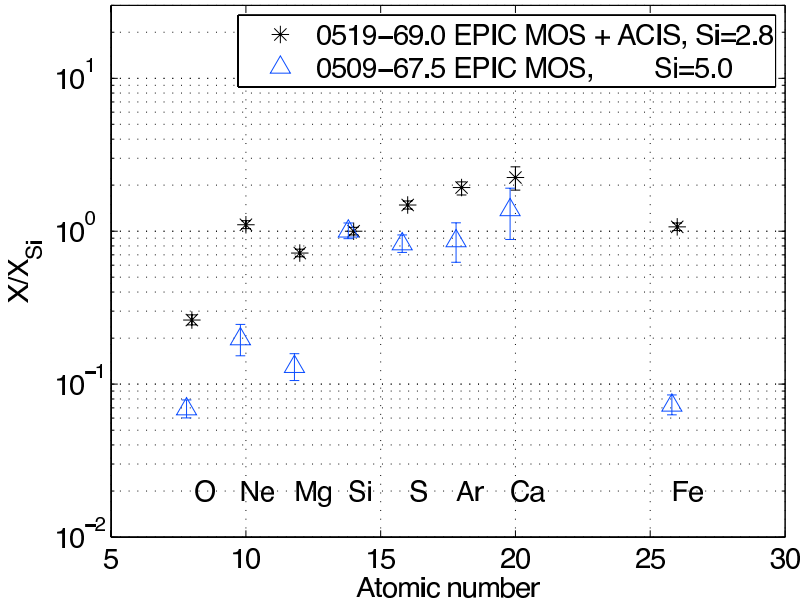

Fig. 4.4: Best-fit abundances of SNR 0519-69.0 and SNR 0509-67.5 (Kosenko et al. 2008), derived from single-ionization timescale NEI models. The data are in solar units (Anders & Grevesse 1989), normalized by Si abundances.

emission from such a complicated and layered object as a SNR, because in the shell one expects ionization timescale and abundance gradients. For example, Fig. 4.3 clearly shows that Si Lyα line is missing in the model and Fe K line flux is overestimated. This discrepancy leads to a very high value of the fit statistic; $\chi^2/d.o.f. \simeq 30$.

Apart from the MOS, we fitted also the EPIC pn data with an NEI model, that yields approximately the same values of the basic parameters of the spectrum.

4.3.3 XMM-Newton RGS spectra

The RGS spectra of SNR 0519-69.0 were also fitted with SPEX NEI models. The fit range was limited to the 0.5-1.1 keV range, which has the more prominent line emission. The best-fit parameters of the single NEI model are listed in Table 4.2 (first column). This single-ionization timescale model was not able to reproduce the fluxes of O VII and Fe XXI ions: the modeled lines are weaker than the data

Table 4.2: The best-fit NEI parameters of the XMM-Newton EPIC, RGS and Chandra ACIS data for the entire remnant (columns 1 and 2), column 3 lists data for the inner shell of the SNR and column 4 — for the outer shell (see Fig. 4.7).

Parameter	RGS	EPIC MOS + ACIS	ACIS inner	ACIS outer
$n_e n_H\, V$ (10^{58}, cm^{-3})	$1.8^{+2.5}_{-1.8}$	$3.7^{+0.2}_{-0.2}$	$2.63^{+0.33}_{-0.32}$	$0.66^{+6.49}_{-0.08}$
kT_e (keV)	$2.21^{+0.08}_{-0.07}$	$2.82^{+0.03}_{-0.03}$	$2.88^{+0.06}_{-0.06}$	$1.73^{+0.14}_{-1.07}$
$n_e t$ (10^{10}, s cm^{-3})	$2.69^{+0.03}_{-0.03}$	$2.27^{+0.01}_{-0.01}$	$2.22^{+0.02}_{-0.002}$	$3.90 \pm N/A$
n_H (10^{21}, cm^{-2})	—	$2.62^{+0.07}_{-0.06}$	$2.74^{+0.11}_{-0.11}$	—
$\chi^2/d.o.f.$	2.4	29.4	10.4	2.5

Table 4.3: The best-fit parameters of the RGS spectral fitting with the three-component NEI model. $\chi^2/\mathrm{d.o.f.} = 1.8$

Parameter	O	Fe-low	Fe-high
$n_e n_H\, V$ (10^{58}, cm^{-3})	$0.50^{+0.08}_{-0.06}$	$5.6^{+0.2}_{-0.3}$	$4.8^{+1.2}_{-0.7}$
kT_e (keV)	$0.84^{+0.27}_{-0.18}$	$1.22^{+0.05}_{-0.33}$	$2.51^{+6.54}_{-0.99}$
$n_e t$ (10^{10}, s cm^{-3})	$2.3^{+0.8}_{-0.5}$	$3.0^{+2.3}_{-0.2}$	$5.2^{+3.4}_{-1.4}$
σ_{RGS}(km s^{-1})		1873 ± 50	

indicate (top panel of Fig. 4.5). For this reason, and inspired by the spatial layering, as indicated by the Chandra data (Sect. 4.3.1), we fitted the RGS spectra in the range of 0.5-1.1 keV with a three-component NEI model: one component is for pure oxygen, the second — for the low-ionized iron (Fe XVII – Fe XVIII), and the third — for the high-ionized iron (Fe XIX – Fe XXI). The corresponding spectra are shown in the bottom panel of Fig. 4.5. The corresponding best-fit parameters are listed in the Table 4.3. As can be seen in Fig. 4.5, this model gives a much better fit to the data than the single NEI model. Note, that no Ne emission is needed to obtain a good fit (Ne IX has a prominent line at 0.92 keV and Ne X at 1.02 keV).

An important advantage of the high spectral resolution RGS spectra is that it enables us to measure the line broadening. The measured best-fit value of the line velocity broadening is $\sigma_v = 1680 \pm 50$ km s^{-1} for the single NEI model and $\sigma_v = 1873 \pm 50$ km s^{-1} for the multi-component model. We adopt the last value as the most reliable value for the Doppler broadening, since the model fits the data much better (Fig. 4.5).

4.3.4 EPIC MOS and RGS spectra combined, multicomponent approach

A next step in our study was to combine both the EPIC MOS and RGS data and try to model it with a multi-component NEI model, in which each component roughly corresponds to the layering observed in the radial profiles (Sect. 4.3.1). In addition to the three components used for fitting the RGS spectra (Sect. 4.3.3), we added three additional components, which contribute mostly to the emission outside the RGS spectral range. In total this amounts to six components: oxygen (O, or component 1), silicon/sulfur (Si/S, or component 2), argon and calcium (Ar/Ca, or component 3) high ionized iron (Fe-high, or component 4), low ionized iron (Fe-low, or component 5), and a continuum dominated model (component 0) for which we used an NEI model with the abundances fixed to those of the LMC

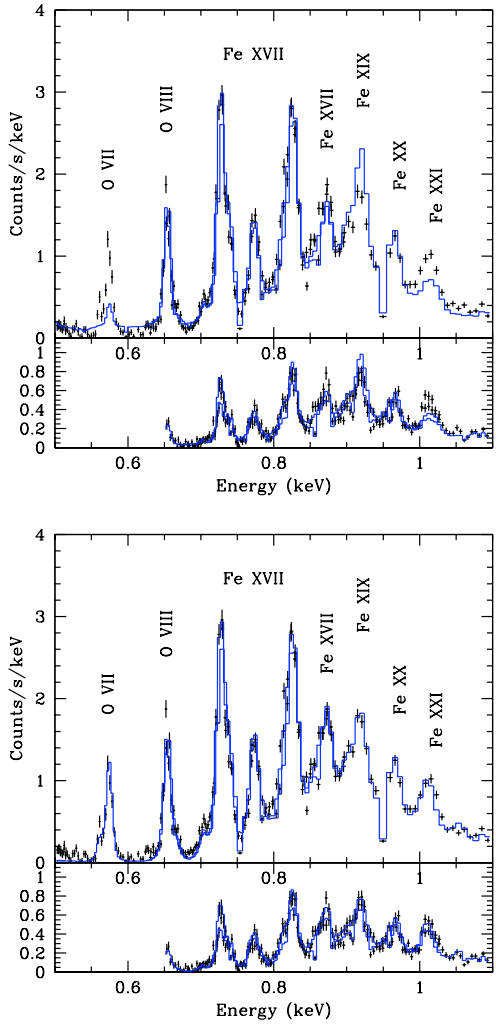

Fig. 4.5: Top panel: the four RGS spectra RGS1, RGS2 of SNR 0519-69.0. Shown are both first order (upper frame) and second order (lower frame) spectra and best fit single NEI model including a line velocity broadening model. Bottom panel: The same as the top panel, but here the spectral model consists of a three-component NEI model. Black crosses are the data, solid lines are the models.

(Russell & Dopita 1992). In addition the model included an interstellar absorption component.

The corresponding principal abundance parameters in components 1–5 were set to 10^7 times the solar value for the specific elements considered, whereas the abundances of other elements were set to zero. Thereby we secure that the absolute abundances of the corresponding elements are at least two orders of magnitude higher than those of the hydrogen, i.e. for all practical purposes these components correspond to pure metal plasma's. The corresponding spectra and the best-fit multicomponent model are presented in Fig. 4.6. The best-fit parameters (emission measure, electron temperature, ionization timescale) are listed in Table 4.4. The best-fit value for the hydrogen column density is $1.7^{0.3}_{-0.1} \times 10^{21}\ \mathrm{cm}^{-2}$.

The multi-component NEI model gives an adequate fit to the data. In contrast to the three NEI component model used to fit only the RGS data, some of the oxygen line emission in this multi-component model attributes part of the corresponding line emission to the shocked CSM component, in particular the O VIII line emission. One peculiarity of the multi-component model is the high $n_{\mathrm{e}}t$ value for Ar/Ca. This is not an artefact of the model chosen. Isolating that part of the spectrum that is dominated by Ar/Ca line emission and searching for other combinations of kT_{e} and $n_{\mathrm{e}}t$ resulted in similar best fit values. In general, $n_{\mathrm{e}}t$ correlates inversely with kT_{e}. This means that if the $n_{\mathrm{e}}t$ of the plasma is in reality lower than our best fit value, an unrealistically high electron temperature is required.

4.3.5 Spatially resolved spectroscopy

Inner and outer rings of the remnant

In the analysis of the Chandra data we extracted ACIS spectra from two shells: the outer one which is presumably the shocked CSM of the remnant and the inner one which is the region where the emission is produced by the shocked ejecta material. These regions are outlined with green circles in Fig. 4.7. Each of the spectra was analyzed in the usual way and fitted with single NEI models. The corresponding best-fit parameters are listed in Table 4.2.

ACIS oxygen and iron masks

The low energy band (0.5-1.1 keV) of the ACIS spectra was treated more thoroughly. We extracted three images of the remnant in the energy bands (see the RGS spectra with the corresponding emission lines) of $0.5 - 0.7$ keV (O only), $0.7 - 0.9$ keV (Fe-low) and $0.9 - 1.1$ keV (Fe-high). Next, three spatial masks were created on the basis of these images, in order to locate regions with the relative emission peaking in either of these energy bands. The masks are presented in the Fig. 4.7. They were applied to the ACIS image of the remnant. Finally, we extracted spectra using these, non-overlapping, image masks.

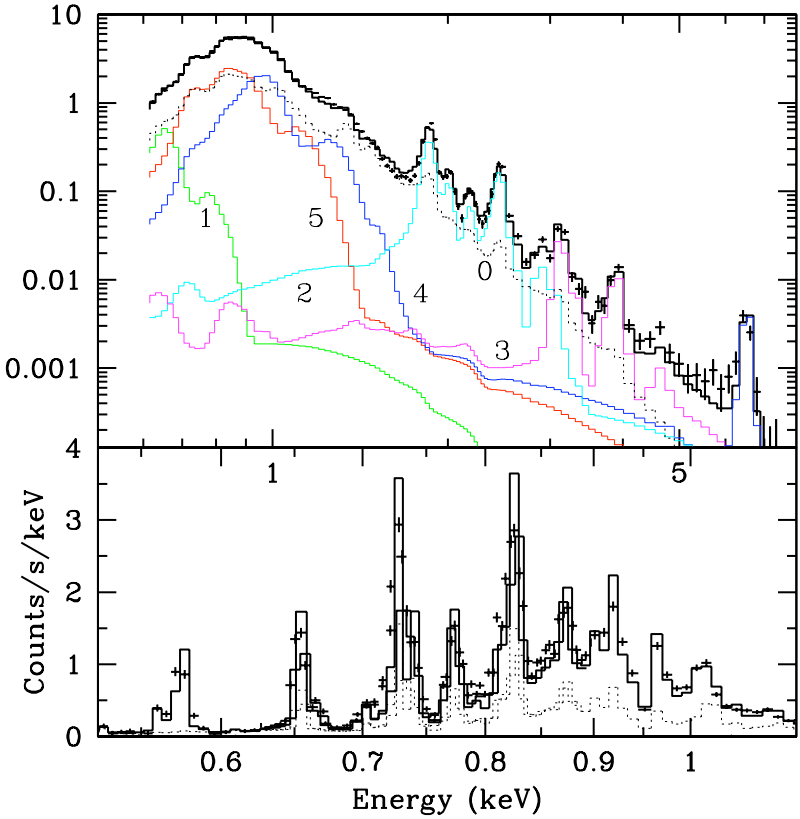

Fig. 4.6: The EPIC MOS1 and MOS2 combined (upper frame) and the RGS1 and RGS2 first order (lower frame) spectra with the best-fit model of the six NEI components and interstellar absorption. Black crosses are the data, the solid lines show the model. The contributions from the different components are marked with the numbers listed in Table 4.4. The dotted lines correspond to the CSM component (0).

Table 4.4: Parameters of the components in the multi NEI approach. Errors are 1σ rms, $\Delta\chi^2 = 2$, $\chi^2/d.o.f = 7.8$. Emission measure $EM_X = n_e n_X V$.

Component number	1	2			3	4	5	0
Layer	O	Si	S	Ar	Ca	Fe-high	Fe-low	CSM
EM_X (10^{54} cm^{-3})	$8.87^{+3.39}_{-0.45}$	$2.47^{+0.31}_{-0.14}$	$1.56^{+0.20}_{-0.09}$	$0.78^{+0.63}_{-0.38}$	$0.60^{+0.49}_{-0.29}$	$2.52^{+0.32}_{-0.35}$	$2.15^{+0.17}_{-0.36}$	$2.36^{+0.50}_{-0.11} \times 10^5$
kT_e (keV)	$0.72^{+0.70}_{-0.24}$	$7.00^{+3.00}_{-2.26}$	$7.00^{+3.00}_{-2.26}$	$2.67^{+10.00}_{-1.17}$	$2.67^{+10.00}_{-1.17}$	$2.73^{+0.07}_{-0.27}$	$1.26^{+0.44}_{-0.26}$	$0.64^{+0.02}_{-0.06}$
$n_e t$ (10^{10} s cm^{-3})	$1.52^{+3.66}_{-0.92}$	$3.63^{+0.27}_{-0.18}$	$3.63^{+0.27}_{-0.18}$	$27.2^{+N/A}_{-18.8}$	$27.2^{+N/A}_{-18.8}$	$3.78^{+0.34}_{-0.26}$	$2.55^{+0.56}_{-0.39}$	$80.0^{N/A}_{-13.4}$
n_e/n_X	6.6	21.2	33.7	30.5	39.6	19.6	17.5	1.2

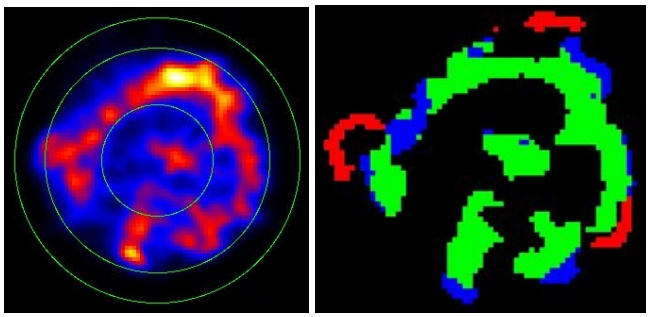

Fig. 4.7: Left panel: Chandra image of SNR 0519-69.0. Outer and inner regions that were considered are outlined with green lines. Right panel: the masks of the Chandra image of SNR 0519-69.0: red — oxygen ($0.5 - 0.7$ keV), green — Fe-low ($0.7 - 0.9$ keV), blue — Fe-high ($0.9 - 1.1$ keV)

The resulting spectra are poorly fitted with single-ionization timescale NEI models, the values of the best-fit abundances contain large errors, and physical parameters, such as temperature and ionization timescale are of the order of the typical values obtained in the analysis of the EPIC and ACIS data of the entire remnant. This suggests that the masks did not totally separate out specific layers, but rather that certain layers may dominate the emission in certain regions, with some overlap from other layers. Therefore, we applied the six-component NEI model with the parameters obtained in the fitting of EPIC and RGS data to each of the masked spectra. We fit only emission measures (i.e. normalizations) of each component in order to evaluate the contributions of the different components, each corresponding to certain elements, to the spectra of these three distinct regions. The spectra and the best-fit models are presented in Fig. 4.8.

The contributions of each component to the different spectra are presented in the Fig. 4.9, in which we plot the emission measures of each NEI component.

4.4 Results

The fitting of the XMM-Newton EPIC MOS and Chandra ACIS spectra with SPEX NEI models allowed us to measure (Table 4.2) the parameters of the plasma, such as typical electron temperature $kT_e \simeq 3$ keV, ionization timescale $n_e t = 2.3 \times 10^{10}$ $\mathrm{s/cm^3}$ and abundances (plotted on Fig. 4.4) in the remnant. The derived best-fit abundances are similar to those of SNR 0509-67.5 (Kosenko et al. 2008), but overall the 0519-69.0 remnant is more metal-rich (S, Ar, Ca and in particular Fe) as it is older and more of the supernova ejecta matter has been swept up by the

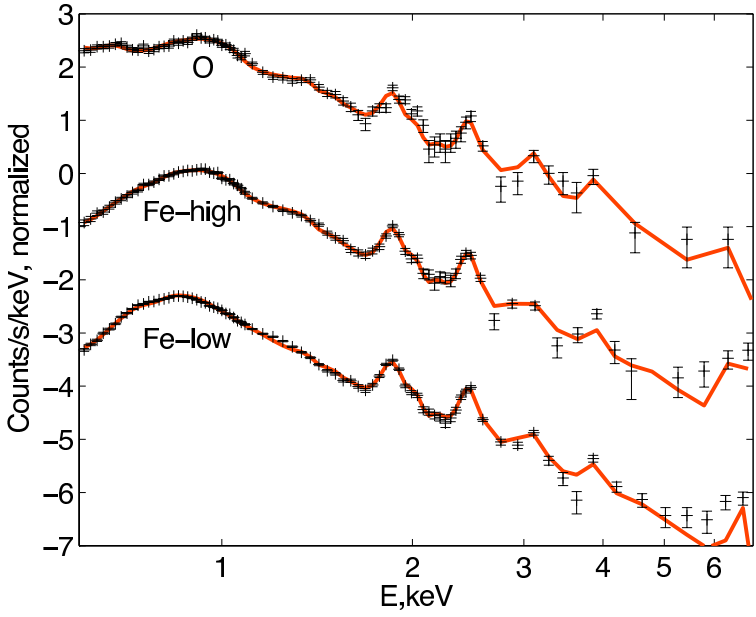

Fig. 4.8: The three masked ACIS spectra. From top to bottom: oxygen (data shifted upwards for three orders), Fe-high, Fe-low (data shifted downwards for three orders).

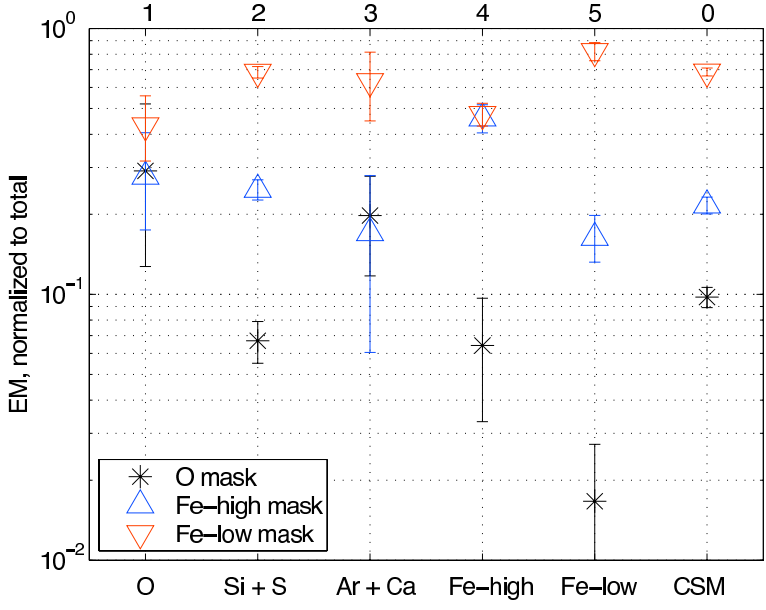

Fig. 4.9: The emission measure of each of the six NEI components shows the contribution of different elements to the emission of the masked regions of the Chandra data.

reverse shock. The relative amount of the light elements (such as O, Ne, Mg) is comparable for both SNRs.

4.4.1 The circumstellar matter density

The multicomponent NEI model provides us with the parameters of the CSM component (component 0 in Table 4.4). Using the best-fit emission measure value we can make an estimate of the density of the CSM in the vicinity of the remnant.

$$n_{\rm CSM} = \frac{1}{2}\sqrt{\frac{EM_{\rm LMC}}{V_{\rm SNR}\, n_e/n_{\rm H}}} = 2.4 \pm 0.2 \ {\rm cm}^{-3} \tag{4.1}$$

where $EM_{\rm LMC} = 2.36^{+0.50}_{-0.11} \times 10^{59}$ cm^3 and $n_e/n_{\rm H} = 1.2$ are taken from Table 4.4. We assumed, that the volume of the shocked CSM is $1/4\, V_{\rm SNR}$, with $V_{\rm SNR} = 4\pi/3\, R^3_{\rm out} = 8.0 \times 10^{57}\,{\rm cm}^3$ and $R_{\rm out} = 4.0$ pc (Table 4.1).

4.4.2 Structure of the ejecta

The radial emissivity profiles of the SNR in different energy bands, drawn from the Chandra observations, clearly show stratification of the elements in the remnant. Fig. 4.2 shows that the outermost layer is oxygen rich, the next inward layer produces most of the Si and S emission, all the iron emission comes from the innermost layers of the shell. The iron shell is split in two regions with different ionization properties. The outer layer of high ionized (Fe XX) and the inner one of low ionized (Fe XVII) iron reflect the effects of time-dependent ionization processes in the shocked ejecta: the inner layer has been shocked later by the reverse shock, and therefore has the lowest $n_e t$.

This stratification is also confirmed by the analysis of the masked Chandra images (Fig. 4.7 right panel) and their spectra (Fig. 4.8). Fig. 4.9 shows the contribution of different elements to the emission from the masked images.

4.4.3 The chemical composition

The measurements of the inner and outer radii of the shell in different energy bands (Table 4.1) allow us to estimate the masses of the layers, which have been swept up by the reverse shock. Using the best-fit emission measure value $EM_{\rm X} = n_{\rm e} n_{\rm X} V_{\rm X}$ of the each model of the multicomponent fitting (Table 4.4), we can express the mass $M_{\rm X}$ of an element "X" (i.e. O, Si, S, Ar, Ca, Fe) as

$$M_{\rm X} = n_{\rm X} V_X m_{\rm X} = \sqrt{\frac{EM_{\rm X} V_{\rm X}}{n_{\rm e}/n_{\rm X}}}\, m_{\rm U} A_{\rm X} \tag{4.2}$$

where $n_{\rm e}/n_{\rm X}$ — electron to ion densities ratio, $m_{\rm U}$ — atomic mass unit, $A_{\rm X}$ — atomic mass of the element, $V_{\rm X}$ — volume occupied by the element (derived from the radii of Table 4.1).

Combining the available data we obtain $M_{\rm O} = 0.36\,M_{\odot}$, $M_{\rm Si/S} = 0.14/0.10\,M_{\odot}$, $M_{\rm Ar/Ca} = 0.08/0.07\,M_{\odot}$, $M_{\rm Fe} = 1.05\,M_{\odot}$, $M_{\rm tot} = 1.8\,M_{\odot}$. Note, that the mass values for the elements are affected by the $\sim 50\%$ errors of the volume estimates, although the total mass is less affected. These masses are higher than may be expected for a single degenerate Type Ia SN model, for which the total mass should be $M_{\rm tot} = 1.4\,M_{\odot}$. The most likely reason for this discrepancy may be the errors in the volume estimates or in the filling factor. In particular, inhomogeneities such as knots may give emission measures skewed toward the higher density regions. In fact, the supernova material may be porous and clumpy, thus the emitting volume should be scaled down using a filling factor (e.g. see 3D simulations of thermonuclear explosions by Röpke & Bruckschen 2008). For example, if we assume volume filling factor in the supernova of ~ 0.4, then we get more adequate values $M_{\rm O} = 0.23\,M_{\odot}$, $M_{\rm Si/S} = 0.09/0.07\,M_{\odot}$, $M_{\rm Ar/Ca} = 0.05/0.05\,M_{\odot}$, $M_{\rm Fe} = 0.67\,M_{\odot}$, $M_{\rm tot} = 1.15\,M_{\odot}$.

The multicomponent fitting of the XMM-Newton EPIC and RGS spectra reveals a specific behavior of the different NEI components. Table 4.4 shows that emission measure ($EM_{\rm X} = n_e n_X V_X$) of each component drops from oxygen to calcium, while the values of the ionization timescale parameter $n_e t$ rise from O to Ca. This trend indicates that increasing from the lighter to the heavier elements, the electron density overcomes the factor of time, which probably does not change drastically for the shocked intermediate mass elements (from Si to Ca). Thus, qualitatively, the decrease of the emission measure and increase of the ionization timescale reflect the relative abundances of the species from O to Ca, i.e. the quantity $n_e n_X V_X/(n_e t) = n_X V_X/t \propto M_X$ (total shocked mass of an element X) is lower for the heavier species. A similar behavior of the ionization timescale parameter for different species was established by Lewis et al. (2003) in their analysis of the Chandra data of SNR N103B.

From these considerations, applying the time of $t \simeq 500$ years to all components, we can make rough estimates of the relative contributions of the species in the SNR 0519-69.0 ejecta to be as follows: $M_{\rm O} = 32\%$, $M_{\rm Si/S} = 7\%/5\%, M_{\rm Ar+Ca} = 1\%$, $M_{\rm Fe} = 55\%$ of the total shocked mass, which are roughly consistent with the mass ratios derived above, using volume estimates. The relative amount of Ar and Ca is probably underestimated, due to the high value of ionization timescale parameter measured in the component 3, for which we do not have a good explanation (note the corresponding errors bars in Table 4.4).

4.5 Discussion

4.5.1 Stratification and composition of the ejecta

Using the Chandra images we built azimuthally averaged radial emissivity profiles of the SNR in different energy bands, which clearly demonstrate the layering of the elements in the supernova (Fig. 4.2). Also these profiles reveal the effects of time-dependent ionization, as the emission from low ionized iron originates mostly from the inner layers of the iron shell, which is distinct from the high ionized "older" outer iron layers.

These effects are also visible in the Chandra spectra extracted using the masked images (Fig. 4.7). However, apparently projection effects play a role in that the spectra of the more inward lying layers are contaminated by the outer layers. For example, the spectral fitting with multi-component NEI models shows (Fig. 4.9) that the oxygen-rich component (component 1) is equally abundant in all three (O, Fe-high, Fe-low) masks. Si and S (component 2) is almost absent in the O-mask, as it is inside the oxygen-rich layer, but it does contribute to the spectra of inner layers of the Fe-low mask. Ar and Ca (component 3) tend to be in the outer layers, but the parameters of this component cannot be reliably measured, and have considerable errors. The O-mask spectrum hardly contains any contribution from the iron-rich components (4,5), as this outer layer can be isolated without much projection effects.

Fe-K emission is present in both the regions corresponding to the Fe-low and Fe-high masks. This is probably due to projection effects, since our spectral analysis suggests that the Fe-K emission is mostly coming from the high ionization layer, which was shocked earlier (component 4, Table 4.4). The radial emission profiles are consistent with this association, but we note that the signal to noise of the 5-7 keV image on which this is based is low. The high temperature of this high ionization layer may be surprising, but it should be mentioned that the electron temperature depends on both the shock velocity, and the degree of equilibration between electron and ion temperature. In general, one expects that ejecta that is shocked later by the reverse shock is heated to higher temperatures, but this may be off set by the shorter time available for the electrons to equilibrate with the ions. The situation in 0519-69.0 may somewhat resemble the situation in the south of Kepler's SNR. The analysis of Cassam-Chenaï et al. (2004) shows that for this region Fe-K peaks at a larger radius than the Fe-L emitting region.

4.5.2 Comparison of the stratification with other Type Ia supernova remnants

The chemical stratification of SNR 0519-69.0 is striking. Even more so if one considers that this SNR is much more distant than the well studied Galactic Type Ia SNRs Tycho (SN 1572), Kepler (SN 1604) and SN 1006. All these SNRs also

show some stratification, but less pronounced. In some cases the Fe, Si, and O layers seem to be very close together or even indistinguisable as separate layers. The latter is especially true for Tycho, in which silicon and iron are found very close to the shock front (Warren et al. 2005; Badenes et al. 2006). For Kepler the situation is different for the northern part of the SNR than for the southern part (Cassam-Chenaï et al. 2004). In the north the spatial separation between Si and Fe is small, whereas in the south the situation is in fact similar to the stratification of SNR 0519-69.0.

The situation for SN 1006 is a bit more complicated. There the O-rich ejecta lie very close to the forward shock (Cassam-Chenaï et al. 2008), but otherwise the Fe-rich layer seems to lie at smaller radius, and may not even have been shocked by the reverse shock, since UV absorption spectra shows the reverse shock to go through Si-rich material (Hamilton et al. 2007).

So what is the origin of this variation in stratification among Type Ia SNRs? It could be that there is some variation among Type Ia supernovae itself, with some supernovae producing more mixing than others. Optical spectroscopy of Type Ia supernovae suggests a strong radial stratification (e.g. Branch et al. 2005; Mazzali et al. 2007) with the the outer ejecta consisting of low mass elements (O, Mg), then followed by intermediate mass elements (IME), and the inner ejecta consisting of Fe and Ni isotopes. However, a group called High Velocity Gradient (HVG) supernovae (Benetti et al. 2005) show a strong gradient in the Si II velocities as a function of time, and evidence for high velocity IME. For the HVG SN 2002bo Si appears to be mixed in with O (Stehle et al. 2005). The strong stratification observed in SNR 0519-69.0 suggests, therefore, that its supernova did not belong to the HVG class.

This does not mean, however, that Kepler or Tycho did belong to the HVG class, because other mechanisms may have destroyed the strong layering in the SNR phase. Kepler is in that sense a very interesting case, as the northern and southern regions show different behaviors. In the north the blast wave of Kepler appears to be interacting with a pre-existing shell of about 1 $M_{\odot}$, which caused a strong deceleration of the blast wave (Vink 2008c). The lack of stratification in that region may therefore be attributed to the strong deceleration, squeezing the different layers closer together.

Interestingly, the expansion rate of Tycho in the eastern part, where the ejecta are very close to the shock front, is also much lower than expected for a SNR expanding in a homogeneous medium (Katsuda et al. 2010). It is, therefore, possible that also in Tycho the initial stratification is no longer visible, as the layers have been squeezed together due to the presence of a strong density gradient, and perhaps even mixed due hydrodynamical instabilities.

Another explanation for the proximity of the ejecta to the shock front in Tycho is the effect of efficient cosmic ray acceleration (Warren et al. 2005). The efficient acceleration alters the equation of state due to the large pressure fraction attributed

to relativistic particles and energy losses due to escape of the highest energy cosmic rays (Decourchelle et al. 2000; Helder et al. 2009). The distance between contact discontinuity and shock front is smaller in the east, whereas the X-ray synchrotron rims, a signature of cosmic ray acceleration, are more pronounced in the west. Moreover, one should not confuse the distance *between* contact discontinuity and shock front, with a lack of stratification *within* the ejecta. Only if the equation of state within the ejecta is changed, can one explain the lack of stratification by invoking cosmic rays. This could be the case, if also the reverse shock is efficiently accelerating particles. For Tycho there is no evidence that this is the case, but the reverse shock of the core collapse SNR Cas A has been proposed as a site of efficient cosmic ray acceleration (Helder & Vink 2008).

In addition to cosmic ray acceleration it has been proposed that Rayleigh-Taylor instabilities have brought ejecta close to the shock front (Chevalier et al. 1992; Wang & Chevalier 2001; Badenes et al. 2006). If this is indeed the case, it may also have destroyed the initial stratification of the ejecta. It is, however, not clear why this mechanism would have affected the stratification of Tycho but not of SNR 0519-69.0, or the southern part of Kepler. So perhaps it is a combination of factors that made Tycho and the north of Kepler less stratified, than 0519-69.0 and the south of Kepler.

4.5.3 The chemical composition of SNR 0519-69.0

From our spectral analysis we derive ejecta masses for O, Si/S, Ar/Ca, and Fe. These masses should be regarded with some caution, because inhomogeneities in the density distribution can lead to some systematic errors. However, on face value, our estimates indicate that the overall abundance pattern matches that for normal Type Ia supernovae, but that the oxygen mass is rather large, $M_{\rm O} \approx 0.2 - 0.3$ M$_\odot$.

According to a recent analysis of optical spectra of Type Ia supernovae (Mazzali et al. 2007) the amount of material from the C/O white dwarf burned into IME and more massive elements is remarkably homogeneous, corresponding to a total mass of roughly $M_{\rm IME,Fe,Ni} \approx 1.1$ M$_\odot$. This means that about 0.2-0.3 M$_\odot$ consists of lower mass elements. This is consistent with the amount we infer for SNR 0519-69.0, provided that most of the outer layers consist of oxygen and that little unburned carbon is present.

One of the differences between pure deflagration and delayed detonation explosion models is that the latter can burn material all the way to the outer edge of the white dwarf, leaving no carbon. Optical spectroscopy of Type Ia supernovae reveal that little or no carbon is present, with the oxygen abundance a factor 100 to 1000 times the carbon abundance (Marion et al. 2006). The relatively high mass of oxygen in 0519-69.0 is therefore consistent with optical spectroscopy of Type Ia supernovae, and supports the idea that burning in the outer layers converts almost all carbon to oxygen.

The amount of Fe that we infer, ~ 0.7 M$_\odot$, is also fairly typical for Type Ia

supernovae. Here we need to caution that not all the Fe may have been shock heated by the reverse shock, so the total iron mass may be higher. Mazzali et al. (2007) showed that the peak luminosity, for which they use the drop in magnitude within 15 days after maximum (Δm_{15}) as a proxy, correlates with the total amount of iron/nickel synthesized (see also Woosley et al. 2007). Using their "Zorro diagram" we can translate our estimate of shocked iron (which includes decayed ^{56}Ni), in an estimate for Δm_{15}. $M_{\rm Fe} > 0.7$ M$_\odot$ corresponds to $\Delta m_{15} \lesssim 1.4$. Combining the amount of IME that we estimate $M_{\rm IME} = 0.2 - 0.4$ M$_\odot$ with the "Zorro-diagram" suggests that $\Delta m_{15} \gtrsim 1.1$.

These constraints suggest that the supernova was a fairly normal Type Ia event, not as bright as SN1991T ($\Delta m_{15} = 0.95$), but similar to for example the template Type Ia SN 1996X ($\Delta m_{15} = 1.3$, Salvo et al. 2001). This is unlike the youngest known Type Ia SNR in the LMC, 0509-67.5, which was according to the light echo spectrum of the supernova an exceptionally bright Type Ia (Rest et al. 2008), similar to SN 1991T.

There is some evidence that bright Type Ia supernovae are associated with younger stellar populations (Gallagher et al. 2008), but the starforming history around SNR 0509-67.5 is not significantly more recent than around SNR 0519-69.0 (Badenes et al. 2009). This study, therefore, does not provide evidence for a one to one relation between population age and supernova brightness. In addition, Howell et al. (2009) show that the relation between the mean galaxy stellar population age and Type Ia brightness has significant scatter. This may be no suprise, if the brightness of a Type Ia supernova is related to the properties and history of the progenitor white dwarf, whereas the time delay between birth of the binary system and the supernova event is also governed by the evolution of the secondary star (Howell et al. 2009).[1]

4.5.4 Analytical model

From the measured locations of the reverse and forward shocks, we can derive typical velocities of the plasma, using the Truelove & McKee (1999) analytical models, with the ejecta density power $n = 7$. Setting the density of the circumstellar matter to $n_{\rm CSM} = 2$ cm^{-3}, supernova explosion energy to $E = 10^{51}$ erg, and the mass of the progenitor to $M_{\rm WD} = 1.4\,M_\odot$, we can plot the forward to reverse shock radii ratio versus the time that passed since the explosion. We see from the left panel of the Fig. 4.10 that these parameters correspond to age of the remnant of 460 ± 150 years, which is somewhat lower than the value estimated by Rest et al. (2005). The leftmost bottom panel of Fig. 4.10 shows that in this model, the ratio of the reverse to forward shock velocity is $v_{RS}/v_{BW} \simeq 1.2$.

[1] Nevertheless, some correlation between time delay and white dwarf properties can be expected, since a long time scale for the evolution of the primary star (the white dwarf that will explode), automatically means that the secondary star evolves on an even longer time scale.

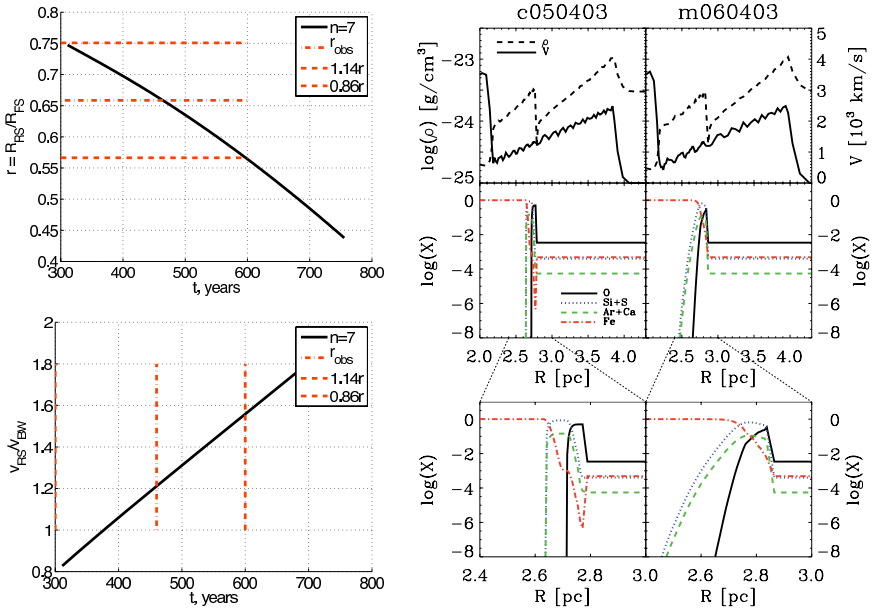

Fig. 4.10: Left two plots: Truelove & McKee (1999) analytical solution for SNR 0519-69.0. Radii ratio vs. the age (top panel); red dash-dotted lines show the measured value from the Chandra measurements (Sect. 4.3.1). Reverse shock velocity (in the frame of the ejecta) to forward shock velocity ratio vs. the age (bottom panel); red dash-dotted lines show values of age derived from the top plot. **Right four plots:** density, velocity (top panels) and abundances (bottom panels) profiles of the numerical models. In this set, left plots show the "mildly mixed" c050403 model, right plots — "moderately mixed" m060403.

4.5.5 Numerical HD models

We run several hydrodynamical models (Sorokina et al. 2004; Kosenko 2006), in order to reproduce the observed features of SNR 0519-69.0. We set the CSM density to $\rho_{\rm CSM} = 3 \times 10^{-24}$ g cm^{-3}. We considered two "toy" explosion models by Woosley et al. (2007) of thermonuclear supernovae: a "mildly mixed" c050403 ($M_{\rm Ni} = 0.5 M_{\odot},\ M_{\rm Fe} = 0.4 M_{\odot},\ M_{\rm IME} = 0.3 M_{\odot}$) and a "moderately mixed" m060403 ($M_{\rm Ni} = 0.6 M_{\odot},\ M_{\rm Fe} = 0.4 M_{\odot},\ M_{\rm IME} = 0.3 M_{\odot}$). The distribution of the elements in these models is plotted in the right lower panels of Fig. 4.10. Velocity and density profiles of the models at the age of 560 years, which are based on these two initial set ups, are presented in Fig. 4.10 (top graphs).

In the hydrodynamical models the contact discontinuity is further away from the blast wave and closer to the reverse shock than the observed locations in the SNR 0519-69.0. This suggests that some of the effects that may have brought the ejecta in Tycho's SNR close to the forward shock, whether pure hydrodynamical effects, or efficient cosmic ray acceleration, may to a lesser extent also have affected SNR 0519-69.0. In the near future we intent to produce models that incorporate cosmic ray acceleration into the hydrodynamic models (Kosenko et al. in preparation). Note that Cassam-Chenaï et al. (2008) found that for SN 1006 the contact discontinuity is also close to the shock front, to a lesser extent even for those regions that do not emit X-ray synchrotron radiation, where efficient cosmic ray acceleration is likely not important. Their models suggest that cosmic ray acceleration alone is not sufficient to explain the observations. This suggests that the distance of the contact continuity to the shock front is the result of a mixture of efficient cosmic ray acceleration and hydrodynamical instabilities (see also Miceli et al. 2009, and the discussion in Sect. 4.5.2).

Estimated from our numerical models, the fraction of the total supernova matter, swept-up by the reverse shock is as follows: $M_{\rm O} = 7\%,\ M_{\rm Si/S} = 12\%/7\%,\ M_{\rm Ar/Ca} = 1\%/2\%,\ M_{\rm Fe} = 63\%$ for c050403 and $M_{\rm O} = 3\%,\ M_{\rm Si/S} = 12\%/7\%,\ M_{\rm Ar/Ca} = 1\%/2\%,\ M_{\rm Fe} = 71\%$ for m060403 explosion model. With a total mass of the shocked ejecta of $1.2\,M_{\odot}$ in both cases. We see that the fractional mass of Fe in c050403 model matches the observed fractional mass reasonably well as determined in Sect. 4.4.3, but the observed fractional mass of oxygen appears to be higher than indicated by the models. This may hint that the progenitor was an oxygen-rich white dwarf. The lack of neon in the RGS spectra and magnesium in the EPIC spectra still argues in favor of C/O white dwarf, and not an O/Ne/Mg white dwarf, which is consistent with type Ia explosion models (e.g. Woosley et al. 2007).

4.5.6 RGS line broadening and the shock velocity

Using the measured value of the emission lines broadening ($\sigma_{\rm RGS}$), we can estimate the velocity of the forward shock. The temperature of each species behind

the reverse shock is calculated from (no temperature equilibration between species assumed)

$$kT_i = \frac{3}{16} m_i v_{\rm RS}^2 \tag{4.3}$$

here m_i — mass of species i, $v_{\rm RS}$ — reverse shock velocity. Thus, the Maxwellian thermal broadening of the lines is

$$\sigma_{\rm th\,ej} = \sqrt{\frac{kT_i}{m_i}} = \frac{\sqrt{3}}{4} v_{\rm RS} \tag{4.4}$$

As it is shown above, according to the analytical Truelove & McKee (1999) solution, for the case of SNR 0519-69.0 the relation $v_{\rm RS} = 1.2\, v_{\rm FS}$ holds. Also, according to the numerical models, the value of the bulk velocity in the ejecta is by $\sim 50\%$ lower than the bulk velocity in the shocked CSM (the velocity profiles of the HD models on the top right plots of Fig. 4.10), i.e. $\sigma_{\rm bulk\,ej} \simeq 0.5 \sigma_{\rm bulk\,CSM} = 0.5\,(3/4)\, {v_{\rm FS}}^2$. Thus

$$\sigma_{\rm RGS} = \sqrt{\sigma_{\rm th\,ej}^2 + \sigma_{\rm bulk\,ej}^2} \simeq 0.64\, v_{\rm FS} \tag{4.5}$$

Substituting the measured value of $\sigma_{\rm RGS} = 1873 \pm 50$ km s^{-1} into eq. (4.5), we obtain $v_{\rm FS} = 2927 \pm 500$ km s^{-1}. Where the error includes an estimate of the systematic uncertainties, which come from relation of $\sigma_{\rm RGS}$ to $v_{\rm FS}$.

From the optical observation of the remnant we have independent measurements of the blast wave velocity, but these measurements give ambiguous values. van Adelsberg et al. (2008) modeled hydrogen spectra of the SNR and found shock velocities of $v_{\rm FS} = 2984^{+703}_{-185}$ km s^{-1} and $v_{\rm FS} = 1178^{+185}_{-157}$ km s^{-1} based on the observations of Ghavamian et al. (2007a) and Smith et al. (1991) respectively. Measurements of Hα-line along the rim by Tuohy et al. (1982) provide the value of $v_{\rm FS} = 2800 \pm 300$ km s^{-1}. Our estimate is the closest to the estimates by Tuohy et al. (1982) and Ghavamian et al. (2007a). The lower value of the forward shock velocity in the measurements by Smith et al. (1991) is probably caused by the slit location they used, which intersects the bright eastern rim of the SNR, where the blast wave probably encounters a dense cloud of interstellar matter and may have slowed down (Ghavamian et al. 2007a).

4.6 Conclusions

We analyzed X-ray data of SNR 0519-69.0, which were obtained by both the XMM-Newton and Chandra observatories. We treated the spectra with SPEX fitting software and applied non-equiliblium ionization (NEI) models. Fitting of the

[2]The contributes to the line broadening, as the RGS takes a spectrum of the whole remnant. The expanding shell of shocked material will hence contribute to the line broadening. This results in a 'hat-profile' in the spectral lines, convolved with the Gaussian line profile caused by the thermal broadening. We characterize the observed lines with a Gaussian line profile.

data with the single-ionization timescale NEI model allowed us to measure average electron temperature of 3 keV, ionization timescale of 2.3×10^{10} s cm^{-3}.

The stratification of the elements is particularly pronounced in the radial emissivity profiles of the Chandra images of the SNR. Chandra ACIS spectra of specific regions of the SNR also points to the separation of the elements in the shell. This inspired us to use a multi-component fitting model for the EPIC MOS and RGS spectral analysis, in which the observed layers are each represented by an NEI component dominated by one or two elements. This multi-component model provides an adequate description of both the broad band EPIC MOS spectra and the high spectral resolution RGS spectra in the 0.5-1.1 keV band. In addition it allowed us to characterize the Chandra ACIS spectra of several distinct regions. Using this approach we estimate the density of the circumstellar matter of 2.4 ± 0.2 cm^{-3}.

The results of our analysis show that the X-ray data of SNR 0519-69.0 are consistent with mildly or moderately mixed delayed detonation explosion models, which result in clear separation of the outermost oxygen layer (produced during the final detonation phase), followed inwards by the partially mixed inner layers of intermediate mass elements and iron (deflagration phase of the explosion). The mass fraction that we infer are $M_{\rm O} \approx 32\%$, $M_{\rm Si/S} \approx 7\%/5\%$, $M_{\rm Ar+Ca} \approx 1\%$ and $M_{\rm Fe} \approx 55\%$, which should be considered with some caution, as we had to infer a volume filling factor to convert from emission measure to mass. Taken at face value, these mass fraction are consistent with recent observational results of Type Ia supernovae (Mazzali et al. 2007), which show that all material out to an enclosed mass of ~ 1.1 M$_\odot$ is burned into IME and heavier elements, leaving about $0.2 - 0.3$ M$_\odot$ for oxygen, provided all carbon was burned. The mass fractions of IME and Fe in SNR 0519-69.0 puts contraints on the sub-classification of the supernova, suggesting a Type Ia event of normal peak luminosity.

The RGS data allowed us to measure the line broadening of the shocked ejecta of 1873 ± 50 km s^{-3}, which helped to constrain the dynamical properties of the remnant and estimate the forward shock velocity of 2770 ± 500 km s^{-1}. This value is consistent with the measurements reported by Tuohy et al. (1982) and Ghavamian et al. (2007a), but inconsistent with Smith et al. (1991).

4.7 Acknowledgements

We thank the anonymous referee for his/her insightful comments, which helped to broaden the scope of this paper. We also thank S.I. Blinnikov for providing us with the thermonuclear explosion models and also for the fruitful discussions on explosion mechanisms. DK is supported by an "open competition" grant and EH and JV are supported by a Vidi grant from the Netherlands Organization for Scientific Research (PI J. Vink). The work is also partially supported in Russia by RFBR under grant 07-02-00961.

5

Cosmic-ray acceleration efficiency vs temperature equilibration: the case of SNR 0509-67.5

E.A. Helder, D. Kosenko and J. Vink
Astrophysical Journal Letters, 2010, 719, L140

We study the 0509-67.5 supernova remnant in the Large Magellanic Cloud with the VLT/FORS2 spectrograph. We detect a broad component in the Hα emission with a FWHM of 2680 ± 70 km s^{-1} and 3900 ± 800 km s^{-1} for the southwest (SW) and northeast (NE) shocks, respectively. For the SW, the proton temperature appears to be too low for the shock velocity, which we attribute to a cosmic-ray pressure behind the shock front of at least 20% of the total pressure. For the NE, the post-shock proton temperature and the shock velocity are compatible, only if the plasma behind the shock front has a degree of thermal equilibrium of over 20%, which is at odds with current models for temperature equilibration behind fast shocks, which do not accelerate cosmic rays. If we assume the electron temperature to be less than 10% of the proton temperature, we find a post-shock cosmic-ray pressure of at least 7%.

5.1 Introduction

Supernova remnants (SNRs) are generally thought to be the dominant sources of Galactic cosmic rays. For this to be true, SNRs need to transfer about 10% of their initial kinetic energy into cosmic rays. An open question is whether SNR shocks can reach these acceleration efficiencies averaged over their life time; recent TeV and GeV γ-ray observations give promising but ambiguous results (Ellison et al. 2010; Abdo et al. 2010).

Although the process of efficiently accelerating particles is well understood (Malkov & Drury 2001), observational verifications for efficient acceleration are scarce (e.g. Warren et al. 2005; Lee et al. 2007; Vink et al. 2006; Helder et al. 2009). These observations are essential for characterizing the efficiency of the acceleration. As the particles move ahead (i.e., upstream) of the shock, they form a so-called shock precursor, which compresses and pre-heats the upstream medium. This effectively lowers the Mach number of the main shock, therewith lowering the temperature behind the shock front (Ellison et al. 2004; Drury et al. 2009). This effect would ideally be characterized by the post-shock proton temperature ($T_{\mathrm{s,\,p}}$), as $T_{\mathrm{s,\,p}}$ is close to the plasma temperature, whereas the post-shock electron temperature $T_{\mathrm{s,\,e}}$ might be lower (e.g. Ghavamian et al. 2007b). The latter implies that the electrons might constitute only a minor part of the thermal pressure behind the shock front.

For some SNRs, $T_{\mathrm{s,\,p}}$ can be determined from hydrogen line emission at the shock fronts; these are so-called Balmer-dominated shocks. The hydrogen lines of a Balmer-dominated shock consist of two superimposed components: the narrow component emitted by neutral hydrogen after entering the shock front and the broad component by hot protons after undergoing charge exchange with incoming neutral hydrogen atoms. The width of the broad component reflects the proton temperature behind the shock front (Chevalier et al. 1980; Heng 2009).

In this *Letter*, we report on our study of SNR 0509-67.5, as this is a likely source of efficient cosmic-ray acceleration; recent studies show that the remnant resulted from a highly energetic Type Ia explosion (Hughes et al. 1995; Badenes et al. 2008; Rest et al. 2008). Its X-ray spectrum provides some evidence for non-thermal emission (Warren & Hughes 2004). In addition, hydrodynamical models show that the presence of highly energetic particles is likely not negligible (Kosenko et al. 2008).

SNR 0509-67.5 was discovered to have Balmer-dominated shocks by Tuohy et al. (1982), although the flux in the broad component was too low to be detected. A subsequent attempt by Smith et al. (1991) did not reveal any broad component either. The first detection of a broad component in the hydrogen line emission of this remnant was by Ghavamian et al. (2007a), who measured the width of the broad component of the Lyβ line to be 3700 $\pm$400 km s^{-1}, corresponding to a shock velocity (v_{s}) of 5200-6300 km s^{-1}. However, as the spectrum was taken from the entire remnant, it remains uncertain whether the obtained line width is

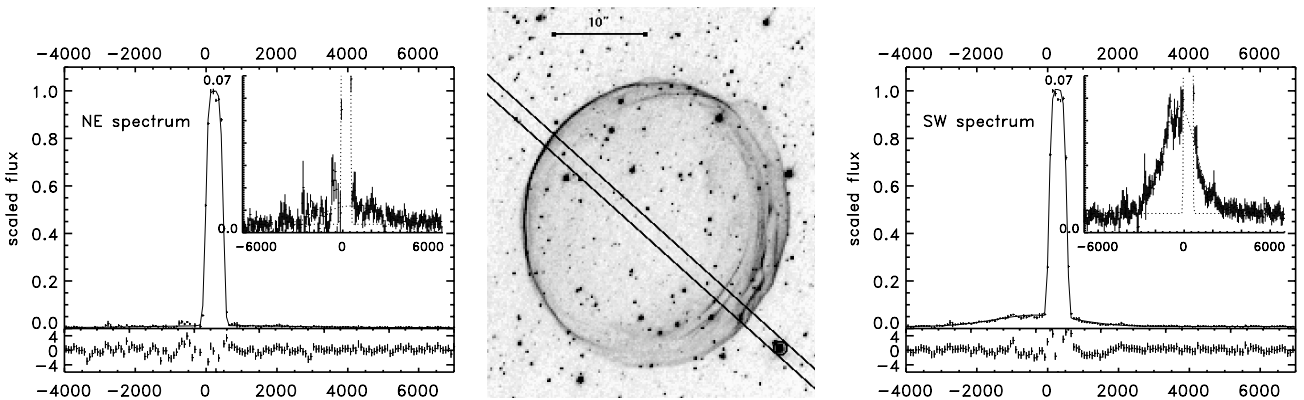

Fig. 5.1: *Left:* spectrum and best fit of the NE shock of SNR 0509-67.5. *Middle:* archival HST/ACS observation of SNR 0509-67.5, as obtained at 2006 October 28, with an exposure time of 4620 s. The position of the longslit of the VLT/FORS2 instrument is indicated. The star on which the slit is centered is indicated with a circle. North is up, east is to the left. *Right:* spectrum and best fit of the SW shock. The lower panels show the residuals divided by the errors. The insets show a zoom-in of the broad component, with the best-fit narrow and broad components overplotted.

broadened by the bulk motion of the plasma as well.

We report the detection of a broad component in the Hα line emission of SNR 0509-67.5 at two locations of the shock front. We combine this with a shock velocity based on X-ray observations (Kosenko et al. 2008) to determine the fraction of the post-shock pressure contributed by cosmic rays.

5.2 Optical data and results

We observed SNR 0509-67.5 for 10932 seconds (four blocks of 2733 s) with FORS2, the low-dispersion spectrograph of ESO's VLT (Appenzeller et al. 1998). The observations were made on 2009 October 15 and 20 and November 10 and 11. By centering the slit at a bright star at $\alpha = 05:09:28.793$, $\delta = -67:31:30.83$ (J2000), with a position angle of 42° (Figure 5.1), we obtained spectra of both the SW and NE rims with a single pointing. The width of the slit was 1.6″ which, in combination with the 600RI grism and the 2×2 binned readout, corresponds to a resolution of ~ 485 km s^{-1} at Hα (6563 Å). This resolution prevents us from resolving the narrow component of the Hα line, but it increases the signal-to-noise sufficiently to detect and resolve the broad component. The data were corrected for bias, flatfielded, and the skylines and cosmic rays were removed. The wavelength calibration was done by fitting a fourth order polynomial to the spectral lines of He, HgCd, Ar and Ne lamps, obtained during daytime. In addition, we checked our calibration against the position of three skylines (at 5577.3, 6864.0 and 7571.7 Å, respectively; Osterbrock et al. 1996). The absolute wavelength calibration has a systematic uncertainty of 0.5 pixel (37 km s^{-1}) and the errors on the data points were determined by tracing the error propagation through the reduction steps, starting from the raw data. For each observation block, obvious outliers, probably caused by erroneous skyline subtraction, were removed. The resulting spectra were fitted with two superimposed Gaussians and an offset, convolved with the slit width. The best-fitting parameters for both spectra are listed in Table 5.2. In order to determine the significance of the broad component in the NE spectrum, we compared the obtained χ^2 value (464) with a fit in which we only fitted a single Gauss to the spectrum (525). The difference indicates a significance of 7.8σ. The $\chi^2_{\rm red}$ values are 2.03 and 2.56 for the SW and NE fits respectively. These high values are mainly caused by substructure of the narrow line: a fit to the broad component with a single Gauss, excluding the central region (between -100 and 800 km s^{-1}), convolved with the resolution, gives $\chi^2_{\rm red}$ of 0.51 for the SW and 0.76 for the NE. This substructure might either be caused by spatial surface brightness fluctuations of the remnant within the slit, or by errors in the skyline subtraction. We determine the 1σ errors on the parameters for the broad components by using the errors we determined in our data reduction. For the narrow component we first increased the errors such that $\chi^2_{\rm red} = 1$, and then determined the 1 σ errors, using $\Delta\chi^2 = 1$.

Parameter	SW	NE
center narrow [km s^{-1}]	287.0 ± 1.4	286.0 ± 1.5
center broad [km s^{-1}]	-342 ± 28	459 ± 220
FWHM broad [km s^{-1}]	2680 ± 70	3900 ± 800
total flux[a] [10^{-16} erg s^{-1} cm^{-2} arcsec^{-2}]	8.6	5.3
$I_\mathrm{b}/I_\mathrm{n}$	0.29 ± 0.01	0.08 ± 0.02

[a]Approximate flux calibration based on an observation of a photometric standard star (LTT 2415; Hamuy et al. 1994) taken on 2010 November 11.

5.3 Comparing with shock velocities

To determine the shock velocity, we use the X-ray line width of $\sigma_\mathrm{RGS} = 4900 \pm 420$ km s^{-1}, as observed by the Reflection Grating Spectrometer (RGS) onboard XMM-Newton (Kosenko et al. 2008). This line width is caused by both the thermal and bulk broadening of the plasma. We follow the method of Kosenko et al. (2010) to disentangle the bulk broadening from the thermal broadening to obtain the forward shock velocity, as described below.

As shown in Kosenko et al. (2010), σ_RGS and v_s are related as follows:

$$\sigma_\mathrm{RGS} = (v_\mathrm{s}/4)\sqrt{3r_\mathrm{sh}^2 + 9r_\mathrm{bulk}^2}, \tag{5.1}$$

where $r_\mathrm{sh} = v_\mathrm{rs}/v_\mathrm{s}$ is the ratio of the reverse shock velocity to the forward shock velocity and $r_\mathrm{bulk} = v_\mathrm{bulk,\,ej}/v_\mathrm{bulk,\,CSM}$ is the gradient in the plasma bulk velocity from reverse to forward shock. We obtain $r_\mathrm{sh} \simeq 1$ (whole remnant) and $r_\mathrm{sh} \simeq 0.5$ (NE), from analytical models (Truelove & McKee 1999) with $M_\mathrm{ej} = 1.4\,\mathrm{M}_\odot$, $E = 1.4 \times 10^{51}$ erg and an age of 400 years (Badenes et al. 2008; Rest et al. 2008). Additionally, we constrain the models with a forward shock radius of $15.9 \pm 0.8''$ and $16.3 \pm 0.3''$ for the entire remnant and the NE respectively and a reverse shock radius of $11.4 \pm 2.1''$ and $13.5 \pm 0.2''$ for the entire remnant and the NE respectively, based on a deprojection of Chandra images (48.9 ks, ObsID: 776), following the procedure of Kosenko et al. (2010).

We obtain $r_\mathrm{bulk} = 0.95$ with numerical simulations (Sorokina et al. 2004; Kosenko 2006), using the above parameters.

We use equation (5.1) to estimate $v_\mathrm{s} = 6000 \pm 300$ km s^{-1} (whole remnant) and $v_\mathrm{s} = 6600 \pm 400$ km s^{-1} (NE). In the remainder of this paper, we use conservative v_s estimates of 5000 km s^{-1} for the SW and 6000 km s^{-1} for the NE.

To check these shock velocities, we estimated the expansion with Chandra. Chandra observed SNR 0509-67.5 for three times, with the first observation in 2000 May (earlier used in this section to determine forward and reverse shock radii) and the latter two in 2007 May (29.5 and 32.7 ks, obs IDs 7635 and 8554). Following the method of Vink (2008c), we find a shock velocity of 6700 $\pm$400 km s^{-1} averaged over the azimuth of the remnant. Note that a full proper motion

study of SNR 0509-67.5, using both Chandra and Hubble data, is underway (Hughes et al. 2010). The dense material in the SW (Fig. 5.1) suggests that the forward shock might have recently slowed down. However, we do not find any support for this scenario from the Chandra expansion study, nor from our XMM-Newton/RGS study. Moreover, as the RGS study is skewed toward the bright SW region, it is unlikely that the SW velocity is substantially lower than 6000 km s^{-1}.

5.4 Interpretation

The centroid of the broad component in the SW of -342 ± 28 km s^{-1} indicates the bulk line-of -sight velocity of the shocked protons. Additionally, the Large Magellanic Cloud (LMC) is moving with 278 km s^{-1} away from us (Richter et al. 1987). This means that we are observing a part of the shell which is moving toward us with 620 km s^{-1} with respect to the LMC. Figure 5.1 shows a bright, inner shell close to the outer shock. Taking into account the seeing of 0.8-1.0", our spectrum is probably contaminated by emission from this shell. This part of the shell is likely to dominate the measurement by Ghavamian et al. (2007a), as they also measured a positive offset for the centroid of the broad component.

The flux in the broad component with respect to the flux in the narrow component ($I_{\rm b}/I_{\rm n}$) declines as a function of shock velocity (Heng & McCray 2007; van Adelsberg et al. 2008). Our low values for $I_{\rm b}/I_{\rm n}$ are therefore consistent with a high shock velocity with likely the highest shock velocity in the NE, which has the lowest $I_{\rm b}/I_{\rm n}$. However, as the standard models for interpreting Balmer-dominated shocks do not include the effects of cosmic-ray acceleration, it is not appropriate to use the $I_{\rm b}/I_{\rm n}$ values to determine the shock velocities of SNR 0509-67.5.

5.4.1 Interpreting the FWHMs

To determine the cosmic-ray pressure from our measurements, we need to determine $T_{\rm s,\,p}$ from the FWHM. For low temperatures and shock velocities, $kT_{\rm s,\,p} = m_{\rm p}\sigma^2$ (Rybicki & Lightman 1979), with $\sigma = {\rm FWHM}/\sqrt{8\ln 2}$ in cm s^{-1}. However, as cross sections for charge exchange decline for high velocities (e.g. Fig. 1 in Heng & McCray 2007), $kT_{\rm s,\,p} > m_{\rm p}\sigma^2$ for higher temperatures and shock velocities. Recent studies focused on determining the FWHM as function of $v_{\rm s}$ for non-accelerating shocks (e.g. Heng & McCray 2007; van Adelsberg et al. 2008, resulting in Fig. 5.2). Here, we are interested in FWHM as function of $T_{\rm s,\,p}$ for a given $v_{\rm s}$ instead. We approximate this concave function linearly between 0,0 and the σ^2 and $T_{\rm s,\,p}$ expected for a non-accelerating shock in thermal equilibrium (Fig. 5.2 and 5.3). In this way, we overestimate $T_{\rm s,\,p}$ and the corresponding thermal

pressure, leading to a conservative measure of the cosmic-ray pressure behind the shock front.

We note that the y-axis of Fig. 5 of van van Adelsberg et al. (2008) is labeled incorrectly (M. van Adelsberg, 2010, private communication). Instead of showing the 'broad Hα FWHM', this figure plots the 'broad neutral velocity distribution FWHM', which is independent of the emission line considered. To model a specific emission line such as Hα, one has to convolve the broad neutral velocity distribution with the relevant atomic cross sections. The FWHM-$v_{\rm s}$ relations we use in this study, obtained in electronic form from M. van Adelsberg and K. Heng, are plotted in Fig. 5.2 and are based upon the same relations used to generate Figure 13 and Table 1 of van Adelsberg et al. (2008).

Following Vink (2008a) and Helder et al. (2009), we interpret $T_{\rm s,\,p}$ and v_s in terms of cosmic-ray pressure behind the shock front and cosmic-ray energy flux leaving the system (respectively $w_{\rm CR} = P_{\rm CR}/P_{\rm tot}$ in which $P_{\rm tot}$ is the total pressure behind the shock front (x-axis in Figure 5.4) and $\epsilon_{\rm esc} = F_{\rm esc}/F_{\rm tot}$ in which $F_{\rm tot}$ is the energy flux entering the shock; $\frac{1}{2}\rho_{\rm ISM}v_{\rm s}^3$ (y-axis of Figure 5.4)). To conservatively estimate the post-shock cosmic-ray pressure, we assume the electrons and ions to be in thermal equilibrium. We add $w_{\rm CR}$ and $\epsilon_{\rm esc}$ to the equations

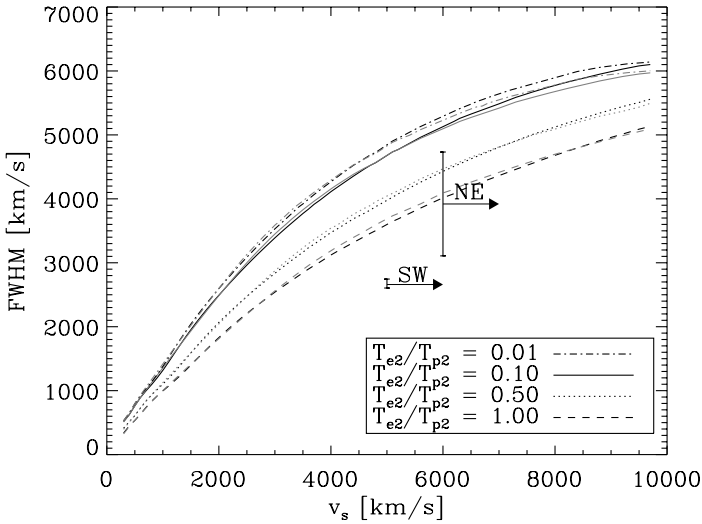

Fig. 5.2: FWHM as function of $v_{\rm s}$ for non-accelerating shocks, for different values for $T_{\rm e}/T_{\rm p}$, (courtesy to K. Heng and M. van Adelsberg). The gray (black) lines indicate this relation for plasmas, that are optically thin (thick) to Lyβ scattering (van Adelsberg et al. 2008). Overplotted is $v_{\rm s}$ and the measured FWHM for both the SW and NE.

of conservation of mass, momentum and energy over the shock front, which leads to:

$$kT_{\mathrm{s,\,p}} = (1 - w_{\mathrm{CR}})\frac{1}{\chi}(1 - \frac{1}{\chi})\mu m_{\mathrm{p}} v_{\mathrm{s}}^2. \tag{5.2}$$

Formally, μ is the number-averaged mean particle weight (~ 0.54 for a fully equilibrated and fully ionized plasma with LMC abundances), when considering $kT_{\mathrm{s,\,p}}$, we can treat μ as well as a measure for the temperature equilibration behind the shock front, where $\mu = 1$ indicates no temperature equilibration, and $\mu = 0.54$ indicates a fully equilibrated plasma. In addition, χ is the total shock compression ratio. For a non-accelerating, adiabatic shock, $\chi = 4$ and hence $kT_{\mathrm{s,\,p}} = \frac{3}{16}\mu m_{\mathrm{p}} v_{\mathrm{s}}^2$. We define $\beta \equiv kT_{\mathrm{s,\,p}} / \frac{3}{16}\mu m_{\mathrm{p}} v_{\mathrm{s}}^2$, to characterize the influence of cosmic-ray acceleration on $T_{\mathrm{s,\,p}}$. Figure 5.4 shows β in the (w_{CR}, ϵ_{esc}) frame. The 'max' line indicates the ratio of the cosmic-ray pressure and escaping cosmic-ray energy for the most efficiently accelerating shock according to theory (Malkov 1999; Drury et al. 2009). Hence, the hashed region is excluded.

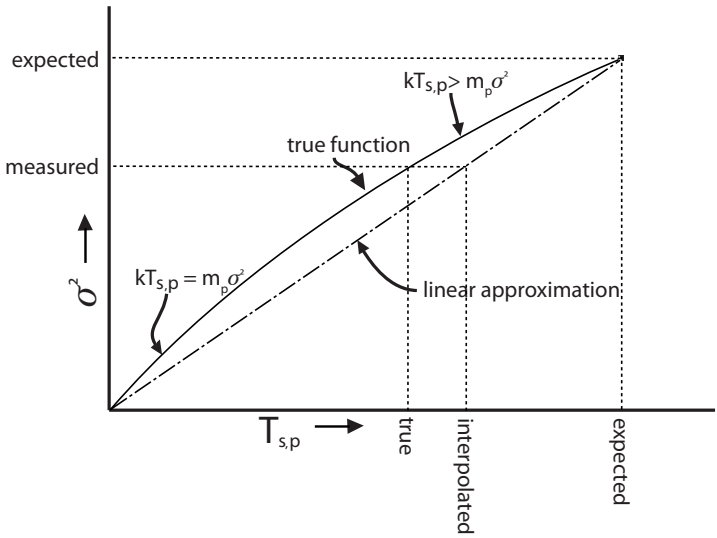

Fig. 5.3: Cartoon of σ^2 as a function of $T_{\mathrm{s,\,p}}$. 'Expected' are the values we expect for a non-accelerating shock (Fig. 5.2). 'True' shows the true $T_{\mathrm{s,\,p}}$ and 'measured' is the corresponding σ^2 we would measure. 'Interpolated' shows our estimated $T_{\mathrm{s,\,p}}$, based on the measured σ^2. Note that this method leads to an overestimation of $T_{\mathrm{s,\,p}}$.

5.4.2 The southwest spectrum

For $v_{\rm s} = 5000$ km s^{-1}, we expect to measure at least an FWHM for the broad component of 3600 km s^{-1}, corresponding to a $T_{\rm s,\,p}$ of 28.7 keV (Fig 5.2). This differs significantly from the measured 2680 ± 70 km s^{-1}. We derive a $T_{\rm s,\,p}$ of 15.9 ± 0.9 keV, leading to a $\beta < 0.58$, which gives a cosmic-ray pressure behind the shock front of at least 20% (Fig. 5.4).

5.4.3 The northeast spectrum

For the NE, the measured FWHM indicates a $v_{\rm s} = 6000$ km s^{-1}, for $0.2< T_{\rm s,\,e}/T_{\rm s,\,p} < 1.0$ (Fig. 5.2). This leads to two possibilities:
1) The shock does not efficiently accelerate cosmic rays and has a $T_{\rm s,\,e}/T_{\rm s,\,p} > 0.2$, breaking with the earlier reported trend of $T_{\rm s,\,e}/T_{\rm s,\,p} \propto 1/v_{\rm s}^2$ for $v_{\rm s} > 400$ km s^{-1} (Ghavamian et al. 2007a), as this would give $T_{\rm e}/T_{\rm p} < 0.01$ for $v_{\rm s} = 6000$ km s^{-1}.
2) The shock is far out of thermal equilibrium, as we might expect for a fast shock, and accelerates particles. If we assume $T_{\rm s,\,e}/T_{\rm s,\,p} < 0.1$, we expect an FWHM of >5100 km s^{-1}, whereas we measure 3900 ± 800 km s^{-1}. Using the approach from section 5.4.1 and Fig. 5.4, we obtain $\beta < 0.85$ and hence a cosmic-ray pressure behind the shock front of $> 7\%$ of the total pressure. Note that this is a very conservative lower limit: for both $T_{s,\,p}$ and $v_{\rm s}$ we used conservative approximations. Also, at this high shock velocity, the squared line width of the broad component does not increase linearly with $T_{\rm s,\,p}$, but flattens off. This makes the difference in line width lower for a given $\Delta T_{\rm s,\,p}$, which makes that the line width is a less sensitive temperature indicator at high shock velocities. Future progress can be made with better shock velocity estimates of the NE region itself, a higher signal-over-noise spectrum of the NE region and with models for non-radiative Balmer-dominated shocks that include the effects of cosmic-ray acceleration.

A remaining question is whether the magnetic field pressure makes a contribution to the post-shock pressure. As SNR 0509-67.5 is at a distance of 50 kpc, we can not resolve filaments of X-ray synchrotron emission, which are often used for determining post-shock magnetic field strengths (Vink & Laming 2003). However, Völk et al. (2005) showed that a typical value for the magnetic field pressure is around 3.5% of the total post-shock pressure. Moreover, according to Bell's theory (Bell 2004) the magnetic field energy density scales as $B^2/8\pi \sim \frac{1}{2} v_{\rm s} U_{\rm c}/c$, with $U_{\rm c}$ being the cosmic ray energy density. This means that the magnetic field energy density is expected to be about 1% of the cosmic-ray energy density.

5.5 Conclusions

We investigated the cosmic-ray acceleration efficiency of the 0509-67.5 SNR in the LMC, by comparing $T_{\rm s,\,p}$, determined from the Hα-line widths of the SW and

NE shocks with shock velocities of respectively 5000 km s^{-1} and 6000 km s^{-1} for the SW and NE, based on X-ray observations. Our study gives the following results:

- We measured widths of the broad components of the Hα lines in SNR 0509-67.5 to be 2680 ± 70 km s^{-1} for the SW and 3900 ± 800 km s^{-1} for the NE.

- For the SW, we can only explain the line width if we allow for a contribution of $> 20\%$ of the post-shock pressure by cosmic rays.

- For the NE shock, we have two options: either the shock has a $T_{\mathrm{s,\,e}}/T_{\mathrm{s,\,p}} > 0.2$, breaking with the earlier reported trend of $T_{\mathrm{s,\,e}}/T_{\mathrm{s,\,p}} \propto 1/v_{\mathrm{s}}^2$ for $v_{\mathrm{s}} > 400$ km s^{-1} (Ghavamian et al. 2007a), or if we assume $T_{\mathrm{s,\,e}}/T_{\mathrm{s,\,p}} < 0.1$, the cosmic-ray pressure behind the shock front is at least 7% of the total pressure.

This research, together with our previous study (Helder et al. 2009), shows that more than 10% of the pressure in young SNRs can be contributed by cosmic rays. This is more than the requirement that 10% of the available energy needs to be in cosmic rays. On the other hand, the cosmic-ray acceleration efficiency may decline for older SNRs, as indicated by a recent study of the Cygnus Loop (Salvesen et al. 2009). So a higher efficiency at a young age may be needed to have an average efficiency of 10% over the whole lifetime of a SNR.

5.6 Acknowledgments

The authors thank Matthew van Adelsberg and Kevin Heng for kindly providing the data used for Figure 2. We also thank Frank Verbunt for critical reading of the manuscript and Cees Bassa and Peter Jonker for useful discussions on the planning and reduction of optical spectra. This research is based on observations collected with ESO Telescopes at the Paranal Observatory under programme ID 384.D-0518(A) and on observations obtained with the XMM-Newton and Chandra satellites. E.A.H. and J.V. are supported by the Vidi grant of J.V. from the Netherlands Organization for Scientific Research (NWO). D.K. is supported by an "open competition" grant from NWO. This research has made use of the NASA/IPAC Extragalactic Database (NED) which is operated by the Jet Propulsion Laboratory, California Institute of Technology, under contract with the National Aeronautics and Space Administration.

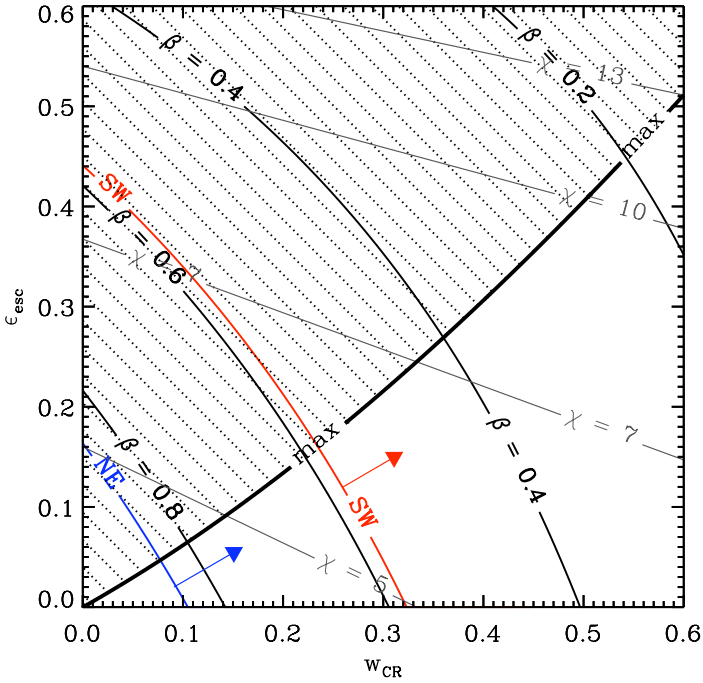

Fig. 5.4: Values for β in the $(w_{\mathrm{CR}}, \epsilon_{\mathrm{esc}})$ frame. The χ-lines indicate the compression ratio of the plasma behind the shock front. The hashed region requires a shock, more efficient than can be explained with current theoretical models. The red line indicates the lower limit for β for the SW. For the NE, β is determined assuming $T_{\mathrm{s,\,e}}/T_{\mathrm{s,\,p}} < 0.1$.

6

Temperature equilibration behind the shock front: an X-ray and optical study

E.A. Helder, J. Vink and C.G. Bassa
Astrophysical Journal, to be submitted

We study the electron-proton temperature equilibration behind several shocks of the RCW 86 supernova remnant. To measure the proton temperature, we use published and new optical spectra, all from different locations on the remnant. For each location, we determine the electron temperature from XMM-Newton/MOS spectra, and correct for temperature equilibration between the shock front and the location of the X-ray spectrum. We confirm the result of previous studies that the electron and proton temperatures behind shock fronts are similar for slow shocks and deviate for faster shocks. However, we can not confirm the previously reported trend of $T_{\rm e}/T_{\rm p} \propto 1/v_{\rm s}^2$.

6.1 Introduction

Shocks are ubiquitous in the Universe and occur at various scales: from planetary shocks in our Solar system to large scale shocks in clusters of galaxies. Astrophysical shocks are rather different from shocks on Earth, as typical mean-free-paths

for particle-particle interactions in the interstellar medium are of the order of parsecs, which is larger than the scale of the shock transitions of interstellar shocks. The fact that we observe sharp transitions, implies that the existence of the shock must be communicated on scales shorter than this mean-free-path.

From conservation of mass momentum and energy over a high Mach number shock front, the temperature of species i can be derived ($T_{\rm i}$):

$$kT_{\rm i} = \frac{3}{16} m_{\rm i} v_{\rm s}^2, \tag{6.1}$$

in which $m_{\rm i}$ is the mass of species i, and $v_{\rm s}$ the shock velocity. This equation holds for a plasma out of thermal equilibrium, implying an electron temperature over proton temperature ($T_{\rm e}/T_{\rm p}$) of the ratio of the electron and proton mass ($m_{\rm e}/m_{\rm p} = 1/1836$). For a plasma in thermal equilibrium, the equation reads:

$$kT = < kT_{\rm i} > = \frac{3}{16} \mu m_{\rm p} v_{\rm s}^2, \tag{6.2}$$

in which μ is the mean particle mass (0.6 for a fully ionized plasma with solar abundances).

In most empirical studies on temperature equilibration behind supernova remnant shocks, $T_{\rm e}$ and $T_{\rm p}$ are determined from Balmer dominated shocks. These shocks are characterized by a hydrogen line profile of two superimposed lines in their spectra. These shocks are non-radiative; their energy losses in the form of radiation are dynamically negligible (this happens for shock velocities > 200 km s^{-1}; e.g. Draine & McKee 1993). The narrow component of the spectrum is emitted by neutral hydrogen atoms, excited shortly after entering the shock front; its width reflects the temperature of the ambient medium. The broad component is emitted after charge exchange between incoming neutral hydrogen and the hot protons behind the shock front. The width reflects the temperature of the protons behind the shock front. Combining the width with the ratio of the flux in the narrow to the flux in the broad component, one can determine the shock velocity and hence the electron temperature (for a recent review, see Heng 2009).

The electron temperature for most young supernova remnants can also be measured from the X-ray spectrum, as the thermal component of the X-ray spectrum is shaped by the electron temperature. Electron temperatures measured from X-ray spectra are generally not the electron temperatures right behind the shock front, but rather somewhat further downstream, where temperatures have already partially equilibrated through Coulomb interactions. The amount of equilibration is a function of $n_{\rm e}t$, which is the ionization time scale, which can be determined from the X-ray spectrum simultaneously with the electron temperature.

Rakowski et al. (2003) studied shocks of the DEM L71 remnant in both optical and X-ray wavelengths. The remnant has shock velocities between 555 and 980 km s^{-1}, which is close to 400 km s^{-1}, where the behavior of $T_{\rm e}/T_{\rm p}$ changes

from being constant to being proportional to $1/v_{\rm s}^2$. Correcting for equilibration effects, Rakowski et al. (2003) showed that $T_{\rm e}/T_{\rm p}$ decreases with increasing shock velocity.

From a theoretical point of view, it is not well determined how much electron-proton temperature equilibration would be expected behind a shock front. Empirical studies on shocks with negligible cosmic-ray acceleration, show that equation 6.2 holds for slow shocks ($v_{\rm s} < 400$ km s^{-1}), whereas the degree of thermal equilibration decreases for faster shocks (Rakowski et al. 2003; Ghavamian et al. 2007b; van Adelsberg et al. 2008). More specifically, a relation of $T_{\rm e}/T_{\rm p} \propto v_{\rm s}^{-2}$ has been suggested for shocks with $v_s > 400$ km s^{-1} (Ghavamian et al. 2007b). This directly implies that $T_{\rm e}$ is nearly constant closely behind the shock front, independently of the shock velocity (equation 6.1). The origin of this relation is attributed to so-called lower hybrid waves ahead of the shock, caused by a (moderate) cosmic-ray precursor (Ghavamian et al. 2007b). Using published data on Hα-spectra as well, but with different models for interpreting Hα spectra, van Adelsberg et al. (2008) found deviations from $T_{\rm e}/T_{\rm p} \propto v_{\rm s}^{-2}$.

In this chapter, we investigate electron-proton temperature equilibration behind several shock fronts of RCW 86, using X-ray and optical data, obtained with XMM-Newton/MOS and VLT/FORS2 respectively. The shocks of the supernova remnant RCW 86 are particularly well suited for this study, as the ionization time scale of the plasma in parts of the remnant is low: $\sim 5 \times 10^9$ cm^{-3}s (e.g., Vink et al. 1997), making the measured electron temperature a more direct indication for the electron temperature at the shock front.

Additionally, the shocks of RCW 86 have a large variety in speeds, as the progenitor exploded in its own wind-blown bubble (e.g., Vink et al. 1997). The southwest (SW) part of the shell has already hit the cavity wall: its X-ray emission is mostly thermal and the shock velocity is ~ 500 km s^{-1} (Ghavamian et al. 2001). The X-ray emission of the NE shock is dominated by X-ray synchrotoron emission (Vink et al. 2006), and its shock velocity is measured to be 6000 ± 2800 km s^{-1} (Helder et al. 2009).

Furthermore, the thermal X-ray emission at the shock front of RCW 86 is from shocked ambient medium (rather than shocked ejecta), tying the fitted parameters of the X-ray spectrum to the physics at the shock front.

6.2 Data and results

6.2.1 VLT/FORS2

For this chapter, we use both published and new optical observations. The observation taken from the southwest (SW) of the remnant was previously published in Ghavamian et al. (2001)and the observation from the northeast (NE) rim and was published in Helder et al. (2009). A summary of all line widths used in this study

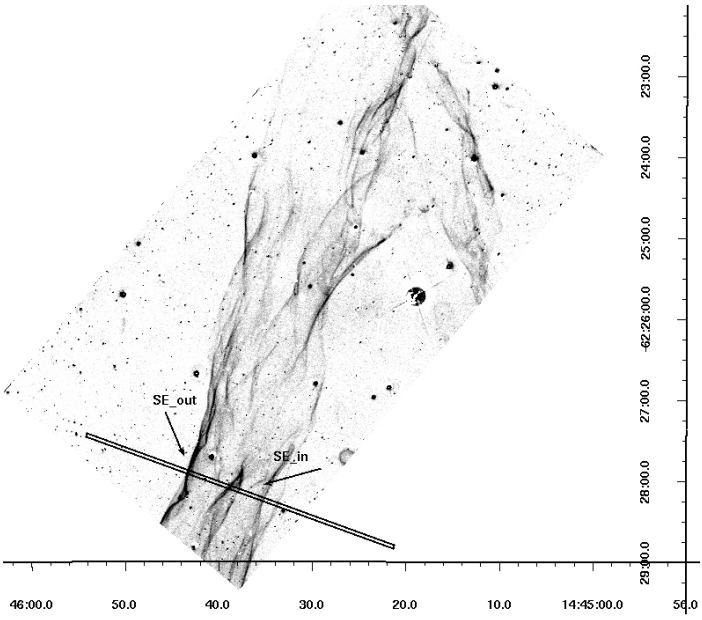

Fig. 6.1: Southwest Hα filament of RCW 86, as observed with VLT/FORS2. Overlaid is the slit position used for the spectra in Fig. 6.2.

can be found in Table 6.2.1.

The optical image of Fig. 6.1 has been obtained with VLT/FORS2 as pre-image for the spectral observation, both in 2007 (programme ID 079.D-0735). The image is a combination of three exposures of 200s, through a narrowband Hα filter (`H_Alpha+83`). To correct for stellar light, three similar images through a narrowband Hα filter, shifted 4500 km s^{-1} (`H_Alpha/4500+61`) have been taken.

Figure 6.1 shows the location of the slit, used to obtain the spectra. The spectra of the southeast (SE) part of the remnant were taken in a single 2733 s exposure, using a 1200R grism and a 2.5" slit. This setup results in a spectral resolution of 350 km s^{-1}, which is sufficient for resolving the broad component, however, the narrow component of the line probably remains unresolved. The data were reduced with standard data reduction steps, as described in Chapter 3, resulting in the spectra shown in Fig. 6.2.

As the slit overlapped more filaments (Fig. 6.1), we were able to extract spectra from two different filaments individually. Here, we focus on the line width of the broad component, as this will give us a direct indication for the post-shock

proton temperature. We fit the spectra with two Gaussian lines, convolved with the resolution of the instrument set-up. Table 6.2.1 lists the line widths obtained from the eastern (SE_{out}) and western (SE_{in}) spectrum in the slit (Fig. 6.1). As the signal-to-noise of the spectrum of the innermost filament is rather low, we used both the inner and middle filament for the SE_{in} spectrum. A fit to solely the innermost filament reveals a width of the broad line similar to the width found of the combined spectrum.

Location	Broad Hα width [km s^{-1}]	proton T [keV]	electron T^a [keV]
NE	1100 ± 60^b	2.3 ± 0.3^a	1.1 ± 0.6
SE_{in}	920 ± 50^d	1.6 ± 0.2^b	0.95 ± 0.15
SE_{out}	1120 ± 40^d	2.4 ± 0.2^b	< 0.05
SW	562 ± 18^c	0.60 ± 0.04^d	0.75 ± 0.1

[a] At the shock front, derived in this study
[b] Helder et al. (2009)
[c] Ghavamian et al. (2001)
[d] Derived in this study

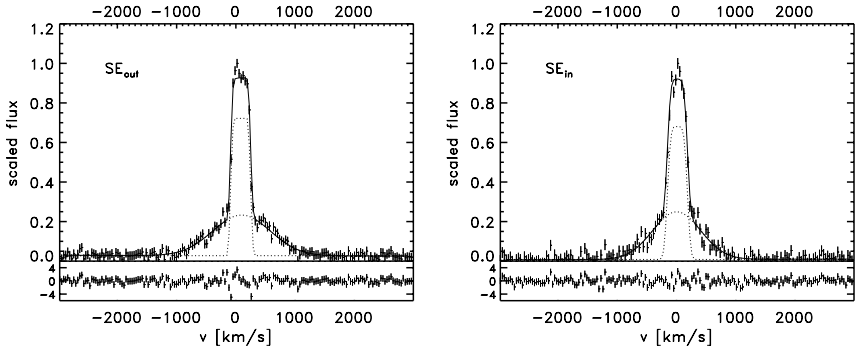

Fig. 6.2: Hα line in the spectrum of the SE_{out} region (left) and for the SE_{out} region (right). Overplotted in both figures are the the individual broad and narrow components (dotted lines) and the total fit (solid line).

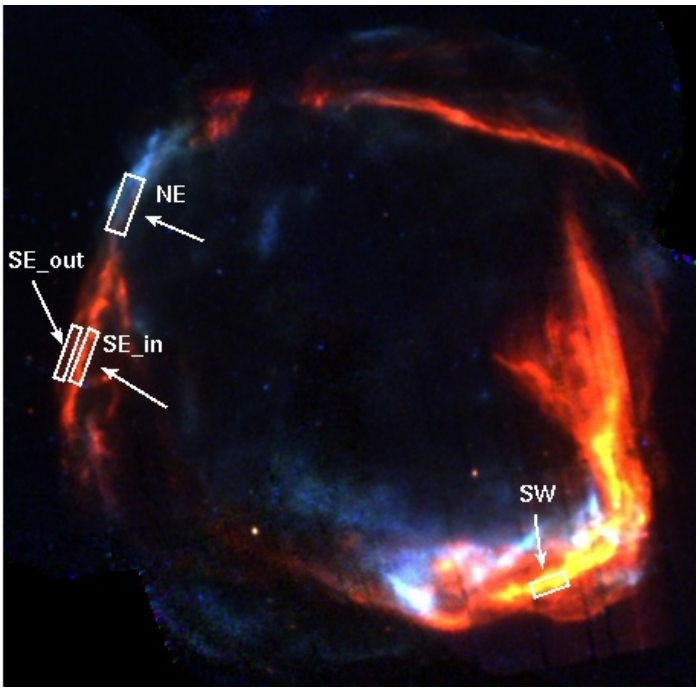

Fig. 6.3: RGB image obtained with XMM-Newton. Shown are the regions from which we extracted an X-ray spectrum, to match the proton temperatures obtained with Hα spectra. In this image, red indicates 0.5 to 1.0 keV, green 1.0-2.0 keV and blue 2.0-4.0 keV.

6.2.2 XMM-Newton

We determine electron temperatures from X-ray spectra, taken with the XMM-Newton/MOS instruments. The observations for the northeast (NE), SE_{in} and SE_{out} spectrum were taken at July 28 (ObsId 0504810101, 117 ks) and for the SW spectrum at August 23 2007 (ObsId 0504810401, 73 ks). The spectra were extracted at locations close to the regions for which we have Hα spectra, as indicated in Fig. 6.3, using the XMM SAS data reduction software, version 1.52.8 (Fig. 6.4). Unfortunately, the position angle of the XMM telescope was chosen such that only the EPIC MOS2 instrument observed the region of interest for the SE and SW rims. For the NE spectrum, we used both the MOS1 and MOS2 instruments.

We fit the extracted spectra with a non-equilibrium ionization model, combined with an absorption model, using the SPEX spectral fitting software version 2.01.02 (Kaastra et al. 1996). The NE spectrum needs an additional power-law component,

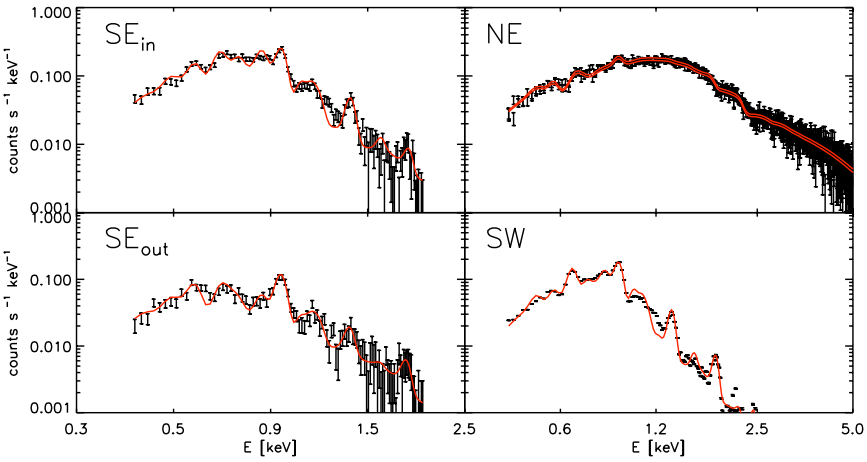

Fig. 6.4: Spectra, corresponding to the regions from Fig. 6.3. Red lines are the best fitting models. Note that the 'NE'-plot includes both a MOS1 and a MOS2 spectrum.

representing synchrotron emission. Table 6.1 lists the parameters of the best-fitting spectral model. The high values for C-statistics/d.of., especially for the SW fit, are mainly caused by a mismatch between the data and the model around 1.2 keV (Fig. 6.4).

6.3 Discussion

6.3.1 XMM-spectra

The parameters in Table 6.1 are consistent with parameters obtained in previous work (Rho et al. 2002; Vink et al. 2006). Problems with fitting the spectrum around 1.2 keV were encountered by Kosenko et al. (2008) for the 0509-67.5 supernova remnant. These deviations are possibly caused by uncertainties in the atomic data base of SPEX. Our electron temperature in the NE filament is lower than the one published in Vink et al. (2006). However, if we analyze exactly their extraction region, the best-fit temperatures are consistent.

The sub solar abundances in all fits show that we indeed fit X-ray spectra from shocked ambient medium, confirming that the measured electron temperatures are related to the proton temperatures at the shock front.

Table 6.1: The best-fit parameters for XMM-Newton MOS spectra. The errors are 1σ.

Parameter	NE[a]	SE_{in}[b]	SE_{out}[b]	SW[b]
EM (10^{54} cm^{-3}kpc^{-2}) [c]	$2.6^{+0.8}_{-0.5}$	6.6 ± 0.8	14 ± 6	4.6 ± 0.3
kT_e (keV)	$1.1^{+0.6}_{-0.4}$	1.1 ± 0.1	0.56 ± 0.15	0.73 ± 0.03
$n_e t$ (10^9 cm^{-3} s)	2.0 ± 0.7	9.0 ± 0.6	6.6 ± 1.5	20.4 ± 0.8
O[d]	1[e]	0.60 ± 0.05	0.44 ± 0.04	0.61 ± 0.03
Ne	1	0.91 ± 0.08	0.54 ± 0.06	1.13 ± 0.06
Mg	1	0.51 ± 0.07	0.37 ± 0.09	0.69 ± 0.05
Si	1	0.29 ± 0.09	1.1 ± 0.5	0.57 ± 0.05
Fe	1	0.41 ± 0.06	0.8 ± 0.7	0.43 ± 0.02
PL norm. [f]	1.58 ± 0.03	–	–	–
Γ	2.77 ± 0.02	–	–	–
N_H (10^{21} cm^{-2})	4.40 ± 0.09	3.0 ± 0.2	4.2 ± 0.3	3.21 ± 0.15
C-statistics/dof	1029/740	303/97	181/97	1050/164

[a] based on MOS1 and MOS2 data
[b] based on MOS2 data
[c] The emission measure (EM) is defined as $\int n_e n_H dV/d^2$
[d] Abundances are relative to solar values (Anders & Grevesse 1989)
[e] A '1' indicates abundances fixed to solar abundances
[f] power law normalization [10^{44} ph s^{-1} keV^{-1}]

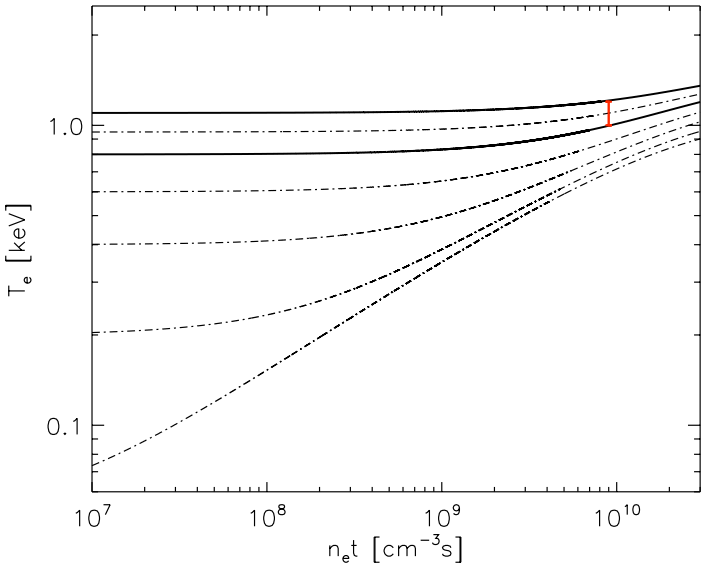

Fig. 6.5: Figure with temperature histories for the SE_{in} location (T_p = 1.6 keV), as function $n_e t$ for different T_e-values at the shock front. From top to bottem, the lines indicate a T_e at the shock front of 1.10, 0.95, 0.80, 0.60, 0.40, 0.20 and 0.05 keV.

6.3.2 Proton temperatures

The measured line width of the broad Hα component gives a measure for the proton temperature behind the shock front. For line widths with FWHM < 2000 km s^{-1} (van Adelsberg et al. 2008), $kT_p = m_p \sigma^2$, with $\sigma = \mathrm{FWHM}/\sqrt{8 \ln 2}$ and the FWHM in km s^{-1} (Rybicki & Lightman 1979), leading to the values in Table 6.2.1.

Table 6.2.1 shows that T_p for SE_{out} is higher than T_p for the SE_{in} spectrum, implying a higher shock velocity (equation 6.1). SE_{out} lies outward of SE_{in}, which is suggestive for a higher shock velocity as well.

6.3.3 Temperature equilibration at the shock front

The proton temperature is obtained from optical spectra directly behind the shock fronts, as the neutral hydrogen will ionize quickly after entering the shock front. To obtain an X-ray spectrum with sufficient signal-over-noise, we extracted over a larger region of the remnant than the region over which the proton temperature was determined. Also, the spatial resolution of the EPIC-MOS instruments (6") will cause contamination from other regions in a spectrum of just the location of

the Hα data.

This means that the electron and proton temperatures will have undergone some equilibration at the extraction region of the X-ray spectrum, implying that the obtained electron temperatures are upper limits (black data points in Fig. 6.6). To compare this to the proton temperatures behind the shock front, we need to determine the amount of heating the electrons experienced. We assume that the electrons are solely heated by Coulomb interactions. Spitzer (1965) derived the coupled differential equation for how fast species i and j with different temperatures (T_i and T_j) equilibrate as function of time (t), writing:

$$\frac{\mathrm{dT_i}}{\mathrm{d}t} = \frac{T_\mathrm{j} - T_\mathrm{i}}{t_{\mathrm{eq\ (i,j)}}}, t_{\mathrm{eq\ (i,j)}} = 5.87 \frac{A_\mathrm{i} A_\mathrm{j}}{n_\mathrm{j} Z_\mathrm{i}^2 Z_\mathrm{j}^2 \ln(\Lambda)} \left(\frac{T_\mathrm{i}}{A_\mathrm{i}} + \frac{T_\mathrm{j}}{A_\mathrm{j}} \right)^{\frac{3}{2}}. \qquad (6.3)$$

For species with atomic numbers A_i and A_j, charge Z_i and Z_j, number density n_j and masses m_i and m_j. Λ is given by

$$\Lambda = \frac{3}{2 Z_\mathrm{i} Z_\mathrm{j} e^3} \left(\frac{k^3 T_\mathrm{i}^3}{\pi n_\mathrm{e}} \right)^{\frac{1}{2}}.$$

Solving the coupled differential equation given by equation 6.3 for electrons, protons, He, O, Si and Fe (assuming solar abundances), we calculate temperature histories up to the measured $n_\mathrm{e}t$ for the measured proton temperature, for different electron temperatures at the shock front (Fig. 6.5). This enables us to determine the electron temperature at the shock front (Table 6.2.1 and red data points in Fig. 6.6). Note that the equilibration time between protons and helium is shorter than between electrons and protons. As a result, the proton temperature might initially increase, before going decreasing to the final temperature.

Equation 6.1 shows that the proton temperature is related to the shock velocity. However, this equation is based on the assumption of conservation of energy over the shock front. In contrast, supernova remnants have been suggested to efficiently accelerate particles which will take away energy. Recent studies have shown RCW 86 to be a cosmic ray accelerator (Vink et al. 2006; Aharonian et al. 2009; Helder et al. 2009).

When a shock accelerates cosmic rays, these create a cosmic-ray precursor ahead of the shock, pushing out and pre-heating the incoming medium. This effectively lowers the velocity of the material entering the main shock, therewith lowering the post-shock temperature (Drury et al. 2009; Hughes et al. 2000b). Hence, v_s will not necessarily be the only variable to characterize T_p. As we focus on T_e-T_p equilibration, we plot T_e as function of T_p, thereby sidestepping the issue whether T_p is determined by v_s solely. This is more reliable as v_s is a quantity derived through Equation 6.1, which may not be valid in the presence of cosmic-ray acceleration (Helder et al. 2009).

Fig. 6.6 shows that $T_\mathrm{e} \sim T_\mathrm{p}$ for the data point with the lowest T_p. Van Adelsberg et al. (2008) calculated $T_\mathrm{e}/T_\mathrm{p} = 0.826^{+0.03}_{-0.51}$ for this specific data point,

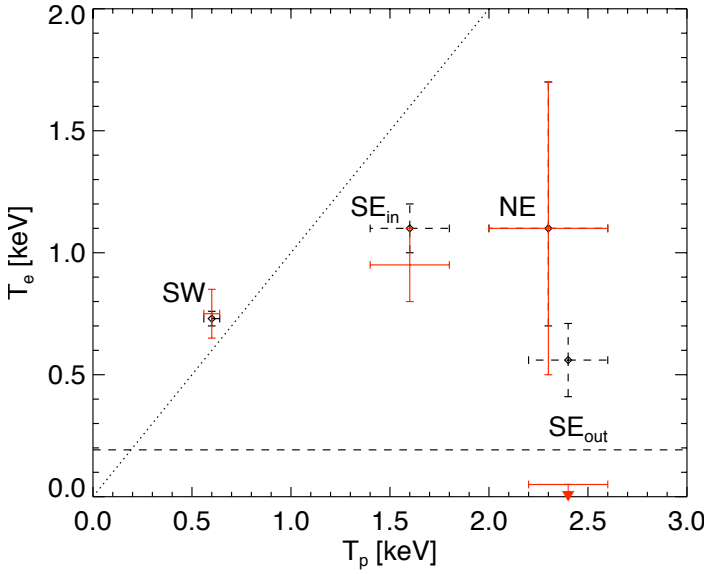

Fig. 6.6: Proton and electron temperatures (x and y-axis respectively) from Table 6.2.1 and 6.1. The black data points show the electron temperature as calculated from the X-ray spectra. The red data points indicate electron temperatures after correcting for Coulomb equilibration.The dotted line indicates $T_\mathrm{p} = T_\mathrm{e}$. The dashed line indicates the electron temperature as calculated for a 400 km s^{-1} shock with thermal equilibrium behind the shock front; the relation found by Ghavamian et al. (2007b) would be on this line.

which is rather similar to our value, given the systematic uncertainties in both approaches. The rightmost data points in Fig. 6.6 show $T_\mathrm{e} < T_\mathrm{p}$, consistent with previous results, however, we do not find a relation of $T_\mathrm{e}/T_\mathrm{p} \propto 1/v_\mathrm{s}^2$, which would result in a horizontal line in Fig. 6.6.

6.4 Conclusions

We investigated the proton-electron temperature equilibration behind several shock fronts of RCW 86. The low ionization parameter $n_\mathrm{e}t$ of this remnant ensures that the current T_e of the plasma is close that at the shock front. The electron temperatures were determined from X-ray spectra, obtained from XMM-Newton data and corrected for equilibration effects, resulting in Fig. 6.6. We used both new and published data to determine proton temperatures. From this study, we can draw the following conclusions:

– The FWHM of the broad Hα line in the SE of RCW 86 are 1120 ± 40 and 920 ± 50 km s^{-1} for the SE$_{\rm out}$ and SE$_{\rm in}$ spectrum respectively.

– $T_{\rm e}/T_{\rm p} \sim 1$ for slow shocks ($T_{\rm p} < 1$ keV), confirming previous studies.

– $T_{\rm e}/T_{\rm p} < 1$ for faster shocks. However, we do not find a constant electron temperature for faster shocks, as implied by the model of Ghavamian et al. (2007b). Additionally, our results show $T_{\rm e}/T_{\rm p} > m_{\rm e}/m_{\rm p}$.

References

Abdo, A. A. et al. 2010, ApJL, 710, L92
Aharonian, F. et al. 2001, A&A, 370, 112
—. 2009, Astrophys. J., 692, 1500
Aharonian, F. A. & Atoyan, A. M. 1999, A&A, 351, 330
Aharonian, F. A. et al. 2004, Nature, 432, 75
Albert, J. et al. 2007, A&A, 474, 937
Allen, G. 1999, in ICRC, 3, 480–+
Allen, G. E., et al. 2008, Astrophys. J., 683, 773
Allen, G. E., et al. 1997, ApJL, 487, L97+
Anders, E. & Grevesse, N. 1989, Geochim. Cosmochim. Acta, 53, 197
Appenzeller, I. et al. 1998, The Messenger, 94, 1
Badenes, C., et al. 2006, Astrophys. J., 645, 1373
Badenes, C., et al. 2003, Astrophys. J., 593, 358
Badenes, C., et al. 2009, Astrophys. J., 700, 727
Badenes, C., et al. 2008, Astrophys. J., 680, 1149
Bamba, A., et al. 2005, Astrophys. J., 621, 793
Bell, A. R. 2004, MNRAS, 353, 550
Bell, A. R. & Lucek, S. G. 2001, MNRAS, 321, 433
Benetti, S., et al. 2005, Astrophys. J., 623, 1011
Berezhko, E. G. & Ellison, D. C. 1999, Astrophys. J., 526, 385
Berezhko, E. G. & Völk, H. J. 2004, A&A, 419, L27
Blasi, P., Gabici, S., & Vannoni, G. 2005, MNRAS, 361, 907
Bleeker, J. A. M., et al. 2001, A&A, 365, L225
Blinnikov, S. I., et al. 2006, A&A, 453, 229
Branch, D., et al. 2005, PASP, 117, 545
Branch, D., Dang, L. C., & Baron, E. 2009, PASP, 121, 238
Brand, J. & Blitz, L. 1993, A&A, 275, 67
Bykov, A. M., et al. 2008, Space Science Reviews, 134, 119
Caprioli, D., et al. 2009, MNRAS, 395, 895

Cassam-Chenaï, G., et al. 2004, A&A, 414, 545
Cassam-Chenaï, G., et al. 2008, Astrophys. J., 680, 1180
Chevalier, R. A. 1982, Astrophys. J., 258, 790
—. 1983, Astrophys. J., 272, 765
Chevalier, R. A., et al. 1992, Astrophys. J., 392, 118
Chevalier, R. A., et al.. 1980, Astrophys. J., 235, 186
Decourchelle, A., Ellison, D. C., & Ballet, J. 2000, ApJL, 543, L57
DeLaney, T., et al. 2004, Astrophys. J., 613, 343
Delaney, T. et al. 2005
Delaney, T. A. 2004, PhD thesis
den Herder, J. W. 2001, A&A, 365, L7
Draine, B. T. & McKee, C. F. 1993, ARA&A, 31, 373
Drury, L. O'C., et al. 2009, A&A, 496, 1
Drury, L. O'C., Duffy, P., & Kirk, J. G. 1996, A&A, 309, 1002
Dwarkadas, V. V. 2005, Astrophys. J., 630, 892
Ellison, et al. 2004, A&A, 413, 189
—. 2005, A&A, 429, 569
Ellison, D. C., et al. 2010, Astrophys. J., 712, 287
Favata, F., et al. 1997, A&A, 324, L49
Gaisser, T. K. 1990, Cosmic rays and particle physics
Gallagher, J. S., et al. 2008, Astrophys. J., 685, 752
Ghavamian, P., et al. 2007a, Astrophys. J., 664, 304
Ghavamian, P., et al. 2007b, ApJL, 654, L69
Ghavamian, P., et al. 2000, Astrophys. J., 535, 266
Ghavamian, P., et al. 2001, Astrophys. J., 547, 995
Ginzburg, V. L. & Syrovatskii, S. I. 1965, ARA&A, 3, 297
Gotthelf, E. V., et al. 2001, ApJL, 552, L39
Green, D. A., et al. 2008, MNRAS, 387, L54
Hamilton, A. J. S., et al. 2007, MNRAS, 381, 771
Hamilton, A. J. S., et al. 1986, Astrophys. J., 300, 698
Hamuy, M., et al. 1994, PASP, 106, 566
Helder, E. A. & Vink, J. 2008, Astrophys. J., 686, 1094, Chapter 1
Helder, E. A., et al. 2009, Science, 325, 719, Chapter 2
Heng, K. 2009, PASA, 27, 23
Heng, K. & McCray, R. 2007, Astrophys. J., 654, 923
Hörandel, J. R. 2008, Advances in Space Research, 41, 442
Howell, D. A., et al. 2009, Astrophys. J., 691, 661
Hughes, J. P., et al. 1995, ApJL, 444, L81
Hughes, J. P., et al. 2000a, ApJL, 528, L109
Hughes, J. P., et al. 2000b, ApJL, 543, L61
Hughes, J. P. et al. 2010, in prep.
Hwang, U., et al. 2004, ApJL, 615, L117

Kaastra, J. S., et al. 1996, Proceedings of the Eleventh Colloquium on UV and X-ray, p.411
Katsuda, S., et al. 2010, Astrophys. J., 709, 1387
Katsuda, S., et al. 2008, ApJL, 678, L35
Keohane, J. W. 1996, ASPC, 99, 362
Koerwer, J. F. 2009, AJ, 138, 1
Kosenko, D., et al. 2010, ArXiv e-prints: 1001.0983, Chapter 4
Kosenko, D., et al. 2008, A&A, 490, 223
Kosenko, D. I. 2006, MNRAS, 369, 1407
Koyama, K., et al. 1995, Nature, 378, 255
Laming, J. M. 2001, Astrophys. J., 546, 1149
Laming, J. M. & Hwang, U. 2003, Astrophys. J., 597, 347
Landsman, W. B. 1993, ASPC, 52, 246
Lee, J.-J., et al. 2007, ApJL, 659, L133
Lewis, K. T., et al. 2003, Astrophys. J., 582, 770
Long, K. S. & Blair, W. P. 1990, ApJL, 358, L13
Lucy, L. B. 1974, AJ, 79, 745
Lyutikov, M. & Pohl, M. 2004, Astrophys. J., 609, 785
Malkov, M. A. 1999, ApJL, 511, L53
Malkov, M. A. & Drury, L. O'C. 2001, Reports of Progress in Physics, 64, 429
Marion, G. H., et al. 2006, Astrophys. J., 645, 1392
Matsunaga, K., et al. 2001, PASJ, 53, 1003
Mazzali, P. A., et al. 2007, Science, 315, 825
Meyer, P. 1969, ARA&A, 7, 1
Miceli, M., et al. 2009, A&A, 501, 239
Minkowski, R. 1957, in IAU Symposium, 4, 107
Morse, J. A., et al. 2004, Astrophys. J., 614, 727
Osterbrock, D. E., et al. 1996, PASP, 108, 277
Panagia, N. 2005, Nuovo Cimento B Serie, 120, 667
Patnaude, D. J., et al. 2009, Astrophys. J., 696, 1956
Perlmutter, S., et al. 1999, Astrophys. J., 517, 565
Phillips, M. M., et al. 1999, AJ, 118, 1766
Pietrzyński, G., et al. 2009, Astrophys. J., 697, 862
Pohl, M., Yan, H., & Lazarian, A. 2005, ApJL, 626, L101
Press, W. H., et al. 1992, Numerical recipes in C.
Rakowski, C. E., et al. 2003, Astrophys. J., 590, 846
Raymond, J. C., et al. 2008, Astrophys. J., 682, 408
Reed, J. E., et al. 1995, Astrophys. J., 440, 706
Renaud, M., et al. 2006, ApJL, 647, L41
Rest, A., et al. 2008, Astrophys. J., 680, 1137
Rest, A., et al. 2005, Nature, 438, 1132
Reynolds, S. P., et al. 2008, ApJL, 680, L41

Reynolds, S. P., et al. 2007, ApJL, 668, L135
Rho, J., et al. 2002, Astrophys. J., 581, 1116
Richardson, W. H. 1972, Journal of the Optical Society of America, 62, 55
Richter, O., et al. 1987, A&A, 171, 33
Riess, A. G., et al. 1998, AJ, 116, 1009
Röpke, F. K. & Bruckschen, R. 2008, New Journal of Physics, 10, 125009
Rosado, M., et al. 1996, A&A, 315, 243
Rothschild, R. E. & Lingenfelter, R. E. 2003, Astrophys. J., 582, 257
Russell, S. C. & Dopita, M. A. 1992, Astrophys. J., 384, 508
Rybicki, G. B. & Lightman, A. P. 1979, Radiative processes in astrophysics
Salvesen, G., et al. 2009, Astrophys. J., 702, 327
Salvo, M. E., et al. 2001, MNRAS, 321, 254
Schure, K. M., et al. 2009, A&A, 508, 751
Shklovskii, I. S. 1953, Reports of the Academy, U.S.S.R., 90, 983
Smith, R. C., et al. 1991, Astrophys. J., 375, 652
Sollerman, J., et al. 2003, A&A, 407, 249
Sorokina, E. I., et al. 2004, Astronomy Letters, 30, 737
Spitzer, L. 1965, Physics of fully ionized gases
Spitzer, L. 1978, Physical processes in the interstellar medium
Stage, M. D., et al. 2006, Nature Physics, 2, 614
Starck, J.-L., et al. 1998, Image processing and data analysis. The multiscale approach
Stehle, M., et al. 2005, MNRAS, 360, 1231
Stephenson, F. R. & Green, D. A. 2002, Historical supernovae and their remnants, Vol. 5
Tammann, G. A., Loeffler, W., & Schroeder, A. 1994, ApJS, 92, 487
The, L.-S., et al. 1996, AAPS, 120, C357
Thorstensen, J. R., et al. 2001, AJ, 122, 297
Truelove, J. K. & McKee, C. F. 1999, ApJS, 120, 299
Tuohy, I. R., et al. 1982, Astrophys. J., 261, 473
Turner, M. J. L., et al. 2001, A&A, 365, L27
Uchiyama, Y. & Aharonian, F. A. 2008, ApJL, 677, L105
van Adelsberg, M., et al. 2008, Astrophys. J., 689, 1089
Vink, J. 2006, ArXiv: 0601131
Vink, J. 2008a, AIP, 1085, 169
—. 2008b, A&A, 486, 837
—. 2008c, Astrophys. J., 689, 231
Vink, J., et al. 2006, ApJL, 648, L33
Vink, J., et al. 1998, A&A, 339, 201
Vink, J., et al. 1996, A&A, 307, L41
—. 1997, A&A, 328, 628
Vink, J. & Laming, J. M. 2003, Astrophys. J., 584, 758

Vink, J., et al. 2003, ApJL, 587, L31
Vink, J., et al. 2001, ApJL, 560, L79
Vink, J., et al. 1999, A&A, 344, 289
Völk, H. J., et al. 2005, A&A, 433, 229
Wagner, A. Y., et al. 2009, Astrophys. J., 690, 1412
Wang, C. & Chevalier, R. A. 2001, Astrophys. J., 549, 1119
Warren, J. S. & Hughes, J. P. 2004, Astrophys. J., 608, 261
Warren, J. S., et al. 2005, Astrophys. J., 634, 376
Westerlund, B. E. 1969, AJ, 74, 879
Williams, R., et al. 2001, AIP, 565, 185
Willingale, R., et al., 2002, A&A, 381, 1039
Willingale, R., et al. 1996, MNRAS, 278, 749
Winkler, P. F., et al. 2003, Astrophys. J., 585, 324
Woosley, S. E., et al. 2007, Astrophys. J., 662, 487
Yanasak, N. E., et al. 2001, Astrophys. J., 563, 768
Yang, X., et al. 2008, Chinese Journal of Astronomy and Astrophysics, 8, 439
Zirakashvili, V. N. & Aharonian, F. 2007, A&A, 465, 695

7

Nederlandse samenvatting

IEDERE seconde komen miljoenen maal miljoenen atomen met bijna de lichtsnelheid aan op aarde. Ondanks dat deze deeltjes heel klein zijn, kunnen ze energieën hebben, zo groot als die van een goed geslagen tennisbal. Deze deeltjes noemen we kosmische straling. Gelukkig wordt een groot deel van de kosmische straling door onze atmosfeer opgevangen, waardoor wij op de aardkorst nauwelijks iets merken van hetgeen zich boven ons hoofd afspeelt. Dat is maar goed ook, want blootgesteld worden aan kosmische straling kan gevaarlijk zijn. De bemanning van de Apollo raketten zag bijvoorbeeld lichtflitsen, zelfs wanneer ze hun ogen gesloten hielden. Dit bleek veroorzaakt door kosmische straling die met bijna de lichtsnelheid dwars door hun oogbol heenschoot. Ook satellieten kunnen last hebben van kosmische straling, omdat deze de gevoelige electronica aan boord kan vernielen.

Een gedeelte van de kosmische straling is afkomstig van het oppervlak van de zon. Dit zijn echter enkel de deeltjes met lagere energieën. Van de deeltjes met de hoogste energieën is het nog niet helemaal duidelijk waar ze vandaan komen. Deze deeltjes zijn afkomstig van buiten onze Melkweg. Waarschijnlijk worden ze versneld door zware zwarte gaten in de kernen van nabije sterrenstelsels.

Dit proefschrift gaat over de kosmische straling met ‘gemiddelde’ energieën. De energie van deze deeltjes is zo hoog dat ze niet door de zon versneld kunnen zijn. We denken dat ze versneld worden in de Melkweg, omdat hun energie te laag is om te kunnen ontsnappen uit het magneetveld van de Melkweg. Deze deel-

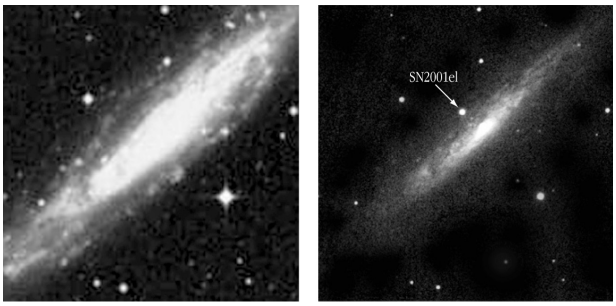

Figuur 7.1: Waarnemingen van het sterrenstelsel NGC 1448. Links is een oud plaatje van dit sterrenstelsel, voordat er een supernova explosie had plaatsgevonden. Het rechter plaatje is gemaakt vlak nadat er een supernova explosie heeft plaatsgevonden. Het lichtpuntje (de supernova) bij de pijl is er in het linkerplaatje nog niet is. Dit plaatje laat zien dat de explosie bijna net zoveel licht geeft als het sterrenstelsel zelf. Credits: ESO

tjes verliezen in tientallen miljoenen jaren energie, waardoor ze op een gegeven moment niet meer te onderscheiden zijn van de normale materie in de Melkweg. Doordat we kosmische straling met deze hoge energieën zien, weten we dat ze niet van veel verder dan de rand van de Melkweg kunnen komen en hun bronnen zich dus hoogstwaarschijnlijk binnen onze Melkweg bevinden.

7.1 Supernovaresten

Kosmische straling is niet alleen heel energetisch, maar er zijn ook nog eens heel veel kosmische stralingdeeltjes. Omdat deze ook energie verliezen, is er ontzettend veel energie nodig om de kosmische straling op peil te houden. Hierdoor zijn de meest veelbelovende bronnen van kosmische straling ook meteen de meest energetische bronnen in onze Melkweg: supernova explosies. Supernova explosies komen voor in twee soorten:

1) sterren die zwaarder zijn dan 8 keer de massa van de zon eindigen hun leven met een supernova explosie. Hierbij blijft een zwart gat of een neutronenster over, omringd door schillen van stermateriaal.

2) lichtere sterren kunnen ook supernovas maken. Zodra het restant van een lichtere ster (witte dwerg) een massa bereikt van 1,4 maal de massa van de zon, wordt de gehele ster in een supernova explosie uiteen wordt gereten.

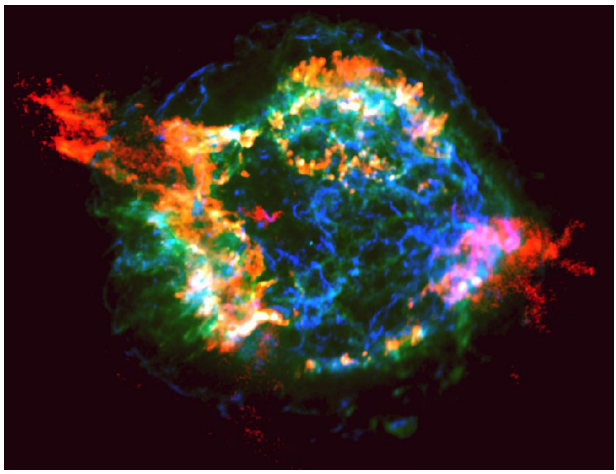

Figuur 7.2: Röntgenwaarneming van de supernovarest Cassiopeia A. gemaakt door de Chandra Röntgensatelliet Chandra. De blauwe kleur laat de hoog energetische electronen zien.

Alhoewel beide manieren waarop de sterren exploderen erg verschillen, lijken de uiteindelijke explosies behoorlijk op elkaar; bij beiden komt zoveel energie vrij dat deze explosie dagenlang net zoveel licht uitstraalt als het hele sterrenstelsel zelf (Figuur 7.1). Bovendien expanderen de schillen met stermateriaal vlak na beide soorten explosies met snelheden van enkele tienduizenden kilometers per seconde door het heelal.

Deze expanderende materie veegt het omliggende materiaal op en wordt daardoor afgeremd. Er vormt zich schil die we supernovarest noemen. Het duurt zo'n 10.000 tot 100.000 jaar voordat de supernovarest volledig is afgeremd en opgaat in zijn omgeving. Gedurende deze periode kunnen we de supernovaresten onder andere waarnemen met telescopen die gevoelig zijn voor zichtbaar licht, radiostraling en met name met telescopen die gevoelig zijn voor Röntgenstraling. Dit levert prachtige plaatjes op, zoals van de supernovarest Cassiopeia A (Figuur 7.2).

De buitenste rand van een supernovarest wordt gevormd door een schokgolf. Al enkele tientallen jaren kennen we een manier waarop schokgolven kosmische straling kunnen versnellen. De deeltjes worden door de lokale magneetvelden over de schokgolf heen en weer gekaatst. Iedere keer dat het deeltje terug wordt gekaatst wint het aan energie. Dit duurt totdat het deeltje zich te ver van de schokgolf verwijdert, en zo ontsnapt uit de supernovarest. Er zijn sterke aanwijzingen dat dit daadwerkelijk gebeurt: de straling van hoog energetische electronen is precies op de schokgolven van supernovaresten gemeten. Deze electronen zijn dus precies zichtbaar op de plaats waar ze versneld zijn en niet ergens anders, omdat ze dan

al een deel van hun energie hebben verloren. Omdat hoog energetische electronen door hun straling goed zichtbaar zijn, hebben we nu vrij directe aanwijzingen dat de schokgolven van supernovaresten electronen tot hoge energieën versnellen. Helaas dragen electronen slechts voor 1% bij aan het totale aantal kosmische stralingsdeeltjes. Het overgrote deel van de kosmische straling bestaat uit protonen, waarvoor we nog geen directe detectiemethode hebben gevonden. Omdat de kosmische straling energie onttrekt aan de supernovarest, zal de supernovarest anders evolueren dan wanneer deze geen deeltjes zou versnellen. Omgekeerd kan deze afwijkende evolutie aanwijzingen kunnen dat supernovaresten ook de bron zijn van de protonen in de kosmische straling.

7.2 Dit proefschrift

De individuele hoofdstukken in dit proefschrift beschrijven diverse waarnemingen van supernovaresten. Met deze waarnemingen onderzoeken we hoe de deeltjes op de schokgolven worden versneld en hoeveel energie de supernovarest aan kosmische straling verliest.

– Hoofdstuk 2 beschrijft een studie over de teruggaande schokgolf aan de binnenkant van de supernovarest Cassiopeia A. Als de buitenste schokgolf wordt afgeremd door het omliggende materiaal, ontwikkelt zich een nieuwe schokgolf, die zich naar binnen beweegt ten opzichte van de buitenste golf. Lange tijd dacht men dat deze schokgolf geen deeltjes kan versnellen omdat er binnen de supernovarest nauwelijks magneetveld aanwezig is. Wij laten in dit hoofdstuk zien dat er wel deeltjes versneld worden door deze teruggaande schokgolf, en dat daarom het van te voren aanwezige magneetveld misschien minder belangrijk is voor het deeltjesversnelproces dan men eerder dacht.

– In hoofdstuk 3 onderzoeken we de hoeveelheid energie die een schokgolf omzet in kosmische stralingsenergie. We hebben dit gemeten door de temperatuur vlak achter de schok te meten. Dit bleek kouder dan dat we berekenden voor een schokgolf die geen deeltjes zou versnellen. Het gas is dus afgekoeld, omdat er energie naar de deeltjes is gegaan. Het blijkt dat meer dan de helft van de druk achter de schokgolf door kosmische straling wordt bijgedragen.

– Hoofdstuk 4 beschrijft een uitgebreide studie naar de supernovaexplosie die de supernovarest veroorzaakte die we nu kennen onder de naam SNR 0519 - 69.0. Ondanks dat deze supernovarest op 163.000 lichtjaar afstand staat, kunnen we zien dat de explosie een gelaagde structuur heeft gehad, als een ui. Aan de binnenkant van de supernovarest zien we voornamelijk ijzer, daarbuiten silicium en zwavel en helemaal aan de buitenkant vinden we

zuurstof. We hebben in deze studie ook de snelheid van de buitenste schokgolf van SNR 0519-69.0 gemeten en hieruit afgeleid dat het licht van de explosie zo'n 450 jaar geleden de aarde heeft bereikt.

– Hierna hebben we in hoofdstuk 5 het jongere broertje van SNR 0519-69.0 onderzocht: SNR 0509-67.5. Voor deze supernovarest hebben we de methode van hoofdstuk 4 gebruikt om de schoksnelheid te meten, en dit gecombineerd met de temperatuur van de protonen achter het schokfront. We nemen in deze studie aan dat de electronen dezelfde temperatuur hebben. Ook uit deze studie blijkt dat een behoorlijk deel ($>$20%) van de energie achter de schokgolf in kosmische straling zit. In werkelijkheid kennen we de temperatuur van de electronen niet, en kunnen ze veel koeler zijn dan we aannemen. In dat geval is het deel van de energie dat in kosmische straling zit zelfs groter.

– We bestuderen het evenwicht tussen de proton- en electrontemperatuur achter het schokfront iets beter in hoofdstuk 6. Eerdere studies hebben laten zien dat de mate van evenwicht tussen de electron- en protontemperatuur achter de schokgolf afhangt van de snelheid van de schokgolf. Voor lage snelheden (< 400 km s^{-1}), zijn de proton- en electrontemperatuur gelijk. Voor steeds hogere snelheden zijn deze temperaturen steeds verder uit evenwicht. Wij meten deze temperaturen in de RCW 86 supernovarest, welke enorme verschillen in schoksnelheden rond de rest heeft. Onze studie laat zien dat de mate van evenwicht tussen electron- en protontemperatuur in RCW 86 niet op een eenduidige wijze van de snelheid van de schokgolf afhangt.

Curriculum Vitae

Eveline Helder werd geboren op 7 oktober 1982 in het Noordhollandse Wijdenes, gemeente Venhuizen. Van 1986 tot 1994 doorliep ze basisschool ‘de Boet’ in ’t Veld. Aansluitend behaalde ze in 2000 haar gymnasium diploma aan de GSg in Schagen. In september van datzelfde jaar startte ze de studie sterrenkunde aan universiteit Leiden. In augustus 2006 studeerde ze af met de scriptie getiteld ‘Gas orbits in a barred galaxy’ onder supervisie van prof.dr. Tim de Zeeuw en dr. Glenn van de Ven.

Op 1 oktober 2006 begon ze haar promotieonderzoek aan de universiteit van Utrecht, wat geresulteerd heeft in dit proefschrift. Individuele hoofdstukken hieruit zijn verschenen als publicaties in Science, the Astrophysical Journal (Letters) en Astronomy & Astrophysics. Gedurende haar promotie heeft ze haar werk laten zien tijdens conferenties en werkbezoeken in Hawaii, Leiden, Tokyo, Granada, Montreal, London, Boston, New Brunswick, Washington, Santa Barbara, Berkeley, Palo Alto, Montpellier en Bremen. Ook heeft ze cursussen gevolgd in Dwingeloo, Blankenberge en London. Daarnaast hielp ze met het oprichten van de Nederlandse Sterrenkunde Olympiade en zat ze in de commissie van de eerste en tweede editie hiervan.

Ze zal haar onderzoek aan supernovaresten vervolgen als post-doc aan de Universiteit van Utrecht.

Dankwoord

Graag wil ik hier iedereen bedanken die afgelopen vier jaar heeft bijgedragen aan dit proefschrift. Niet alleen op wetenschappelijk gebied, maar ook door mij er aan te herinneren dat er ook een wereld is buiten het doen van een promotie.

Als eerste mijn begeleiders: Jacco voor de wetenschappelijke discussies, het enthousiaste commentaar en de mogelijkheden die hij tijdens mijn promotie voor mij heeft gecreëerd. Ik dank Frank voor de kennis over de sterrenkunde, geschiedenis, statistiek, politiek en literatuur die hij met mij heeft gedeeld.

Alex Chiotellis, Bob van Veelen, Dasha Kosenko, Joke Claeys and Klara Schure; it was a great pleasure to enjoy conferences and group meetings with you. I hope we will continue to work on supernova remnants together.

My office mates have contributed and above all suffered when I had to submit papers, proposals, abstracts and applications ('just click submit!'); Evert Glebbeek, Julius Koza, Ana Chies Santos and Selma de Mink, thank you for sharing the office with me! Tim van Werkhoven, zonder jouw hulp en ideeën zou dit proefschrift er veel ongepolijster uitzien. Without the fun, coffee and discussions with the (former) colleagues and support staff of the institute and SRON, the institute would have been a cold and uninspiring environment.

Special thanks to the people who I could always bother at the very last moment with questions on optical observations: Peter Jonker, Manuel Torres, Søren Larsen and Cees Bassa.

Zonder steun en nuchtere opmerkingen van mijn familie was ik vast vergeten dat het doen van sterrenkundig onderzoek nu ook weer niet zo'n grote rol speelt in het leven van de rest van de samenleving. Speciale dank gaat hierbij uit naar Lisanne en Rogier, met wie ik lange (email) conversaties heb gehad naar aanleiding van diverse persberichten, al dan niet over mijn eigen onderzoek.

Daarnaast bedank ik mijn vrienden uit Schagen en Leiden: Eveline, Jolanda, Karin, Marsha, Annika, Arthur, Dorien, George, Jan-Pieter, Laura, Liesbeth, Maarten, Marloes, Patrick and Stefan. Het is bijzonder dat ik jullie nog steeds regelmatig zie en spreek, ondanks dat ik om de paar jaar naar een andere stad

verhuis. Lisanne en Selma, bedankt dat jullie mij tijdens de verdediging van dit proefschrift bij willen staan als paranimfen. Rosalinde, Han en Els, bedankt voor de wijn, dineetjes en het gezellige huis.

Als laatste dank ik Jeroen; zonder jouw eindeloze enthousiasme, steun en geduld had de afgelopen 4 jaar lang niet zo leuk geweest. Ik hoop dat we de komende jaren net zoveel plezier samen gaan beleven als we in de afgelopen jaren hebben gehad!